Volume 01
Number 1
February 2020
Pages 001-200

Materials
Advances

rsc.li/materials-advances

ISSN 2633-5409

ROYAL SOCIETY
OF CHEMISTRY

This is an Accepted Manuscript, which has been through the Royal Society of Chemistry peer review process and has been accepted for publication.

Accepted Manuscripts are published online shortly after acceptance, before technical editing, formatting and proof reading. Using this free service, authors can make their results available to the community, in citable form, before we publish the edited article. We will replace this Accepted Manuscript with the edited and formatted Advance Article as soon as it is available.

You can find more information about Accepted Manuscripts in the Information for Authors.

Please note that technical editing may introduce minor changes to the text and/or graphics, which may alter content. The journal's standard Terms & Conditions and the Ethical guidelines still apply. In no event shall the Royal Society of Chemistry be held responsible for any errors or omissions in this Accepted Manuscript or any consequences arising from the use of any information it contains.

ROYAL SOCIETY
OF CHEMISTRY

rsc.li/materials-advances

Review

Insights to the N₂O decomposition in environmental catalysis: evaluation and advanced outlook

Khezina Rafiq[a], Mamoona Sabir[a], Iqra Sadia[a], Muhammad Zeeshan Abid[a], Muhammad Arif Nadeem[b], Ejaz Hussain[ab]*

Nitrous oxide (N₂O) is a potent greenhouse gas and a significant contributor to stratospheric ozone depletion. Its emission arises from a combination of natural and anthropogenic sources, including microbial processes like nitrification, denitrification, nitrifier denitrification and abiotic chemical pathways such as chemodenitrification and hydroxylamine oxidation. Effective decomposition of N₂O into harmless nitrogen and oxygen is therefore critical for climate mitigation. This review provides a comprehensive overview of the current state of N₂O decomposition, with a focus on mechanisms, catalyst composition and material design strategies. Catalysts are categorized based on their decomposition mechanisms–direct catalytic decomposition (DCD), selective catalytic reduction (SCR) and surface-catalysed redox pathways – as well as their compositions including precious and non-precious metal-based catalysts. Further, a progress-based classification is presented, encompassing classical metal oxides, spinel oxides, layered double hydroxides, MXenes, and metal organic frameworks (MOFs). Emerging systems such as antenna-reactor catalysts and quantum dots are also discussed for their unique properties and potential. Mechanistic insights into N₂O activation, including thermal, surface-catalysed, Mars-van Krevelen-type redox, radical and photocatalytic pathways are explored in depth. This review highlights the significance of catalysts design, oxygen vacancy engineering and atomically dispersed active sites in enhancing activity and selectivity. Future perspectives emphasized the development of low-cost, thermally stable and environmentally benign catalysts, along with mechanistic understanding through in-situ studies and computational modelling. This review aims to guide the rational design of next-generation catalysts for efficient N₂O abatement across industrial and environmental systems.

Table of Contents

a. *Institute of Chemistry, Inorganic Materials Laboratory 52S, The Islamia University of Bahawalpur-63100, Pakistan*
b. *Catalysis and Nanomaterials Lab 27, Department of Chemistry, Quaid-i-Azam University, Islamabad 45320, Pakistan*
Corresponding author contact details: ejaz.hussain@iub.edu.pk; khezina.rafiq@iub.edu.pk

Materials Advances Accepted Manuscript

ARTICLE

8. N$_2$O activation mechanisms
    8.1. Dual-pathway mechanism
    8.2. Radical-mediated oxidation of N$_2$O
    8.3. Electron-mediated reduction of N$_2$O
9. Conclusions and future perspectives

List of Abbreviations

WHO	World health organization
EPA	Environmental protection agency
IPPC	Intergovernmental panel on climate change
AFED	Arab forum for environment and development
APAN	Asian Pacific Adaptation Network
CCCCC	Caribbean Community Climate Change Centre
CAN	Climate Action Network
CCL	Citizen Climate Lobby
CJA	Climate Justice Alliance
EDF	Environmental Defence Fund
HEA	Health and Environmental Alliance
NRDC	Natural Resources Defence Council
GWP	Global warming potential
AOB	Ammonia oxidizing bacteria
AOA	Ammonia-oxidizing archaea
DCD	Direct catalytic decomposition
SCR	Selective Catalytic Reduction
ZSM	Zeolite Socony Mobil
SSZ	Aluminosilicate zeolite
MOF	Metal organic framework
E$_a$	Activation Energy
CFBC	Circulating fluidized bed combustion
SNCR	Selective non-catalytic reduction
EG	Ethylene glycol
DP	Deposition precipitation
IMP	Impregnation Method
DP–Cl	Deposition precipitation by chloride precursor
PTA	Phosphotungstic acid
SACs	Single atom catalysts
DFT	Density functional theory
GC	Gas chromatography
XRD	X-ray diffraction
XPS	X-ray photoelectron spectroscopy
FTIR	Fourier transform infrared spectroscopy
TEM	Transmission electron microscopy
HRTEM	High resolution transmission electron microscopy
TPR	Temperature programmed reduction
H$_2$–TPR	Temperature programmed reduction with H$_2$
XPS	X-ray photoelectron spectroscopy
EXAFS	Extended X-ray absorption fine structure
EDS	Energy dispersive spectroscopy
STEM	Scanning transmission electron spectroscopy
EELS	Electron energy loss spectroscopy
O$_2$–TPR	Temperature programmed reduction with O$_2$
nHAP	Natural hydroxyapatites
SSA	Specific surface area
HADDF	High-angle annular dark field
O$_2$–TPD	Temperature programmed desorption of chemisorbed O$_2$
XRF	X-ray fluorescence
TPSR	Temperature programmed surface reaction
SEM	Scanning electron microscopy
FESEM	Field emission scanning electron microscopy
SAED	Selected area electron diffraction

TPCR	Transfer-PCR
QMS	Quadrupole mass spectrometer
EPR	Electron paramagnetic resonance
TGA	Thermogravimetric analysis
ICP–OES	Inductively coupled plasma optical emission spectrometry
BET	Brunauer, Emmett and Teller theory
MS	Mass Spectrometry
GC–TCD	Gas chromatograph equipped with thermal conductivity detector
DTA	Differential thermal analysis
XRPD	X-ray powder diffraction
QDs	Quantum dots
DRS	Diffuse reflectance spectroscopy
DRIFTS	Diffuse reluctance infrared fourier transform spectroscopy
CO–DRIFTS	Diffuse Reluctance Infrared Fourier Transform Spectroscopy of CO Adsorption
MCT	Mercury cadmium Telluride
LDHs	Layered double hydroxides
MP	Mirror plane
PILC	Pillared clay
VOCs	Volatile organic compounds
LS	Low saturation
SP	Sequential precipitation
TMIs	Transition metal ions
IEC	Ion exchange capacity
WEI	Wet ion exchange
XANES	X-ray absorption near edge structure
CHA	Chabazite
AAS	Atomic absorption spectroscopy
ICP–AES	Inductive coupled plasma atomic emission spectroscopy
FID	Flame ionization detector
ESR	Electron spin resonance
NMR	Nuclear magnetic resonance
SBA	Santa Barbara Amorphous
NTs	Nanotubes
NSs	Nanosheets
NCs	Nanocages
CNTs	Carbon nanotubes
TNTs	Titania nanotubes
PL	Photoluminance
CUS	Coordinatively unsaturated sites
BDC	1, 4-benzenedicarboxylate
BTC	1, 3, 5-benzentricarboxylate
MCM	Mobil Composition of Matter
KIT	Korea Advanced Institute of Science and Technology
MCF	Mesoporous Cellular Foam
Fe–FER	Iron Ferrierites
TG–DTA–MS	Thermogravimetric differential thermal analysis mass spectrometry

1. Introduction

Climate change has become challenging issue to the international agencies like WHO, EPA, IPCC (intergovernmental panel on climate change), AFED (Arab forum for environment and development), APAN (Asian Pacific Adaptation Network), CCCCC (Caribbean Community Climate Change Centre), CAN (Climate Action Network), CCL (International, Citizen Climate Lobby), CJA (Climate Justice Alliance), EDF (Environmental Defence Fund, USA), HEA (Health and Environmental Alliance) and NRDC (Natural Resources Defence Council) etc [1]. For a long time, nitrous oxide (N_2O) was not considered significant environmental pollutant and it did not receive much attention from an environmental perspective. In recent decades, N_2O has been recognized as potent greenhouse gases. It contributes to the greenhouse effect by trapping the heat in the Earth's atmosphere and leading to the global warming. In addition, it is believed to play a role in the destruction of ozone in the stratosphere, contributing to the ozone layer depletion [2]. The presence of atmospheric N_2O is related to the formation of acid rain, which can have detrimental effects on ecosystem and the environment. Moreover, N_2O is of particular concern due to its long atmospheric lifetime, estimated at approximately 120 years. This means that once released into the atmosphere, it persists for a very long time [3]. The global warming potential (GWP) of N_2O is nearly 310 times that of carbon dioxide (CO_2). This high GWP makes it a significant contributor to climate change [4]. Chemical industries, especially in processes like nitric acid production and the industrial synthesis of adipic acid are major sources of anthropogenic N_2O emissions. Specifically, in the synthesis of adipic acid, N_2O is produced when a cyclohexanone/cyclohexanol mixture reacts with nitric acid. It is noted that N_2O emissions from the adipic acid industry contribute a substantial percentage (5-8%) to anthropogenic sources of N_2O in the atmosphere [5, 6]. Both natural and anthropogenic sources of N_2O exist, with industrial sources responsible for emitting a significant amount (400–500 kt) of these gases annually [7].

2. N_2O generation mechanisms

N_2O is generated through multiple pathways, primarily mediated by microbial processes, but also via abiotic chemical reactions. Key mechanisms include *nitrification*, where ammonia is oxidized and N_2O forms as a by-product, and *denitrification*, where nitrate is reduced to nitrogen gases, often realising N_2O when the process in incomplete. *Nitrifier denitrification* also plays a role under oxygen-limiting conditions, while abiotic chemical reactions, such as nitrate reduction by iron or manganese, contribute to additional N_2O fluxes. On top of natural processes, *human activities* significantly amplify these emissions, particularly thorugh intensive agriculture, wastewater management and industrial processes. Different mechanisms are summarized in this section, shown in Figure 1.

2.1. Nitrification

Nitrification is an aerobic microbial process where ammonium (NH_4^+) or ammonia (NH_3) is oxidized to nitrate (NO_3^-) via nitrite (NO_2^-). This process is mediated by ammonia-oxidizing archaea (AOA), as well as nitrate oxidizing bacteria (NOB) in a two-step sequence. The oxidation of hydroxylamine (NH_2OH), a key intermediate, can inadvertently release N_2O as a by-product. N_2O production during nitrification is particularly pronounced under suboptimal oxygen conditions, low pH, or high substrate (ammonia) availability, which destabilize the electron transport chain in AOB. Moreover, recent studies suggest that AOA contribute significantly to N_2O emissions in acidic soils, where bacterial nitrification is less efficient. Thus, nitrification represents both a fundamental nitrogen cycle process and a critical source of N_2O in agricultural and natural soils [8].

2.2. Denitrification

Denitrification is an anaerobic respiratory process in which nitrate (NO_3^-) is sequentially reduced to nitrite (NO_2^-), nitric oxide (NO), nitrous oxide (N_2O) and finally dinitrogen gas (N_2). This pathway is primarily driven by facultative anaerobic bacteria such as *Pseudomeonas*, *Paracoccus*, and *Bacillus* species under low-oxygen or anoxic conditions. The process requires organic carbon as an electron donor, linking it closely to carbon cycling. Accumulation of N_2O often occurs when the enzyme nitrous oxide reductase (NosZ), responsible for reducing N_2O to N_2, inhibited by low pH, low copper availability, or the presence of oxygen. As a result, soils and sediments under fluctuating oxygen conditions, such as wetlands, wastewater systems, and agricultural fields after irrigation, often exhibit high N_2O fluxes. Denitrification is considered the largest single biological source of N_2O globally [9].

2.3. Nitrifier denitrification

Nitrifier denitrification is a hybrid pathway in which nitrifying organisms, under oxygen-limited or microaerophilic conditions, reduce nitrite (NO_2^-) to nitric oxide (NO), nitrous oxide (N_2O) and nitrogen gas (N_2). Unlike conventional denitrification carried out by facultative anaerobes, this process is mediated by ammonia-oxidizing bacteria (AOB). The pathway is particularly relevant in soils, sediments, and wastewater treatment systems where oxygen availability fluctuates. Nitrifier denitrification can account for substantial N_2O emissions when ammonia and nitrite are both abundant, such as in fertilized agricultural soils. It provides a mechanistic link between nitrification and denitrification, highlighting the versatility of microbial nitrogen metabolism under transitional redox conditions [8].

2.4. Abiotic chemical pathways

Although microbial processes dominate, abiotic pathways also contribute to N_2O formation. These include: (i) Chemodenitrification: it involves the reduction of nitrites by ferrous ions (Fe^{2+}) or other reductants, leading to N_2O release. This mechanism is common in waterlogged soils, sediments and mining-impacted environments with high levels of reduced metals. (ii) Oxidation of hydroxylamine

can occur through reactions with metal oxides, particularly ferric (Fe^{3+}) and manganese (Mn^{4+}) oxides, producing N_2O and NO. Additionally, photochemical reactions in sunlit waters and soils have been reported to drive abiotic N_2O formation from nitrite. While biotic pathways may represent a smaller fraction globally, they can dominate under specific geochemical conditions, especially in soils rich in iron or manganese [10].

2.5. Anthropogenic sources

Human activities have amplified N_2O emissions far beyond natural background levels. These include (i) Agriculture: Excessive application of nitrogen-based fertilizers (urea, ammonium nitrate) and livestock manure leads to surplus reactive nitrogen in soils, fueling nitrification, denitrification and nitrifier denitrification. Agricultural soils are estimated to contribute more than 60% of global anthropogenic N_2O emissions. (ii) Wastewater treatment: Biological nitrogen removal processes, particularly in activated sludge and sequencing batch reactors, release N_2O due to incomplete nitrification and denitrification under variable oxygen conditions. Emerging evidence shows that wastewater plants may be hotspots of N_2O release if not properly managed. (iii) Industrial processes: N2O is also released during the production of nitric acid (used in fertilizers) and adipic acid (used in nylon manufacture). Though mitigation technologies exist, incomplete adoption leads to continued emissions. (iv) Biomass burning and fossil fuel combustion: Smaller but notable contributions come from burning crop residues, forests, and fossil fuels, releasing reactive nitrogen that indirectly contributes to N_2O formation. Together, these anthropogenic sources have increased atmospheric N_2O concentrations to record highs, making it the third most important long-lived greenhouse gas and a major contributor to stratospheric ozone depletion. Figure 2a shows distribution of natural versus anthropogenic sources.

3. Categories of N_2O decomposing catalysts based on mechanism and composition

Catalysts for N_2O decomposition are generally classified into different categories depending on their catalytic mechanism, composition, and support material. This classification helps us in understanding theory operational principles, activity under industrial conditions, cost-effectiveness and long-term stability. Below is detailed overview of each category.

3.1. Based on catalytic mechanism

3.1.1. Direct catalytic decomposition (DCD)

In this mechanism, catalysts decompose nitrous oxide (N_2O) directly into N_2 and O_2 without the need of a reducing agent.

$$2N_2O \rightarrow 2N_2 + O_2$$
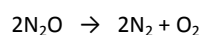
Examples of such catalysts include metal oxides [such as cobalt oxides (Co_3O_4), iron oxide (Fe_2O_3) and manganese oxide (MnO_2)], perovskites (e.g. $La_{1-x}Sr_xCoO_3$ with tunable oxygen vacancies that improve oxygen mobility and enhance N_2O activation) and spinels (e.g. $CuFe_2O_4$, $MnAl_2O_4$) known for their stable structures and redox properties. In DCD, oxygen vacancies on these catalysts adsorb and activate N_2O, leading to bond cleavage and release of N_2. The oxygen atoms are either released as O_2 or incorporated temporarily into the lattice. These catalysts are widely considered for industrial emission control (e.g. nitric acid plants) where large volumes of N_2O are generated.

3.1.2. Selective catalytic reduction (SCR)

In SCR, a reducing agent (such as NH_3, CO or hydrocarbons like CH_4 and C_3H_6) is introduced to facilitate the reduction of N_2O into N_2:

$$N_2O + 2CO \rightarrow N_2 + 2CO_2$$

$$N_2O + 2NH_3 \rightarrow 2N_2 + 3H_2O$$
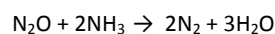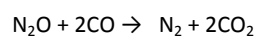
Examples of these catalysts include Fe- or Cu-exchanged zeolites (Fe-ZSM-5, Cu-SSZ-13, Cu-ZSM-5) and vanadium-based catalysts (V_2O_5/TiO_2, V_2O_5-WO_3/TiO_2) etc. The reducing agent react with oxygen species from N_2O decomposition, enhancing N_2 formation. SCR can operate at relatively lower temperatures compared to DCD, making it practical for vehicular exhaust systems and stationary sources. SCR is often applied in mixed gas systems like automotive exhausts, power plants, and mobile sources. Figure 2c demonstrates the role of Cu-zeolites in ammonia-assisted SCR of N_2O, particularly effective in diesel engines.

3.2 Based on catalyst composition

3.2.1. Precious metal-based catalysts

Precious metals such as Rh, Ru, Pt and Pd are highly active for N2O decomposition. They promote rapid N–O bond cleavage due to their strong adsorption capacity for N_2O. Examples include Rh/Al_2O_3, Ru/CeO_2, Pt/ZrO_2 etc. High catalytic activity and efficiency at relatively low temperatures are their key advantages. Their limitations are high cost (that makes them less suitable for large-scale industrial use) and susceptibility to deactivation due to sintering or poisoning (e.g. by sulphur or water vapours). They are often used in niche or specialized applications where high efficiency is required despite high costs (e.g. medical gas purification or research setups).

3.2.2. Non-precious metal-based catalysts

Non-precious metals (mainly transition metals and mixed oxides) are more cost-effective and environmentally sustainable, making them widely used in industrial processes. Examples include transition metal oxides (e.g. Co_3O_4, MnO_x, CuO, Fe_2O_3), perovskites ($LaCoO_3$, $LaMnO_3$, Sr-doped cobaltites with enhanced oxygen mobility), spinels ($CuFe_2O_4$, $MnAl_2O_4$) and zeolites (Fe-ZSM-5, Cu-SSZ-13 with
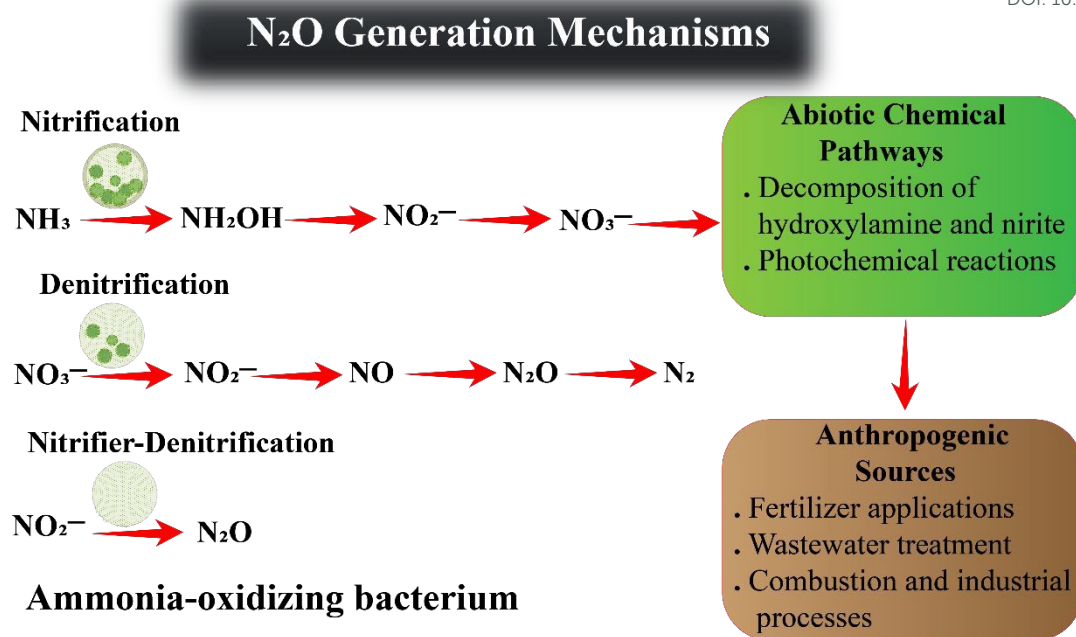
Figure 1. Key mechanisms of N_2O generation.

high hydrothermal stability) etc. Their advantages include low cost, abundant raw materials and high thermal stability. They generally require higher operating temperatures compared to precious metals, but can be optimized by doping or adding promoters. These are widely employed in industrial emission abatement systems, including nitric acid and adipic acid plants, as well as power generation facilities.

3.3 Based on support type

The support material plays a crucial role in dispersing active catalytic sites, enhancing redox behaviour, and providing structural stability under harsh reaction conditions. Common supports include metal oxides like Al_2O_3, TiO_2 and CeO_2 due to their high surface area and redox properties. CeO_2, in particular, enhances oxygen storage and mobility, improving catalytic efficiency. Zeolites include framework structures (like ZSM-5, SSZ-13 and Beta-zeolites) provide high surface area and microporosity. Their ion-exchange ability allows incorporation of Fe or Cu cations, which significantly enhances SCR activity. SSZ-13 is particularly noted for high hydrothermal stability under automotive exhaust conditions. In carbon-based supports, activated carbon and graphene are sometimes used due to their large surface area and electrical conductivity. However, they are less common for N_2O decomposition because of limited thermal stability at high operating temperatures. The choice of support directly influences catalyst dispersion, durability, oxygen mobility and tolerance to poisons (e.g. SO_2, H_2O). Hence, support selection is as important as the active catalytic phase itself.

4. Significance of catalytic decomposition of N_2O

N_2O is also a by-product in various industrial processes, including the catalytic abatement of nitrogen oxides (NO_x) in three-way catalytic converters and selective catalytic reduction (SCR) of NO_x with NH_3. As N_2O is a significant greenhouse gas and its emission contributes to the global warming and climate change. Therefore, there is a pressing need to reduce N_2O emissions from anthropogenic sources. One effective and economical method to reduce N_2O emissions is by catalytically decomposing N_2O into its elemental components (nitrogen and oxygen) which is known as catalytic decomposition of N_2O [11, 12]. To make it effective, the catalyst must be durable and selective. Durability ensures long-term effectiveness of the catalyst and selectivity ensures that N_2O is effectively converted into nitrogen and oxygen without the formation of undesirable by-products [13]. Catalysts designed for N_2O decomposition should be stable even in the presence of moisture, as they may encounter atmospheric moisture during real-world applications. N_2O decomposition is an exothermic reaction, meaning it releases heat during the process. This can occur either thermally (without any catalyst) or catalytically (Figure 2b). The choice between these paths depends on the factors such as operating temperature and the amount of catalysts used [14]. On the other hand, noble metal-based photocatalysts are among reliable options for N_2O decomposition. These catalysts utilize noble metals (e.g. Pt, Pd etc) to facilitate the decomposition of N_2O under the influence of light, making them a potential choice for efficient N_2O abatement [15].

A considerable amount of work has been done in the catalytic decomposition of N_2O, and a number of catalyst systems with a variety of compositions, such as zinc, platinum, copper oxides and zeolites, have been developed [16]. Metal surfaces [17], supported metals [18], metal oxides [19, 20], supported oxides [21], ternary oxides [22], spinel oxides [23], perovskite-type oxides [24], hydrotalcites [25], and transition

metal exchanged zeolites [26] are well-known catalysts that can decompose N$_2$O into its elements even at low temperatures. In this review, important categories of N$_2$O decomposing catalysts are covered, that include transition metal-based zeolites, hydrotalcites, spinel oxides, mixed metal oxides, metal/metal oxides in mesoporous silica, metal oxides, metal-doped nanotubes, nanosheets and nanocages, graphene and graphitic oxides/nitrides, metal-organic frameworks (MOFs), and MOF-derived catalysts. This review compares the different synthesis strategies of catalysts fabrication, experimental conditions, catalyst characterization techniques, N$_2$O decomposition temperatures and catalytic efficiencies of various catalysts (Figure 2d).

5. Progress-based systematic classification of N$_2$O decomposition catalysts
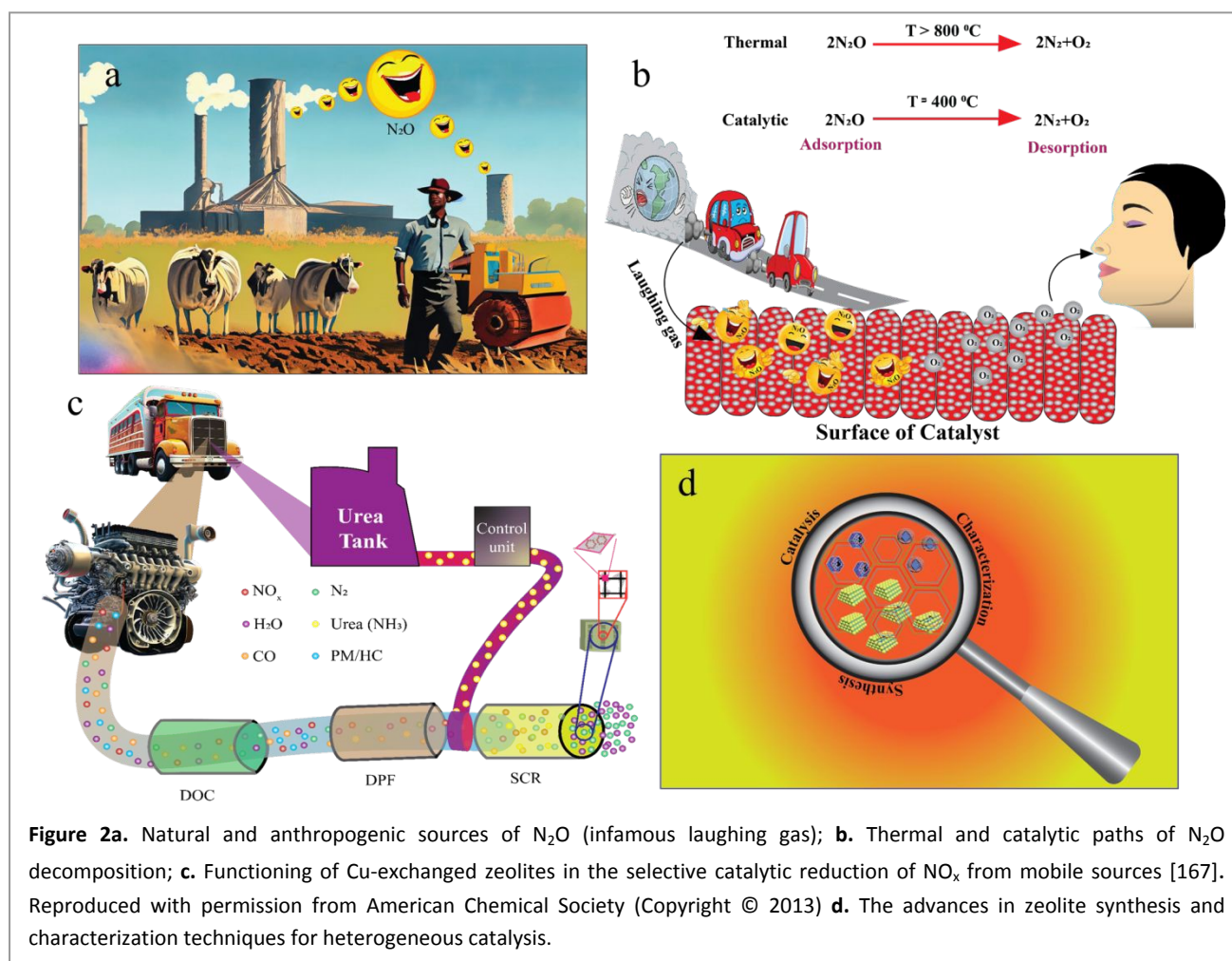
N$_2$O decomposition catalytic materials are classified into five main categories based on their structure, composition and research progress/maturity. Each category includes subtypes ordered by their level of maturity, from well-established (extensively studied) to emerging (recently developed or still under intense research).

5.1. Classical metal oxide-based catalysts

Classical metal oxide-based catalysts, such as Fe$_2$O$_3$, Co$_3$O$_4$, and MnO$_2$, are most well-established and extensively studied for decades. They are renowned for their thermal stability, redox flexibility, and cost effectiveness. These oxides typically possess high oxygen mobility and variable oxidation states, enabling efficient N$_2$O decomposition via lattice oxygen participation. Their simple structures allow for easy synthesis, scalability, and tunability through doping or morphology control. Spinel-type oxides, in particular, exhibit strong metal–oxygen interactions and good resistance to sintering. Despite their maturity, continued research enhances their surface area, dispersion, and durability under reaction conditions. Their robustness and versatility make them fundamental benchmarks in both industrial and environmental catalytic applications. Four categories of these catalysts are particularly important with respect to N$_2$O decomposition.

5.1.1. Metal oxide catalysts

Transition metal oxides, such as, NiO, Co$_3$O$_4$, MnO$_2$, CuO, Cr$_2$O$_3$ and Fe$_2$O$_3$, exhibit high catalytic activity for the decomposition of N$_2$O. The transition metal oxides are known for their high thermal and chemical stability, making them suitable candidates for catalytic applications[27-29]. For example, Gaidei and co-workers synthesized a series of oxide catalysts containing up to 30% active metal component on an alumina carrier. The temperature dependence of

Figure 2a. Natural and anthropogenic sources of N$_2$O (infamous laughing gas); **b.** Thermal and catalytic paths of N$_2$O decomposition; **c.** Functioning of Cu-exchanged zeolites in the selective catalytic reduction of NO$_x$ from mobile sources [167]. Reproduced with permission from American Chemical Society (Copyright © 2013) **d.** The advances in zeolite synthesis and characterization techniques for heterogeneous catalysis.

　　　　　　　　　　　　　　　　　　　　　　　　　　　　　　　ARTICLE

N_2O decomposition on these catalysts follow a well-defined S-shaped curve, similar to Pt family metals, but these transition metal oxide catalysts are somewhat less active than Pt-based catalysts. The catalytic activity of these metal oxide catalysts was ranked as follows in increasing order of decomposition temperature: $Fe_2O_3 < Cr_2O_3 < CuO < MnO_2 < NiO < Co_3O_4$. Among the catalysts based on non-noble metals, Co_3O_4 showed the highest catalytic activity. The calculated activation energy values for these catalysts vary, with CuO and Cr_2O_3 having the highest E_a (187–176 kJ/mol) and MnO_2, Co_3O_4 and NiO having lower values (133–143 kJ/mol). Based on experimental data, Co, Cu, Mn and Cr oxides are recommended as active components for developing deposited catalysts based on non-noble metals [30]. Figure 3 signifies the use of acidic and high valence metal sites on the various metal oxide catalysts based on MnO_x, CeO_2, Fe_2O_3, VO_x and CuO for the NH_3-assited SCR of NO_x [31].

CaO obtained from the domestic limestone has also demonstrated its catalytic effect in N_2O decomposition. Effects of CO and CO_2 on N_2O conversion activity were found antagonistic to each other. On

one hand, CO increases the N_2O decomposition activity. On the other hand, higher CO_2 concentrations slowly decrease the N_2O decomposition activity. As NO was also a hindering factor in N_2O decomposition, in order to lessen its concentration, N_2O was concurrently flew in the circulating fluidized bed combustion (CFBC) reactor. Selective non-catalytic reduction (SNCR) is a method of choice for the NO removal from flue gas [32]. Similarly, various Bi-based semiconductors were fabricated by hydrothermal strategy[33-35]. e.g. Liu group examined monoclinic $BiVO_4$, orthorhombic Bi_2MoO_6 and Bi_2WO_6 catalysts for the photocatalytic degradation of N_2O into N_2 and O_2, as shown in Figure 4a. They found that $BiVO_4$ exhibited highest degradation activity due to stronger absorption of visible light and higher charge separation [36].

Metal supported metal oxides catalysts are also popular for N_2O decomposition reaction. Komvokis *et al* synthesized series of Ru/Al_2O_3 nanocatalysts via *in-situ* reduction with ethylene glycol (EG) and compared their N_2O reduction activity with the catalysts prepared through the typical incipient wetness procedure. The EG
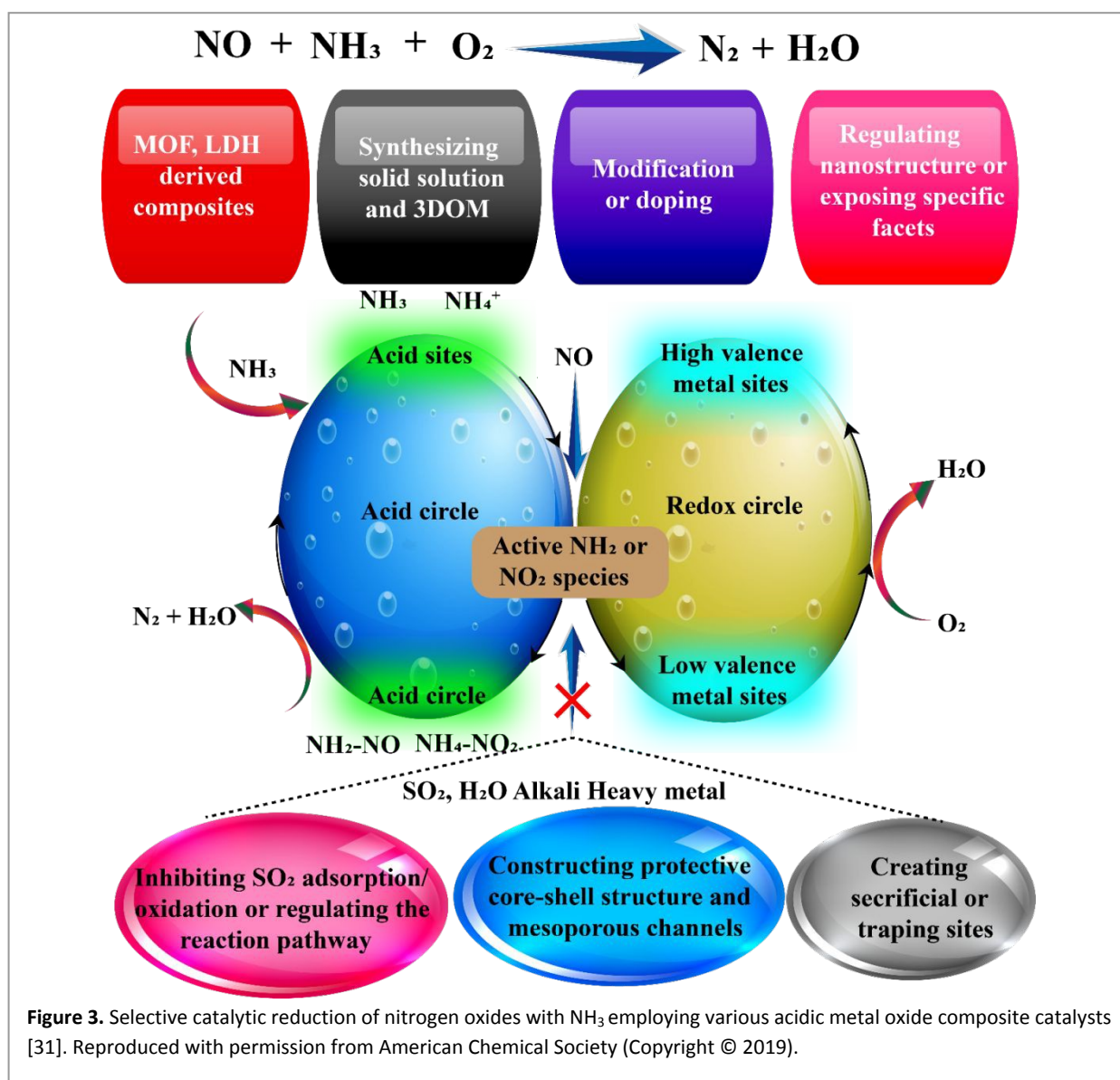

Figure 3. Selective catalytic reduction of nitrogen oxides with NH_3 employing various acidic metal oxide composite catalysts [31]. Reproduced with permission from American Chemical Society (Copyright © 2019).
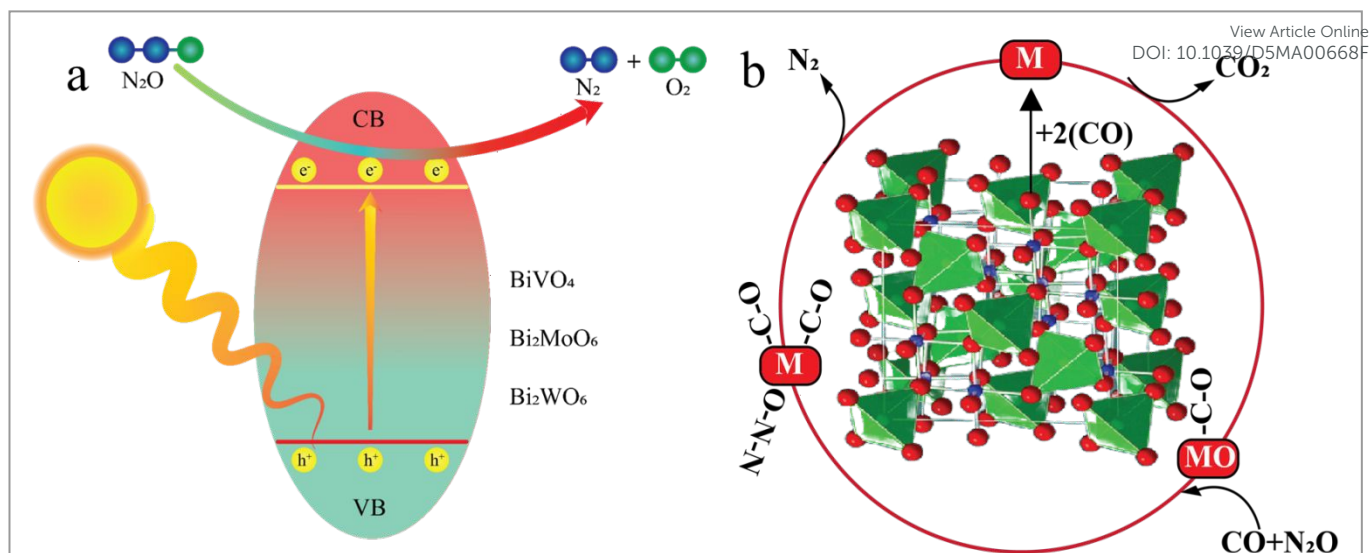
Figure 4a. Photocatalytic N_2O decomposition via Bi-based photocatalysts (i.e. $BiVO_4$, Bi_2MoO_6 and Bi_2WO_6) under visible light irradiation [36]. Reproduced with permission from American Chemical Society (Copyright © 2018). **b.** Mans–van Krevelen mechanism over phosphortungstic acid supported SACs for the reduction of N_2O by CO [39]. Reproduced with permission from American Chemical Society (Copyright © 2019).

reduction approach resulted in the formation of spherical Ru nanoparticles (particle size: 1–3nm; dispersion: 70–35%). While impregnated calcined catalysts had larger sized nanoparticles with very small dispersion degree (particle size: 10–80 nm; dispersion: 10%). The catalysts synthesized via EG reduction showed significantly higher N_2O decomposition activity in O_2 rich environment irrespective of CO, CO_2, NO, H_2O and SO_2. The higher surface area of Ru metal contributes to their higher catalytic activity. These catalysts have a low apparent activation energy, which suggest they require less energy to initiate the chemical reaction. Ru/Al_2O_3 nanocatalysts can be regenerated effectively that helps to restore their catalytic activity, achieving a conversion rate of over 90% [37]. Similarly, Reddya *et al* synthesized alumina-supported Pd catalysts (Pd/Al_2O_3) employing the deposition precipitation (DP) and impregnation (IMP) methods, and studied their effect on N_2O conversion activity. Higher catalytic efficiency was recorded for DP catalysts as compared to their IMP equivalents due to formation of partially oxidized Pd^{2+} species over the surface of the DP–Cl catalyst [38].

In a general N_2O decomposition reaction, CO is adsorbed over the surface of catalyst to reduce N_2O but this strong adsorption of CO may lead to the catalyst's poisoning. For example, Zhang *et al* have utilized Mans-van-Krevelan mechanism by employing phosphotungstic acid (PTA) supported single atom catalysts (SACs), M/PTA where M include = Fe, Co, Mn, Rh, Ru, Ir, Os, Pt and Pd. Adsorbed CO reacts with the surface oxygen atoms of PTA support and create holes on M/PTA surface. N_2O acts as oxygen donor to regenerate catalyst and releases N_2. It was also demonstrated that among all metals, Pd/PTA, Rh/PTA and Pt/PTA are most efficient catalysts. Figure 4b shows the mechanism for the reduction of N_2O by CO over M/PTA catalysts [39]. Metals like Co, Cu or Fe supported on ZrO_2 are also active in the decomposition of N_2O. The activity pattern

is Co > Cu >> Fe. ZrO_2 catalysts have the advantage of hydrothermal stability. Unlike that of zeolite systems, their catalytic activity is recovered when H_2O vapours are eliminated from the feed gas [40].

Tuti *et al* further investigated N_2O adsorption and decomposition on ZrO_2. At 25 °C, N_2O molecularly adsorbs through the O_2 end on Zr^{4+} sites and dissociative adsorption of N_2O occurs on surface defect sites, i.e. Zr^{3+} sites. It was noted that N–N bond dissociation did not occur and oxygen atoms of the lattice become incorporated into the product O_2 molecules [41].

In a different study, researchers have used a cluster model represented by the $M(OH)_3(H_2O)_2$, where M represents different transition metals such as Co, Fe and Rh. The results indicated that Rh and Co sites were more active for N_2O decomposition reaction as compared to Fe. The rate-limiting step is the formation of adsorbed O_2 molecules via the interaction of adsorbed oxygen atom with N_2O. A correlation was observed between the activation energy (E_a) and the strength of M–O bond. Weaker metal-adsorbed oxygen bonds for Co and Rh sites facilitated the decomposition of second N_2O molecule into O_2, lowering the activation barrier [42]. In the case of $Fe(OH)_3(H_2O)_2$, the transition state analysis suggested that N_2O dissociation was achieved through electron density donation from the metal to an N_2O molecule [43]. Various other examples of N_2O decomposing metal oxide catalysts have been provided in the Table 1.

Shortcomings of metal oxide catalysts: Though pure metal oxides show highest catalytic efficiencies in the cases of transition metal oxides of group VIII and some rare earth oxides (e.g. La), it is also worthwhile to note that, based upon experimental conditions, metal oxides including MnO_2, MnO, Cu_2O and CoO are not stable and are partially decomposed [44]. As a result, N_2O decomposition studies took

a turn towards the development of more active and stable catalytic systems. Another important fact about pure metal oxide catalysts is the utilization of high temperature for catalyzing N_2O decomposition because of the limited availability of active sites at low temperatures due to adsorbed oxygen recombination. In addition to this, presence of H_2O exerts a negative effect on catalytic efficiency due to its competitive adsorption on active sites [20].

Application scenario: nitric acid plants: Metal oxide catalysts, such as Co_3O_4, Fe_2O_3 and MnO_2 are low-cost, stable, and effective for N_2O decomposition under high-temperature conditions typical of nitric acid plant. They offer thermal robustness and environmental compatibility but require elevated activation temperatures, show reduced efficiency at intermediate ranges ad are vulnerable to deactivation by H_2O and SO_2 impurities.

5.1.2. Spinel oxides

Spinel oxides, having structural formula of AB_2O_4, show high thermal stability and redox activity. In several redox reactions such as, reduction of N_2O, oxidation of higher hydrocarbons and CO, cobalt spinel catalysts have been widely investigated [54]. It has been demonstrated that Co_3O_4 is more active in CO oxidation than Fe_2O_3, Cu_2O, NiO, MnO, V_2O_5, Cr_2O, CeO_2 and ZnO. Because of its capability to bind quickly with oxygen and a very low M–O bond energy, cobalt spinel is believed to display the highest activity in hydrocarbon oxidation [55]. Figure 5 represents synthesis and use of various metal spinels in different electronic materials (ORR and OER) [56].

Shen *et al* investigated the catalytic conversion of N_2O using cobalt oxide catalysts supported on various materials and synthesized using co-precipitation method. Among the supports tested, alkaline MgO was found to be the most effective due to its strong electron-donating properties. Here cobalt existed in the form of Co_3O_4 nanoparticles dispersed in the MgO matrix. Under specific conditions, the Co–MgO–15% catalyst demonstrated good activity on decomposing N_2O, making it a potential candidate for mitigating
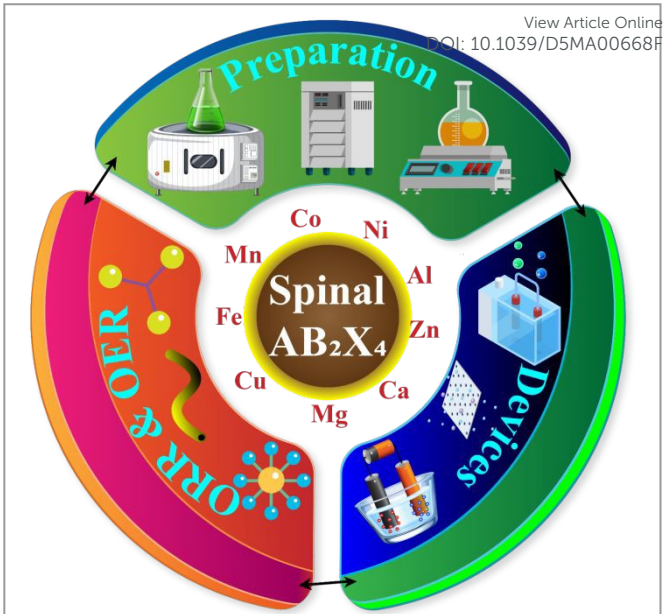

Figure 5. Synthesis routes and applications of spinel oxides (AB_2X_4) [55]. Reproduced with permission from American Chemical Society (Copyright © 2017).

greenhouse gas emissions from anthropogenic sources [57]. The advantages of using Co oxide-based spinel catalysts lie in their capability to decompose N_2O below 400 °C and sufficient catalytic activity. Another benefit of using spinel oxide catalysts containing Rh is that they exhibit unusual catalytic activities in the absence of water but these catalysts rapidly lose their activity upon exposure to water [58, 59].

Researchers have tried to find whether the catalytic activity of cobalt spinel oxide catalysts is influenced by the addition of gases such as NO_2, NO, O_2 and H_2O vapours or not. It has been found that operating the reaction at 850 °C led to a higher N_2O conversion compared to 800 °C.

Table 1. Overview of synthesis methods, reaction conditions and various techniques employed during the course of analysis of metal oxide-based catalysts for N_2O decomposition.

Catalysts	Method of preparation	Reaction atmosphere	Air speed (mL/min)	N_2O Decomposition Temp-range (°C/K)	Techniques used for characterization and activity of catalysts	Ref.
CaO catalysts	Hydrothermal	-	-	1073–1273 K	DFT method, On-line gas flue analyzer, GC	45
γ-Fe_2O_3	Co-precipitation	N_2	50	100–400 °C	XRD, XPS, FTIR	46
Al-doped MoS_2	-	Ethylene oxide	-	-	DFT	47
3.0 F–Co_3O_4	Sol-gel	Ar	50	250–450 °C	TEM, HRTEM	48
Ti_3O_6@TiO_2	-	-	-	-	DFT	49
Ni>Co>Fe>Cu	Impregnation	N_2	400	200–500 °C	DFT	50
Co_3O_4	Sol-gel	-	-	-	UV–visible spectra, H_2–TPR, XPS, TEM, EXAFS, EDS, NAP–XPS	51
$Sm_{0.1}$–Co_3O_4	Sol-gel	Ar	50	300–500 °C	XRD, XPS, STEM, EELS, H_2–TPR	52
N–doped Co_3O_4	Sol-gel	H_2/N_2	30	150–500 °C	FTIR, XRD, TEM, EDX, XPS, O_2–TPD	53

This improvement was attributed to the presence of O_2, which altered the oxidation state of Co in the catalyst [24]. However, at lower temperatures, the presence of O_2 reduced N_2O conversion. H_2O vapours also have a detrimental effect on the catalyst's activity at all temperatures. This was likely due to the competitive chemisorption of H_2O vapours on the active sites, hindering N_2O decomposition. Unlike O_2 and H_2O vapours, however NO_2 did not decompose over the cobalt catalyst and it did not impact the catalyst's state. It had no effect on N_2O conversion. On the other hand, the presence of NO in the feed gas mixture at 850 °C led to the higher N_2O reduction values. This was attributed to NO's influence on the process, possibly affecting the last phase of N_2O decomposition. The state of catalyst was also influenced by temperature variations, particularly when exposed to a feed gas mixture containing O_2, N_2O and Ar at temperatures ranging from 700 °C to 850 °C [60]. Extensive examples of the N_2O decomposition by spinel oxide catalysts have been enlisted in Table 2.

Shortcomings of spinel oxide catalysts: Spinel oxide catalysts often suffer from limited surface area and poor dispersion of active sites, reducing their catalytic efficiency. Their high-temperature synthesis can lead to particle sintering, decreasing reactivity. Additionally, some spinels exhibit slow oxygen mobility and reduced activity at low temperatures, limiting their applicability in mild reaction conditions. Stability under hydrothermal conditions can also be a concern.

Application scenario: Industrial flue gas treatment: Spinel oxides are attractive for N_2O decomposition in industrial flue gas streams due to their structural stability, redox flexibility and cost-effectiveness. They operate efficiently at high temperatures and tolerate thermal stress, but limitations include moderate activity at lower temperatures and susceptibility to poisoning by SO_2 and H_2O commonly present in flue gases.

5.1.3. Hydroxyapatites

Hydroxyapatites, having the formula $Ca_{10}(PO_4)_6(OH)_2$ act as dual catalysts in acid-base and redox catalysis. They enable moderate activity for N_2O decomposition. Their flexible structure allows ion substitution (e.g. with transition metals), enhancing catalytic sites. They exhibit good thermal stability and surface hydroxylation but generally require modification for high activity. Their tenability makes them suitable for multifunctional or hybrid catalytic systems under mild conditions. [61].

In 1990s, hydroxyapatite catalysts (containing calcium and phosphate ions) were employed for indirect N_2O decomposition via partial oxidation of methane [62, 63]. However, during the last few years, hydroxyapatites have been used as supports for Rh and Ru catalysts in N_2O abatement [64, 65]. Galloni *et al* evaluated Cu- and Fe-loaded hydroxyapatite catalysts for N_2O decomposition, revealing superior Cu performance due to nanoparticle formation, with detailed structural, stability and resistance analyses supporting catalytic behaviour [66]. Wei *et al*, obtained natural hydroxyapatite from bone and after doping it with Co ions, Co/nHAP catalysts were

prepared and utilized of the investigation of N_2O decomposition reaction [67]. Figure 6a shows the mechanistic pathway of N_2O reduction over Co/nHAP catalyst while Figure 6b indicates N_2O conversion profiles with respect to increasing temperature. Similarly, Tan *et al* synthesized a hydroxyapatite supported bimetallic (Fe, Rh) catalysts for plasma-assisted N_2O decomposition studies. In this instance, reaction temperature was lowered to a higher degree as free radicals generated by plasma initiated the catalytic decomposition reaction faster even at low temperatures [68]. Figure 6c & d indicates the mechanism and conversion profiles of N_2O. More examples are represented in Table 3.

Shortcomings of hydroxyapatite catalysts: These catalysts face several limitations, including relatively low intrinsic activity compared to conventional metal oxides. Their performance heavily depends on metal ion doping, as pure HAP is largely inactive. Additionally, achieving uniform dispersion of active sites can be challenging. They may also show reduced thermal stability under harsh conditions are susceptible to deactivation by sulphur or alkali contaminants without proper modification.

Application scenario: Wastewater treatment facilities: These catalysts offer tunable surface properties, ion-exchange capacity and good thermal stability, making them promising for N_2O decomposition in wastewater treatment off-gases. Their biocompatibility and low cost are additional advantages. However, they often show limited intrinsic activity, require modification with transition metals to enhance performance, and may suffer from deactivation under humid, impurity-rich gas conditions.

5.1.4. Mixed metal oxide catalysts

A lot of work has already been conducted on mixed metal oxide systems, e.g. metal-doped oxides and transition metal ions in inert matrices. Due to the unusual structure, thermal stability, synthesis at high temperature and low SSAs, the mixed metal oxides are famous for their N_2O decomposition activity [69]. Transition metal ions are very specific in their activity based on their oxidation state, e.g. MgO matrix dispersed Mn (III) ions showed the highest catalytic efficiency as compared to Mn (II) and Mn (IV) [70]. However, the supported oxides possess better practical applications than pure and mixed metal oxides because of higher dispersion of metal ions in the large surface areas of different well-known supports including alumina, mesoporous silica, zirconia, ceria and titania. The catalytic efficiency is determined by metal loading, method of synthesis, and temperature.

For the purpose of efficient N_2O abatement, mixed metal oxide catalysts are proved very effective catalysts[71-74]. Beyer *et al* studied the N_2O decomposition over different Rh supported metal and non-metal oxides, e.g. Rh/SiO_2, Rh/MgO, Rh/Al_2O_3, Rh/TiO_2 and Rh/CeO_2, both in the presence and absence of O_2. Rh/SiO_2 and Rh/MgO showed high catalytic activity for N_2O conversion, even at the low temperature in the presence of O_2. In Rh/Al_2O_3, Rh/TiO_2 and Rh/CeO_2, smaller sized Rh nanoparticles were abundant, resulting in

lower catalytic activities. The particle size of Rh was a crucial factor affecting the overall catalytic performance [75]. The redox properties of active Rh components were affected by the acid-base properties of the support. The reduction abilities of Rh species decreased as the basicity of the support increased, indicating a strong interaction of Rh species with O_2. Han *et al* employed mesoporous

$TiO_2@Fe_2O_3@Al_2O_3$ core-shell nanostructures for low temperature selective catalytic reduction of (SCR) of NO_x. It effectively prevented the deposition of sulphur compounds and accelerates the SCR of NO_x by facilitating electron transfer at the Fe_2O_3–TiO_2 interface. Figure 7a depicts the comparison of mechanisms for standard SCR with fast SCR these catalysts follow [76].

Table 2. Overview of synthesis methods, reaction conditions and various techniques employed during the course of analysis of different spinel oxide catalysts for N_2O decomposition.

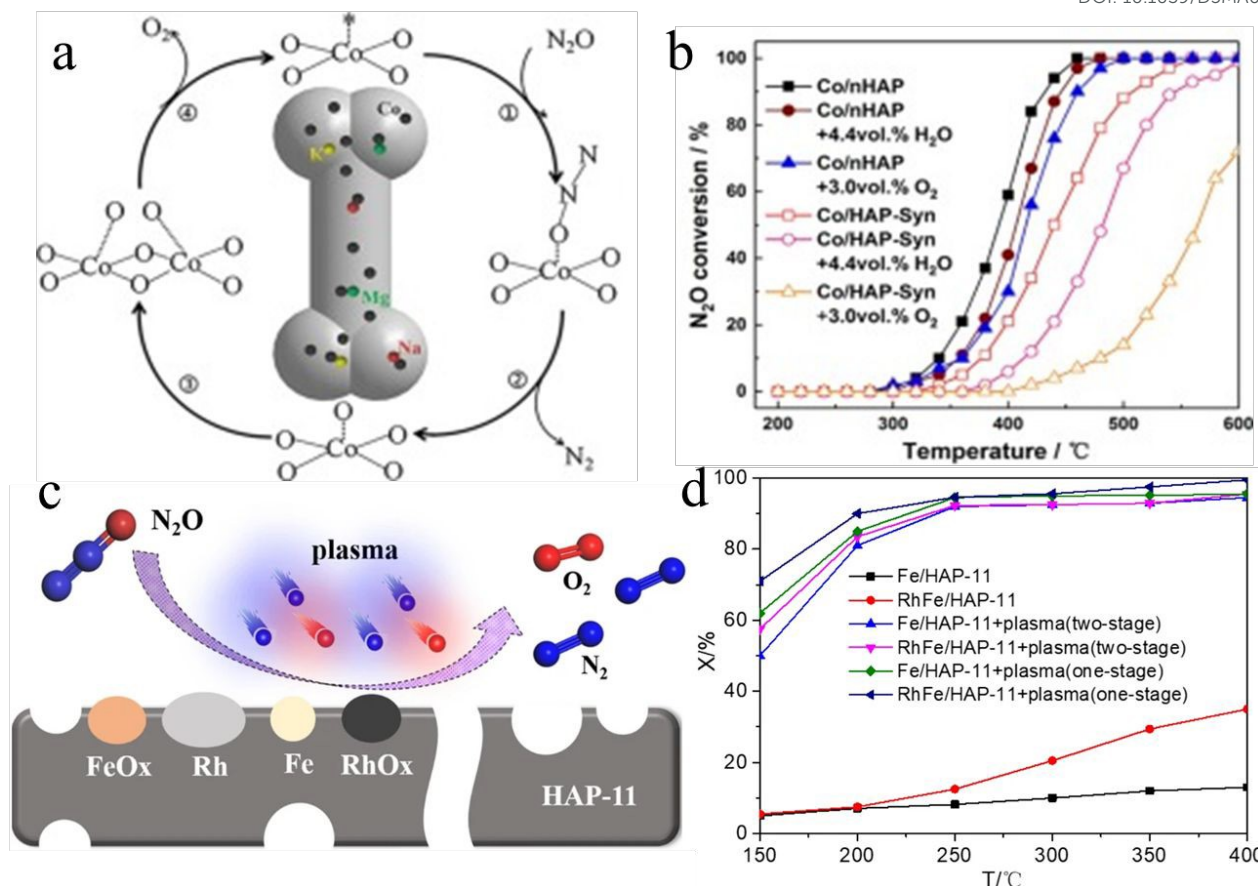| Catalysts	Methods	Reaction atmosphere	Air speed (mL/min)	N_2O Decomposition Temp-range (°C/K)	Techniques used for characterization and activity of catalysts	Ref.
Co/nHAP	Hydrothermal	Ar	-	200–600 °C	XRD, TEM, HADDF–STEM, XPS	67
(Co_3O_4) (CS–N)	Co-precipitation	-	-	100–400 °C	XRD	77
Co_3O_4	Hydrothermal	He	30	100–600°C	O_2–TPD, DFT calculations, XRD, FTIR, SEM, XRF, TPSR	54
Co_3O_4–based catalyst	Co-precipitation	N_2	50	400–600 °C	XRF, XRD, H_2–TPR, TEM, EDX, SAED	78
Cs–doped Co-spinel catalysts (Cs–Co_3O_4)	Wetness impregnation	-	-	< 200 °C	XRF, XRD, SEM, XPS, Raman, TPCR, QMS	79
deNOx and deN$_2$O	Precipitation	-	-	425–450 °C	FTIR	80
$Cu_xCo_{1-x}Co_2O_4$ spinel-oxide catalysts	Co-precipitation	N_2	200	150–500 °C	TGA, DTA, FTIR, XRD	81
Co_3O_4	PVA-assisted precipitation	N_2	65	300–600 °C	DFT, XRD, XPS, TEM, SEM, FTIR, EPR	82
Co_3O_4	PVA-assisted precipitation	-	-	150–450 °C	XRD	83
K-doped $Cu_xCo_{3-x}O_4$ catalysts	Thermal decomposition	O_2	20	250–650 °C	XRD, TGA, TPR, N_2–physisorption, O_2–TPD, ICP–OES, BET	84
Co–Mn–Al mixed oxide catalysts	Precipitation	H_2	50	40–450 °C	AAS, XRD, SEM, Raman, FTIR, TPR–H_2, TPD–N_2O, SEM, EDS, MS	85
Co-based spinel oxides	Impregnation	-	50	25–400 °C	XRD, BET, H_2–TPR, O_2–TPD, XPS	58
Ag_xCo (*x* = 0 ∼ 0.08) oxide catalysts	Co-precipitation	Ar	30	200–400 °C	XRD, TEM, O_2–TPD, BET, H_2–TPR, GC–TCD, XPS	86
Bi–Co_3O_4 catalysts	Co-precipitation	Ar	50	200–500 °C	O_2–TPD, BET, XRD, GC	87
Alien cations doped–nanocrytalline Co–spinel catalysts	Co-precipitation	He	30	100–600 °C	XRD, Raman, BET, XPS, H_2–TPR, TEM	88
LT–deN$_2$O catalysts (K/$Zn_{0.4}Co_{2.6}O_4$/αAl_2O_3)	Co-precipitation	-	-	405–445 °C	FTIR using on-line analyzer	89
$Zn_xCo_{1-x}Co_2o_4$ spinel catalyst	Co-precipitation	O_2	10	-	XRD, EDX	90
Co_3O_4–Cs	Wet impregnation	H_2	50	100–400 °C	XPS, SEM, H_2–TPR, XRD	91
Cd–Co_3O_4 spinel catalysts	Co-precipitation	-	-	-	TGA, DTA, XRD, FTIR, N_2–physisorption, AAS	92
N–doped Co_3O_4	Sol-gel method	H_2/N_2	30	200–500 °C	XRD, FTIR, Raman, N_2–physisorption, TEM, EDX, HADDF–STEM, H_2–TPR, O_2–TPD, EPR, CO_2–TPD	53
(CuMgNiZn)$_1$$Co_2O_4$ catalysts	Co-precipitation	H_2	50	150–500 °C	DFT, TPSR	93
Mn–Fe spinel catalysts	Co-precipitation	H_2	100	100–400° C	NH_3–TPD, NO–TPD, DRIFTS, FTIR, DFT	94

Materials Advances Accepted Manuscript

Figure 6a. Break down of N_2O over the surface of Co-doped bone-derived hydroxyapatite (Co/nHAP) catalysts; **b.** N_2O decomposition profile [67]. Reproduced with permission from Elsevier (Copyright © 2020). **c.** Mechanism of plasma-assisted N_2O degradation over the surface of bimetallic RhFe/HAP catalysts; **d.** Variation of % N_2O decomposition w.r.t. temperature on RhFe/HAP and Fe/HAP catalysts [68]. Reproduced with permission from Springer-Nature (Copyright © 2023).

Similarly, Gaidei *et al* also synthesized and compared N_2O decomposition activities of various Rh supported metal oxide catalysts i.e. Rh/ZrO_2, Rh/Al_2O_3 and $Rh/Al_2O_3–SiO_2$. The catalysts were exposed to an intimal temperature of 450 °C in a reactor. As a result they exhibited excellent dynamic characteristics to initiate and sustain reaction. The catalyst's activity decreased over time. Unloaded catalysts achieved 100% decomposition of N_2O within the temperature range of 460–480 °C that indicated its effectiveness in promoting decomposition reaction. X-ray analysis revealed the presence of phase transitions in carrier materials and oxidation of Rh during the operational time [95]. In yet another study, Ratanatawanate *et al* have devised a method that combined PbS QDs decorated TiO_2 nanotubes with S-nitosocysteine that released NO_2 that further produced singlet oxygen [96]. Whole setup for the attachment of PbS QDs with the surface of TiO_2 nanotubes and release of NO_2 is shown in Figure 7b.

Imamura *et al* investigated the impact of adding Praseodymium (Pr) to CeO_2 to investigate the catalytic decomposition of N_2O. They prepared a catalysts by incorporating Rh on Pr/CeO_2 composites.

These catalysts were then subjected to calcination at different temperatures. However, the presence of Pr alone did not significantly affect the catalytic activity. A significant acceleration in the N_2O decomposition rate was observed as the calcination temperature of the catalysts is increased. Notably, the catalytic performance of the Rh-supported composite oxides ($Pr–Rh/CeO_2$) calcined at 800 °C were found most effective [97]. One of the chief advantages of Rh-doped ceria catalysts is that they retain an exceptionally high catalytic efficiency even in the presence of oxygen and water. Because of the hydrophobic nature of Rh/CeO_2 catalysts, they are much less sensitive to moisture as compared to other catalysts [98]. In another investigation, Peck *et al* fabricated a series of CeO_2-supported Fe_2O_3 and Co_2O_3 catalysts along with increase in the metal loadings to determine monolayer surface coverage on CeO_2 support. It results in higher catalytic activities through the maximization of supporting metal-oxygen bonds. NO_x was reduced by CO in the presence of sufficient amount of O_2 [99, 100]. Figure 8 represents the overall layout of NO_x reduction by CO.

Journal Name

ARTICLE

Table 3. Overview of synthesis methods, reaction conditions and various techniques employed during the course of analysis of hydroxyapatite based catalysts for N_2O decomposition

Catalysts	Method	Reaction atmoshere	Air speed (mL/min)	N_2O Decomposition Temp-range (°C/K)	Techniques used for characterization and activity of catalysts	Ref.
Hydroxyapatite-supported RhO_x catalysts (RhO_x–HAP)	Wet impregnation	O_2	30	150–400 °C	XRD, TEM, ICP, XPS, BET, CO_2–TPD, O_2–TPD, GC, FT–IR	101
Hydroxyapatite-supported RuO_x catalysts (RuO_x–HAP)	impregnating	H_2/He	10	150–400 °C	ICP–OES, XRD, BET, TEM, XPS, CO_2–TPD, O_2–TPD, H_2–TPR, GC–TCD, QMS	64
Co/Hydroxyapatite	Hydrothermal	-	-	100–900 °C	XRD, TEM, HRTEM, EDX, STEM, UV-vis	102
Hydroxyapatite supported Rh, Fe, and Rh–Fe catalysts	impregnation	He	60	150–200 °C	XRD, SEM, TEM, TG, XPS, CO_2–TPD	68
Hydroxyapatite (HAP, $Ca_{10}(PO_4)_6(OH)_2$)	Hydrothermal	NO	15	400–450 °C	N_2–physisorption, XRPD, NH_3-titration, UV–DRS, Mössbauer, XPS, and EXAFS	103
Calcium hydroxyapatite (HAP, $Ca_{10}(PO_4)_6(OH)_2$)	Co-precipitation	-	-	120–800 °C	UV–DRS and Mössbauer spectroscopies, NH_3 titration, N_2–physisorption and XRPD	104
Apatites-supported Co_3O_4	Co-precipitation	H_2/N_2	30	300–600 °C	XRD, XPS, H_2–TPR, TEM, Raman, FT–IR	105

N_2O decomposition was also tested on mixed metal oxides containing noble metals (i.e. Pt and Pd) supported on various oxide materials. The type of support material has a significant impact on the initial decomposition of N_2O. Important support materials include SiO_2 and Al_2O_3. At a low temperatures (298 K), the Pt/SiO_2–Al_2O_3 catalysts showed relatively low activity compared to other catalytic systems. However, their activity boosted at higher temperatures (573 K). This suggested that the support material's influence on N_2O decomposition depends on the reaction temperature [106]. Another important aspect of the support effect is change in the N_2O conversion with pulse numbers. In most cases, N_2O decomposition exhibited steep decrease with increasing pulse number. However, Pt/SiO_2–Al_2O_3 catalysts showed exceptionally high N_2O conversion rates at the second and third pulses [107].

Rh, Ru, and Ir based mixed metal oxides exhibited the highest activity in decomposing N_2O. However these catalysts are susceptible to oxidation at high temperatures due to their oxidation potentials. Ru and Ir based metal oxide catalysts tend to form highly volatile oxides at elevated temperatures, leading to the loss of active metal components and a decrease in catalytic activity. Given its stability in the context of N_2O decomposition, Rh is recommended as the preferred active component for catalysts used in this reaction [108]. Table 4 presents various examples of mixed metal oxide catalysts utilized for N_2O abatement studies.

Shortcomings of mixed metal oxide catalysts: Mixed metal oxide catalysts, despite their tunable composition and synergistic effects, often suffer from limited control over active site uniformity and metal dispersion Their synthesis can lead to phase separation or

undesired crystallanity, reducing catalytic efficiency. Additionally some systems exhibit poor low-temperature activity and deactivation under long-term operation, especially in the presence of moisture or contaminants. Scalability and reproducibility also remain challenging for complex multi-metal formulations.

Application scenario: Nitric acid plant emissions: Mixed metal oxides are highly effective for N2O abatement in nitric acid plant emissions due to their synergistic redox properties, abundant oxygen vacancies and strong thermal stability. They are cost-efficient and tunable but challenges include maintaining long-term stability under fluctuating gas conditions and vulnerability to poisoning by SO_2 and water vapour.

5.2. Layered and framework structures

Layered and framework structure-based catalysts, such as zeolites, hydrotalcites and mesoporous silica-supported systems offer unique structural advantages for N_2O decomposition. Their well-defined pores and channels facilitate controlled diffusion and confinement of reactants, enhancing selectivity and activity. Transition metal ions incorporated into frameworks (e.g. Fe-ZSM-5) act as isolated redox centres, promoting effective N–O bond cleavage.

Hydrotalcites provide tunable acid-base sites and high dispersion of metal species upon calcination. These materials also support ion-exchange capabilities, allowing precise modifications of active sites. However, their catalytic performance can depend heavily on pore architecture, metal loading and thermal stability under reaction conditions. Three classes of this category include;

Materials Advances Accepted Manuscript

Figure 7a. Mechanism of SO$_2$-tolerant selective catalytic reduction of NO$_x$ with NH$_3$ employing mesoporous TiO$_2$@Fe$_2$O$_3$@Al$_2$O$_3$ monolith composites at low temperature [94]. Reproduced with permission from American Chemical Society (Copyright © 2019). **b.** Mechanism of NO$_2$ release via the combination of S-nitrocysteine with PbS quantum dots decorated TiO$_2$ nanotubes [96]. Reproduced with permission from American Chemical Society (Copyright © 2011).

xx

Materials Advances

Table 4. Overview of synthesis methods, reaction conditions and various techniques employed during the course of analysis of different mixed metal oxide catalysts for N_2O decomposition.

Catalysts	Methods	Reaction atmosphere	Air speed (mL/min)	N_2O Decomposition Temp-range (°C/K)	Techniques used for characterization and activity of catalysts	Ref.
Cu/CeO_2	Hydrothermal	H_2/Ar	25	300–450 °C	STEM–EDX, STEM–EELS, H_2–TPR, XPS, operando DRS–UV–Vis, DRIFTS, CO–DRIFTS	[109]
Rh/CeO_2	Hydrothermal	H_2/Ar	40	400 °C	CO–DRIFTS, N_2O–DRIFTS, MCT detector, IR	[110]
RuO_2/Al_2O_3	Wet impregnation	N_2	1000	25–300 °C	BET surface area measurement, XRD, FT–IR, DBD reactor	[111]
Ru/Al_2O_3	Impregnation	He	20	250–500 °C	-	[112]
$PrBaCoCO_3$	Hydrothermal	He	100	200–600 °C	XPS, BET, H_2–TPR, O_2–TPR	[24]
$Cu–Al–O_x$ mixed metal oxides	Co-precipitation method	He	100	300–450 °C	XRD, ICP–MS, N_2–physisorption, O_2–TPD, H_2–TPR, in-situ FT–IR and XAFS	[113]
Metal oxides supported Au–NPs (Au/M_xO_y) (M_xO_y: Al_2O_3, CeO_2, Fe_2O_3, TiO_2 and ZnO)	Deposition precipitation	He	10	400–700 °C	BET, XRD, SEM, HR–TEM, XPS, H_2–TPR, EDS, GC–TCD	[114]
Co_3O_4/CeO_2 mixed oxide catalysts	Hydrothermal	He	100	300–600 °C	BET, XRD, TEM, H_2–TPR, XPS, GC–TCD	[115]
K–modified Co–Mn–Al mixed oxides	Hydrothermal	He	50	250–450 °C	ICP, XPRD, H_2–TPR, CO_2–TPD, NO–TPD, XPS, N_2–sorption	[116]
Co_3O_4/ZrO_2	Hydrothermal	He	30	200–400 °C	XRD, TEM, HRTEM, N_2–physisorption, FTIR, XPS, O_2–TPD, H_2–TPR, GC, Raman	[117]
$K/Y_2O_3–Co_3O_4$	Co-precipitation	He/Ar	20	100–400 °C	BET, DTA	[118]
$Nd(Cu, Co)Al–O_x$	Co-precipitation	O_2/He	100	50–600 °C	XRD, BET, HRTEM, XPS, H_2–TPR	[119]
$Co_3O_4–LaCoO_3$	Co-precipitation	He	40	700–850 °C	XRD, BET, FTIR	[120]
$Mn_xCo_{1-x}Co_2O_4$	Co-precipitation	He	40	100–500°C	XRF, XRD	[121]
$LaFeO_3$	Hydrothermal	-	-	250–500 °C	XRD, EDX, XPS	[122]
MnO_x/TiO_2	Ultrasonic impregnation	N_2	1000	0–400 °C	XRD, EDX, SEM	[123]
$CuFeO_x$ thin-film catalysts	Adsorption	Ar	20	100–550 °C	XRD, EDX, XPS	[124]
MnO_2/MO_x (M = Al, Si and Ti)	Wet impregnation	He	60	120–280 °C	XRD, XPS, BET	[125]
MnO_x/TiO_2	Wet impregnation	-	-	100–300 °C	XRD, BET, HRTEM, XPS, H_2–TPR and NH_3–TPD	[126]
Pd/CeO_2	Hydrothermal	NH_3/He	20	100–400 °C	XRD, XPS, TEM, FEI	[127]
Pt/Co_3O_4	Incipient-wetness	$H2/Ar$	35	100–500 °C	XRD, SEM, TEM, TPO, TPR	[128]
MnO_x/TiO_2	Ultrasonic impregnation	$O_2/Ar/NO/NH_3$	1000	0–350 °C	XRD, SEM, XPS, BET	[129]
Cs-supported Co_3O_4 (Cs/Co)	Co-precipitation	Ar	100	100–300 °C	XRD, XPS, H_2–TPR	[130]
$Bi_{0.1}NiO_{1.15}$	Co-precipitation	N_2/O_2	3100	300–400 °C	XRD, XPS, H_2–TPR	[131]

Materials Advances Accepted Manuscript

CuO/CeO₂	Co-precipitation	-	-	300–550 °C	STEM, EDX, XRD	132
Pd/γ–Al₂O₃	Impregnation	N_2	6	550–350 °C	XRD, XPS	17
Rh/PTA	-			-	DFT	39
P@ SiC	Adsorption	-	-	-	DFT, PDOS	133
(SACs) M1/PTA (M = Fe, Co, Mn, Ru, Rh, Os, Ir & Pt; PTA = [PW12O40]³⁻)	Ion exchange	-	-	-	DFT	134
Fe–substituted La–hexaaluminate supported Ir catalysts	Microemulsion	He	50	384–450 °C	XRD, XPS, DRFTS	135
Rh/CeO₂	incipient wetness impregnation	Ar	30	300–500 °C	XRD, STEM, EDS, HRTEM, XPS, FTIR, DRIFTS	136

5.2.1. Hydrotalcites (Layered double hydroxides)

With structural formula of $[M^{2+}_{1-x}M^{3+}_x(OH)_2]^{x+}(A^{n-})^{x-}.yH_2O$, hydrotalcites (HTs) possess excellent anion exchange capacity and basicity [89]. Their advantages include improved stability, control and efficiency compared to other reaction systems. Because of their flexible structure, hydrotalcites-derived transition metal oxides are considered very active and selective catalysts, even far more efficient than zeolitic catalysts. They are also thermally very stable. When using hydrotalcite catalysts, N₂O decomposes below 500 K. Another benefit of calcined hydrotalcites is that they do not degrade at temperatures above 900 K, thus, the high stability makes the hydrotalcite-derived catalysts quite promising for practical applications. Higher calcination temperatures combined with alkali promoters (i.e. K) have a great enhancing impact on the N₂O decomposition activity. However, water and oxygen are strong inhibitors of the N₂O conversion performance [137].

The overall rate of N₂O decomposition reaction depends on the adsorption of N₂O molecules on the catalysts surface during the reaction. This adsorption is crucial step in the decomposition process. The rapid formation of O₂ led to the fast desorption of adsorbed oxygen, making active sites on the catalyst surface available for further adsorption of N₂O. As the result of fast adsorption and desorption processes, the overall rate of N₂O decomposition is higher. This led to the establishment of first-order rate equation w.r.t the concentration of N₂O [138].

Layered double hydroxides (LDHs) are successfully employed as starting materials for metal supported catalysts. Generally, they are synthesized via three distinct routes; (1) With elements of redox properties present in between the layer spacing, direct calcination and/or reduction of LDH precursors is required, (2) Within the LDH sheets, anionic exchange with the desired metal precursors is crucial, followed by calcination and/or reduction and (3) Pre-calcined LDH precursors are impregnated with different inorganic materials followed by calcination and/or reduction [139]. Figure 9a summarizes
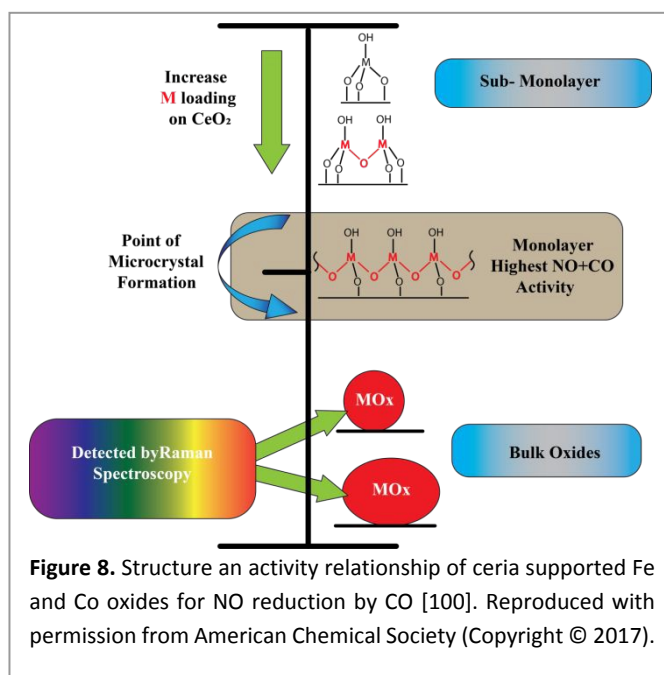

Figure 8. Structure an activity relationship of ceria supported Fe and Co oxides for NO reduction by CO [100]. Reproduced with permission from American Chemical Society (Copyright © 2017).

all three routes for the synthesis of LDH-derived metal supported catalysts.

Oxygen molecules tend to adsorb on the catalyst's surface and occupy the active sites, reducing the availability of free active sites for N_2O decomposition reaction. As a result, overall N_2O decomposition rate decreases. Eley–Rideal reaction, that involves the desorption of oxygen, is not active enough to drive the overall N_2O decomposition reaction within the temperature range of 250 °C and 500 °C. This behaviour of oxygen in N_2O decomposition process is different from selective catalytic reduction (SCR) processes where oxygen plays a key role in breaking down organic molecules to produce N_2 from nitrogen oxides [140]. A first-order reaction rate model can be employed to describe the decomposition of N_2O, but it is only applicable when the concentration of N_2O is less than 10,000 ppm. Beyond this range, reaction kinetics deviate from first-order

behaviour. Presence of impurities in the feed gas can get adsorbed on the active sites of the catalysts resulting in free defect sites on the surface which can slowly decrease the rate of N_2O decomposition [20]. De Stefanis *et al* used catalysts consisting of alumina-pillared smectites which are type of layered clay material. These clay materials were exchanged with transition metals [141]. The main focus of this study was to reduce N_2O through an eco-friendly decomposition reaction:

$$N_2O \rightarrow N_2 + 1/2O_2$$
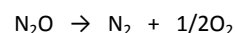
This reaction converts N_2O into less harmful nitrogen (N_2) and oxygen (O_2). The results of this study showed that when pillared clays were exchanged with transition metals, the yield of decomposition reaction increased suggesting that catalysts with transition metals are effective in promoting the N_2O decomposition rate. It was noted
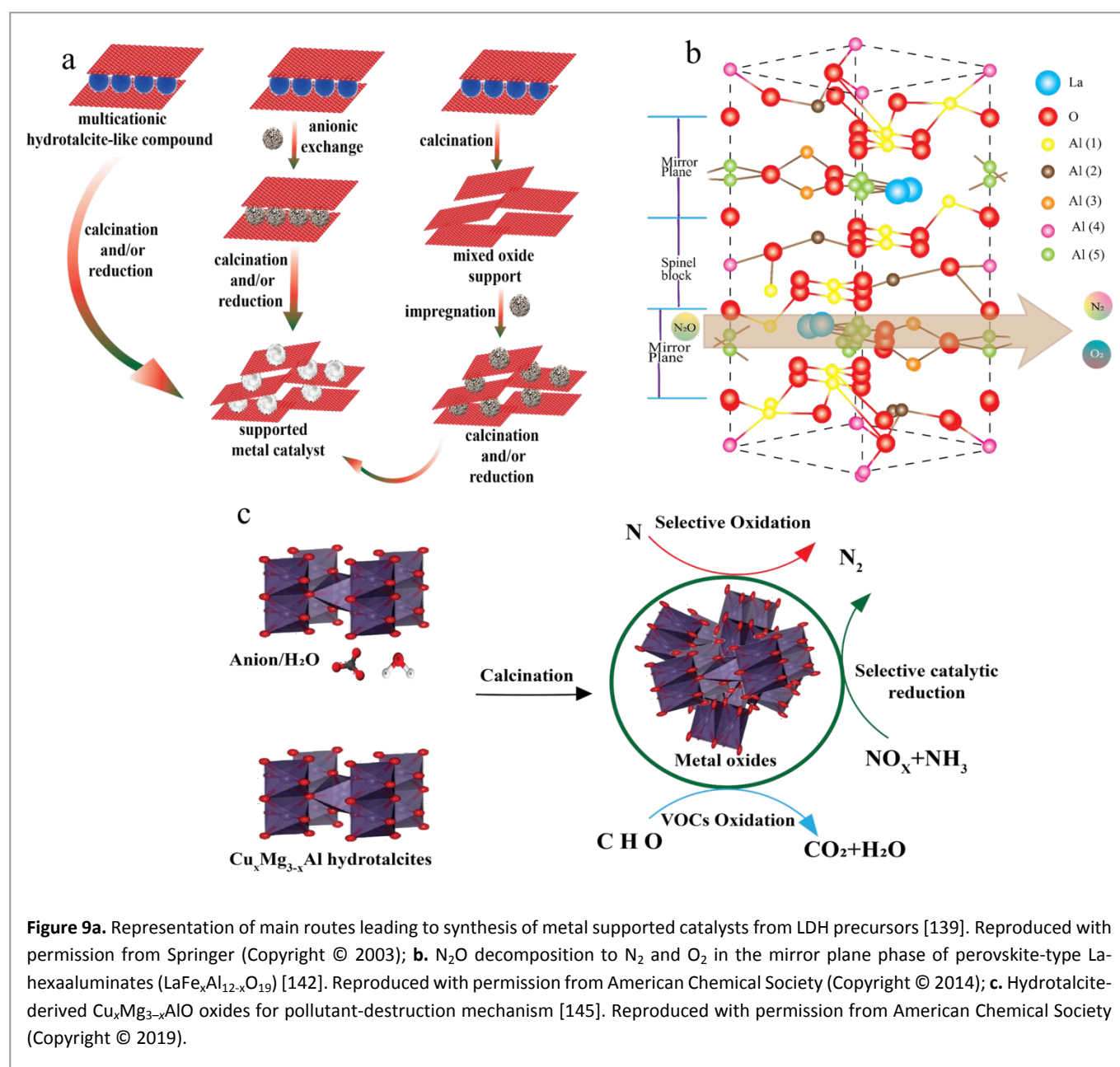
Figure 9a. Representation of main routes leading to synthesis of metal supported catalysts from LDH precursors [139]. Reproduced with permission from Springer (Copyright © 2003); **b.** N_2O decomposition to N_2 and O_2 in the mirror plane phase of perovskite-type La-hexaaluminates (LaFe$_x$Al$_{12-x}$O$_{19}$) [142]. Reproduced with permission from American Chemical Society (Copyright © 2014); **c.** Hydrotalcite-derived Cu$_x$Mg$_{3-x}$AlO oxides for pollutant-destruction mechanism [145]. Reproduced with permission from American Chemical Society (Copyright © 2019).

that double-exchanged alumina-pillared montmorillonite/beidellite catalysts, exchanged with Ca and Co ions, exhibited the highest decomposition activity for N_2O. Overall mechanism suggested that N_2O is first adsorbed on the catalyst surface. Then it underwent decomposition through catalytic oxidation and reduction [141]. Similarly, Zhang *et al* synthesized La-hexaaluminates (LaFe$_x$Al$_{12-x}$O$_{19}$) having abundant Al sites in the mirror plane (MP) phase so that degradation of N_2O can be achieved efficiently. Figure 9b demonstrates that Fe(III) ions prefer to occupy octahedral Al(III) sites in the MP of aluminate crystals confirming a high activity for N_2O decomposition [142]. Kiss *et al* reported AlFe–PILC type catalysts having different metal/OH ratios and employed them for N_2O decomposition reactions [143]. N_2O was 100% converted into N_2 and H_2O on treatment with NH_3 below 500 °C. However, in the direct conversion of N_2O below 500 °C, activity of catalysts did not exceed 40%. For N_2O abatement reaction, the catalytic activities of AlFe–PILC type catalysts prepared with higher metal/OH ratios are higher relative to the apparent activity of AlFe–PILC type catalysts having lower metal/OH ratios. It is attributed to the presence of free FeO–Fe$_2$O$_3$ particles [144].

Hydrotalcites have been effectively utilized for dual decomposition of volatile organic compounds (VOCs) and gaseous pollutants. For instance, fabricated and calcined Cu$_x$Mg$_{3-x}$AlO were examined for 100% primary catalytic oxidation of n-butylamine and 83% secondary catalytic reduction of NO$_x$ at a lower temperature of 350 °C, as represented in Figure 9c [145]. In another study, catalytic decomposition of N_2O was estimated at Co/Al hydrotalcites, [Co$_{1-x}$ Al$_x$(OH)$_2$[CO$_3$]]$_{x/2}$.H$_2$O (where x ≈ 0.25–0.33), in a static glass reactor at pressure of ≈50 Torr within the temperature range of 150–280 °C. Catalysts exhibited a first-order dependence for the N_2O decomposition activity. An increase in Co concentration led to an increased decomposition activity. A higher activity was shown by the catalyst precursor synthesized under a low saturation (LS) method than that synthesized by a sequential precipitation (SP) method [146]. Table 5 presents various examples of hydrotalcites that have been applied for N_2O decomposition.

Shortcomings of hydrotalcite catalysts: Hydrotalcite catalysts, while offering tunable composition and high dispersion of active sites, suffer from several drawbacks. Their thermal stability is limited, as structural collapse can occur upon high temperature calcination. The resulting mixed metal oxides may exhibit low surface area and poor

crystallinity. Additionally, their activity in N_2O decomposition is generally moderate, requiring further modifications. Sensitivity to water and contaminants can also affect long-term performance and catalyst durability.

Application scenario: Automotive exhaust control: These catalysts with layered double hydroxide structures, offer high surface area, tunable composition, and excellent dispersion of active metal sites, making them promising for N2O decomposition in automotive exhaust systems. They are low cost and versatile but disadvantages include limited intrinsic activity, dependence on metal modification for efficiency and reduced stability under high-temperature, water and sulphur-rich exhaust conditions.

5.2.2. Zeolites with transition metal ions

Zeolite catalysts are among the few early known catalysts for N_2O decomposition while some show catalytic activities below 600 K [147]. The activity of transition metal ion exchanged zeolite is determined by type of transition metal ion (TMI) and zeolite. This is the reason that the activity order for different transition metals in zeolite catalysts differs considerably from other metal oxide catalysts. One major advantage associated with zeolite catalysts is that the higher oxygen concentration shows a very small inhibitory effect on their catalytic efficiency, but one disadvantage associated with Rh-exchanged zeolites is their extreme sensitivity to water [59].

Transition metal ions in zeolites, supported on oxides, or dispersed in solid solution, are very active for N_2O decomposition [148, 149]. Numerous zeolites with transition metal ions are extensively studied in heterogeneous catalysis. A zeolite's ion-exchange capacity (IEC) depends on how it is chemically composed. A higher IEC is perceived in the zeolites having low SiO$_2$/Al$_2$O$_3$ ratios. Specific ion-exchange capacity of a zeolite varies by varying the structure of zeolite and cation exchanged. When a wet ion exchange (WIE) method was used for the preparation of Fe–ZSM–5, Lobree *et al* were able to achieve only half of the complete IEC without getting small iron oxide particles [150].

Natural zeolites show low activity for the catalytic reduction of N_2O using NH_3 due to the complex structures of zeolites [151]. However, when natural zeolites were modified with Fe, their activity in the SCR of N_2O became comparable to synthetic zeolites. It was found that highest activity of N_2O decomposition was achieved when natural zeolites contained 6.5 wt% Fe.

Table 5. Overview of synthesis methods, reaction conditions and various techniques employed during the course of analysis of different hydrotalcite catalysts for N_2O decomposition.

| Catalysts	Preparation method	Reaction atmosphere	Air speed (mL/min)	Decomposition Temp-range (°C/K)	Techniques used for characterization and activity of catalysts	Ref.
Mn(Fe)CoAlO$_x$ hydrotalcite	Co-precipitation	N$_2$	100	100–500 °C	XRD, H$_2$–TPR, TGA, XPS, XAFS, BET	152
Ru/Me$_x$O$_y$	Hydrothermal	-	-	300–550 °C	CO$_2$–TPD, TEM	153
Rh/Mg/Al HT–derived film	Co-precipitation	H$_2$/Ar	30	50–500 °C	SEM, EDX, TEM, SAED, BET, Raman, H$_2$–TPR, XPS	154
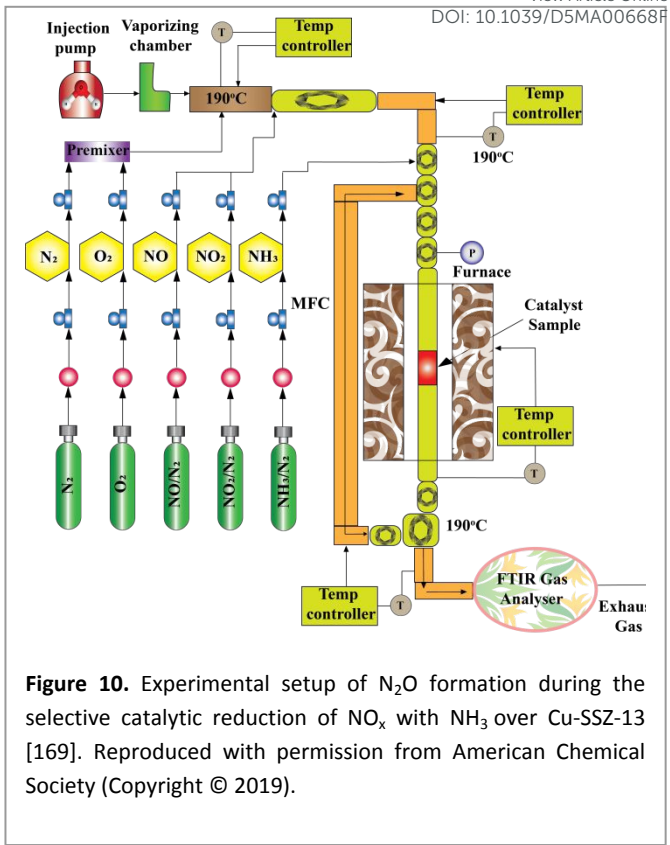
Figure 10. Experimental setup of N_2O formation during the selective catalytic reduction of NO_x with NH_3 over Cu-SSZ-13 [169]. Reproduced with permission from American Chemical Society (Copyright © 2019).

Hydrotalcite-derived Cu_xCo_y (CuO–Co_3O_4 mixed oxides)	Co-precipitation	N_2	100	350–500 °C	XRD, XPS	155
Hydrotalcite-derived mixed oxides	Ion exchange	H_2	200	300–500 °C	XRD, XPS, BET	156
Hydrotalcite-derived Co_3O_4, Co_3O_4–P	Sol-gel method	-	-	150–400 °C	TEM, TGA, XRD and BET	157
Hydrotalcite-derived [y = Cu/(Cu + Ni)]	Co-precipitation	H_2/Ar	41	600–900 °C	XRD, XPS, TGA–DTA, BET, XPS	158
CoCuAl mixed oxides derived from hydrotalcites	Solid phase	H_2/Ar	60	150–350 °C	XRD, N_2–physisorption, H_2–TPR	159
Al@Cu–based hydrotalciteCuAl–HT–c and Cu–P	Co-precipitation	NO/He	8	450–600 K	XRD, TPR and *in–situ* XANES	160
		CO/He	8			

Natural zeolites prepared with $FeCl_2$ as the precursor exhibited the higher activity for the reduction of N_2O due to the formation of more reducible Fe species with $FeCl_2$ [151]. Zeolites prepared with $FeSO_4$ as the precursor showed considerably lower activity for decomposition of N_2O as surface sulphate ions were identified as inhibitors, and their presence shifted the reaction temperature to higher values. It is suggested that natural zeolites especially when modified with Fe, can serve as a cost-effective alternative for catalysing the SCR of N_2O as they demonstrated comparable activity to synthetic zeolites [161,162].

Most active catalysts for N_2O decomposition are usually inhibited by NO. This suggests that NO can interfere with the process of breaking down N_2O into less harmful components. However, interestingly

enough, NO can significantly enhance the rate of N_2O decomposition over a specific catalyst, Fe–ZSM–5. Pérez-*Ramírez et al.* were first to report this positive effect of NO on N_2O decomposition over Fe–ZSM–5. They proposed a mechanism where NO in the gas phase combines with both the N_2O and adsorbed O_2, leading to the regeneration of active sites and the production of nitrogen oxide. This mechanism explains the increase in the N_2O decomposition rate due to NO [60]. On the other hand, Li and Armor reported that zeolites exchanged with Co or Cu ions were effective catalysts for N_2O decomposition, and that metal ions (particularly Co, Cu, Fe) in ZSM–5 were far more active than the same ions on Al_2O_3 [163]. On Cu–ZSM–5, Fe–ZSM–5 and Co–ZSM–5, the N_2O decomposition rate was proportional to the exchange extent. The existence of excess O_2, left the catalytic activity of Co–ZSM–5 unchanged and slightly decreased

Cu–ZSM–5 activity, but enhanced the catalytic activity of Fe–ZSM–5 [164]. Conversely, H_2O present in the feed strongly affected the catalytic activity of zeolites and led to irreversible deactivation because of its heterolytic adsorption on active sites. In the presence of water vapours, Co–ZSM–5 was more stable than Cu–ZSM–5 and Fe–ZSM–5 [165]. For the decomposition of N_2O into its elements, TMI exchanged pentasil-zeolites are recognized as most appropriate catalysts. Among the samples investigated, the highest N_2O decomposition activity was displayed by Cu–ZSM–5 catalysts [166]. Because of this reason, Deka et al have carried out an extensive investigation on the use of Cu-exchanged zeolite based catalysts (that include zeolite Y, ZSM-5, SSZ-13 and zeolite beta) for the abatement of NO_x present in the exhaust emissions of light and heavy duty vehicle engines [167]. However, Cu-ZSM-5 have a tendency to lose activity in the presence of H_2O vapours limiting its use in practical applications. However, Fe-containing zeolites are less sensitive towards H_2O vapours in comparison to Cu-containing zeolite [168]. Liu *et al* studied N_2O formation using Cu-SSZ-13 zeolites via the NH_3-asssited SCR of NO_x. All reactions were performed in a flow reactor system, as shown in Figure 10. It was found out that N_2O formation occurred through two entirely different mechanisms at low and high temperatures. At low temperature, N_2O was released due to the decomposition of NH_4NO_3 on Cu-SSZ-13 zeolite, while high temperatures favoured NH_3 oxidation route for N_2O formation [169].

Yasumura *et al* demonstrated an efficient strategy for the dispersion of metal species to design single atom catalysts. Chabazite (CHA) zeolites precursors were utilized as templates to disperse bulk Pd atoms into its small pores [170]. At 600 °C, flow of feed gas was regulated in a way so that Pd atoms present on the outside of CHA zeolites can get dispersed introducing Pd(II) ions into the pores of zeolite forming Pd-CHA zeolites along with the formation of N_2O. Figure 11a illustrates the conversion of bulk Pd and CHA zeolites into Pd(II) intercalated zeolite.

It has been observed that adsorbed NH_3 leaves the active sites by reaction with the surface O_2. Because NH_3, as a reducing agent, preferably reacts with O_2, N_2O decomposition process becomes suppressed due to presence of surface O_2. As the result, a vast majority of studies on SCR of N_2O have been devoted to Fe-exchanged zeolite catalytic systems, more specifically, the Fe–BEA catalysts [171, 172]. The N_2O abatement by NH_3 follows Mars and Van Krevelen mechanism that involves an oxidation-reduction cycle of interchange between two oxidation states of Fe ($Fe^{3+} \leftrightarrow Fe^{2+}$). In this scenario, N_2O reduction into oxygen surface species occurs over some definite Fe-sites which lead to a simultaneous N_2 release. Consequently, O_2 has no inhibitory influence on N_2O decomposition through NH_3 [173]. In Figure 11b, it can be noted that the presence of O_2 does not hinder the conversion of N_2O. In fact, there was small improvement in N_2O conversion when O_2 was present. This suggested that O_2 did not negatively impact the conversion of N_2O. Figure 11d demonstrated that the enhanced reduction of N_2O was associated with the oxidation of NH_3, which could change the NH_3/N_2O stoichiometry. In the absence of O_2, the highest N_2O

conversion occurred at around 3500 ppm of NH_3 concentration. In contrast, in the excess of O_2, the highest N_2O removal occurred at around 4000 ppm of NH_3 concentration. This also suggested that O_2 did not significantly interfere with N_2O decomposition and did not efficiently react with NH_3. Figure 11c indicates that the oxidation of NH_3 by O_2 was much less significant when N_2O was present compared to when N_2O was absent. This suggested that in the reaction system involving N_2O, NH_3 and O_2, the selective catalytic reduction (SCR) of N_2O by NH_3 was more dominant than the oxidation of NH_3 by O_2. Figure 11e shows that when NH_3 is oxidized by O_2, it produces large amount of NO, NO_2 and N_2O. However, in the $N_2O + NH_3 + O_2$ reaction system, only N_2 is detected as the main product. This indicated that NH_3 can be oxidized by both O_2 and N_2O, but N_2O is much more reactive than O_2, and their reaction pathways are distinct [174].

Ju *et al* have found that UV irradiation of the Pb^{2+}–ZSM–5 catalyst led to the decomposition of N_2O at 298 K in a linear manner with the irradiation time [175]. It can be confirmed by observing the yield of N_2 that increases as a function of the UV-exposure time, while under dark conditions, the formation could not be noticed. The yield of N_2 also increases when the amounts of Pb^{2+} loading becomes higher. It was reported that the photocatalytic decomposition of N_2O proceeds much more efficiently in the presence of propane [130]. In addition to the N_2 evolution, this reaction also led to the formation of oxygen-containing compounds such as ethanol and acetone. It was indicated that the efficient decomposition of N_2O proceeds photocatalytically in the presence of propane on the Pb^{2+}–ZSM–5 catalysts. The efficiency of the photocatalytic reduction of N_2O is found to be strongly dependent on the type of hydrocarbons used, e.g. methane or ethane, and among the hydrocarbons, the highest enhancement in the reaction rate is shown by propane. These results can be attributed to the observation that during the reaction, oxygen atoms formed by the photodecomposition of N_2O detach more easily from the isolated Pb^{2+} ions in the presence of propane [175]. Similarly, Co-based BEA zeolite catalysts were also used to study the oxidative dehydrogenation of propane (C_3H_8) with N_2O or a mixture of N_2O and oxygen (O_2) as the oxidants. N_2O is more selective but less active compared to O_2 as an oxidizing agent. Increasing the concentration of N_2O in the reaction mixture with C_3H_8 and O_2 led to the substantial increase in propane conversion while maintaining a constant selectivity for propene. The combination of O_2 and N_2O had a synergistic effect, resulting three-fold higher yield of propene compared using O_2 and N_2O alone [176]. Table 6 summarizes various examples of catalysts used along with the techniques applied during the course of analysis for the purpose of N_2O decomposition.

Shortcomings of zeolite catalysts: Zeolite catalysts, despite their well-defined microporous structures and strong metal-support interactions, have notable limitations in N_2O decomposition. Their narrow pore sizes can restrict diffusion of reactants and products, especially at higher conversions. Metal ion exchange may lead to non-uniform dispersion or clustering, reducing active site accessibility. Thermal stability under prolonged high-temperature reactions can be a concern, leading to framework degradation.

Materials Advances

Additionally, zeolites are sensitive to water vapours and contaminants like sulphur, which can cause deactivation and limit their industrial applicability.

Application scenario: Diesel vehicle exhaust mechanism: These catalysts are highly effective for N_2O decomposition in diesel exhaust due to their high surface area, tunable acidity and excellent

hydrothermal stability. They enable selective catalytic reduction with NH_3, offering high efficiency at medium temperatures. However, they are sensitive to sulphur poisoning, may deactivate under prolonged hydrothermal stress, and require careful formulation for durability.

Table 6. Overview of synthesis methods, reaction conditions and various techniques employed during the course of analysis of different zeolite catalysts for N_2O decomposition.

Catalysts	Preparation method	Reaction atmosphere	Air speed (mL/min)	Decomposition Temp-range (°C/K)	Techniques used for characterization and activity of catalysts	Ref.
Co−, Cu− and Fe−SSZ−13 zeolites	Hydrothermal	N_2	10	300–530 K	XRD, FT−IR, H_2−TPR, N_2O−TPR	26
		H_2/Ar	30			
Rh−ZSM catalysts	Incipient wetness	He/Ar	70	250–450 °C	STEM, XPS, TPR, N_2O-DRIFTS	98
CoMnAl HTC catalysts	Co-precipitation	He	25	330–460 °C	SEM, EDX, XRD, NH_3−TPD, CO_2−TPD, H_2−TPR, BET	148
Cu−ZSM−5 catalysts	Ion exchange	NH_3/He	30	200–600 °C	BET, XRD, TEM, CO_2−TPR, NH_3−TPR, GC−TCD	177
Fe−ZSM−5	Hydrothermal	He/Ar	15	550–750 K	N_2O−TPD, O_2−TPD, NO−TPD, AAS	178
Co−ZSM−5	Hydrothermal	He/O_2	25	380–500 °C	SEM, XRD, NH_3−TPD, H_2−TPR, ICP−AES, UV−Vis−DRS, DFT	179
Co/zeolites (Co/Beta, Co/mordenite, Co/ZSM−5, Co/MCM−49, Co/ZSM−23, Co/SSZ−13)	Wet impregnation	N_2	30	200–450 °C	XRD, BET, NH_3−TPD, H_2−TPR, XPS UV−Vis−DRS,	180
Fe−, Co−, Ni− and Cu−ZSM−5 catalysts	Ion exchange	Ar	4	400–800 °C	DFT, TPR	149
Fe, Co and Ni−exchanged Na−MOR catalysts (Fe−MOR, Co−MOR and Ni−MOR catalysts)	Ion exchange	O_2/He	100	293–773 K	GC, TCD, FID, _operando_ FTIR equipped with MCT detector	181
Cu/ZSM−5 catalysts	Adsorption	N_2	40	250–500 °C	ICP−AES, UV−Vis−DRS, H_2−TPR, N_2O−TPD	182
Cu−ZSM−5 catalysts	Adsorption	-	-	-	DFT	183
Fe−zeolites (Fe−PST−7, Fe−LTA, Fe−RTH, Fe−SSZ−13, Fe−FER, Fe−ZSM−5)	Hydrothermal	He	55	600–850 °C	XRD, SEM, TEM, BET, UV−vis, ESR, FTIR, NMR	184
Cu−ZSM−5 catalysts	Hydrothermal	-	-	600–800 K	H_2−TPR, IR	185
Cu−ZSM−5 catalysts	Ion exchange	N_2O/N_2	300	350–450 °C	H_2−TPR, IR, BET, H_2−TPR, TPD, FESEM, EDX	156
Cu−, Ni−, Zn−, Co−, Fe− and Mn−ZSM−5 catalysts	Ion exchange	N_2	300	50–300 °C	DFT, N_2O−TPD, GC−TCD, FT−IR, BET, ICP−OES	186
Fe−ZSM−5 catalysts	Wet impregnation	N_2	30	250–550 °C	XRD, XPS, BET, HRTEM, UV−Vis−DRS, XPS, H_2−TPR, TPO, DRIFTS	187
Cu/HZSM−5 catalysts	Wet impregnation	N_2	60	620 K	FTIR, XPS, XPRD	188
Co/HZSM−5 catalysts	Citric acid impregnation	O_2/Ar	80	300–450 °C	XRD, TG−DSC, Raman, SEM, H_2−TPR, XPS, EPR, FTIR, DRIFTS	189
Fe−ZSM−5 catalysts	Hydrothermal	N_2	20	300–600 °C	XRD, SEM, BET, UV−Vis, FTIR	190
Fe−ZSM−5, Fe−Beta, Fe−FER catalysts	Wet impregnation	He	70	200–400 °C	FTIR, BET, H_2−TPR, TGA−MS	191
Fe−beta, Fe−ZSM−5 and Fe−SAPO−34 catalysts	Ion exchange	H_2/Ar	30	200–400 °C	UV−vis−DRS, H_2−TPR	192

Materials Advances Accepted Manuscript

|						
Fe–SSZ–13 catalysts	Ion exchange	He	103	400–600 °C	ICP–AES, BET, UV–Vis–DRS, XRD, TEM, On-line GC–TCD	193
Fe/CHA catalysts	Ion exchange	N_2	80	160–550 °C	XRD, ICP–OES, DFT, TEM, EDX, XPS, EPR, FTIR, H_2–TPR	194
Fe-modified MCM–22 zeolite and its derivative ITQ–2 catalysts	Ion exchange	Ar	10	200–600 °C	XRD, ICP–OES, UV–Vis–DRS, H_2–TPR, HRTEM	161
(Co, Fe)–ZSM–5 and (Co, Fe)–beta catalysts	Ion exchange	Ar	30	25–600 °C	XRD, H_2–TPR, UV–Vis, TCD	165
Cu/SSZ–13, Cu/SSZ–5, Cu/BEA	Ion exchange	O_2	2	100–500 °C	XRD, BET, DRIFTS, FTIR, H_2–TPR, NH_3–TPD	195
Co(x)/PRSA catalysts	Impregnation	O_2	20	348–438 °C	XRD, BET, H_2–TPR, NH_3–TPD, XPS, XRF, DRIFTS	196
Fe–FER catalysts	impregnation	$NO/O_2/H_2O$	350	200–900 °C	XRD, BET, SEM, UV–Vis–NIR, FTIR, Mössbauer spectroscopy	197
Fe zeolite catalysts	Diffusion impregnation	He	20	-	UV–Vis–NIR, FTIR, Mössbauer spectroscopy	198
Zeolite 5A, 13X and ZSM–5 catalysts	Wet impregnation	N_2	300	298–358 K	N_2O–TPD, BET, isosteric heat of adsorption	199
Cu/SSZ–13 catalysts	Hydrothermal	$NO/NH_3/ CO_2/H_2O/ NO_2/N_2O$	800–1500	200–600 °C	XRD, BET, ICP–OES, UV–Vis–DRS, H_2–TPR, HRTEM	200
Fe/BEA	Ion exchange	N_2	300	350–380 °C	XRF	201
Fe–MOR and Fe–FER	Hydrothermal	O_2/He	100	0–350 °C	FTIR, UV–vis	202
Fe–FER	Hydrothermal	-	-	500–900 °C	XRD, SEM, FTIR	203
Zeolite-based Fe catalysts	Ion exchange	$NO/O_2/H_2O/ He$	350	400–800 °C	XRD, FTIR, TPD	204
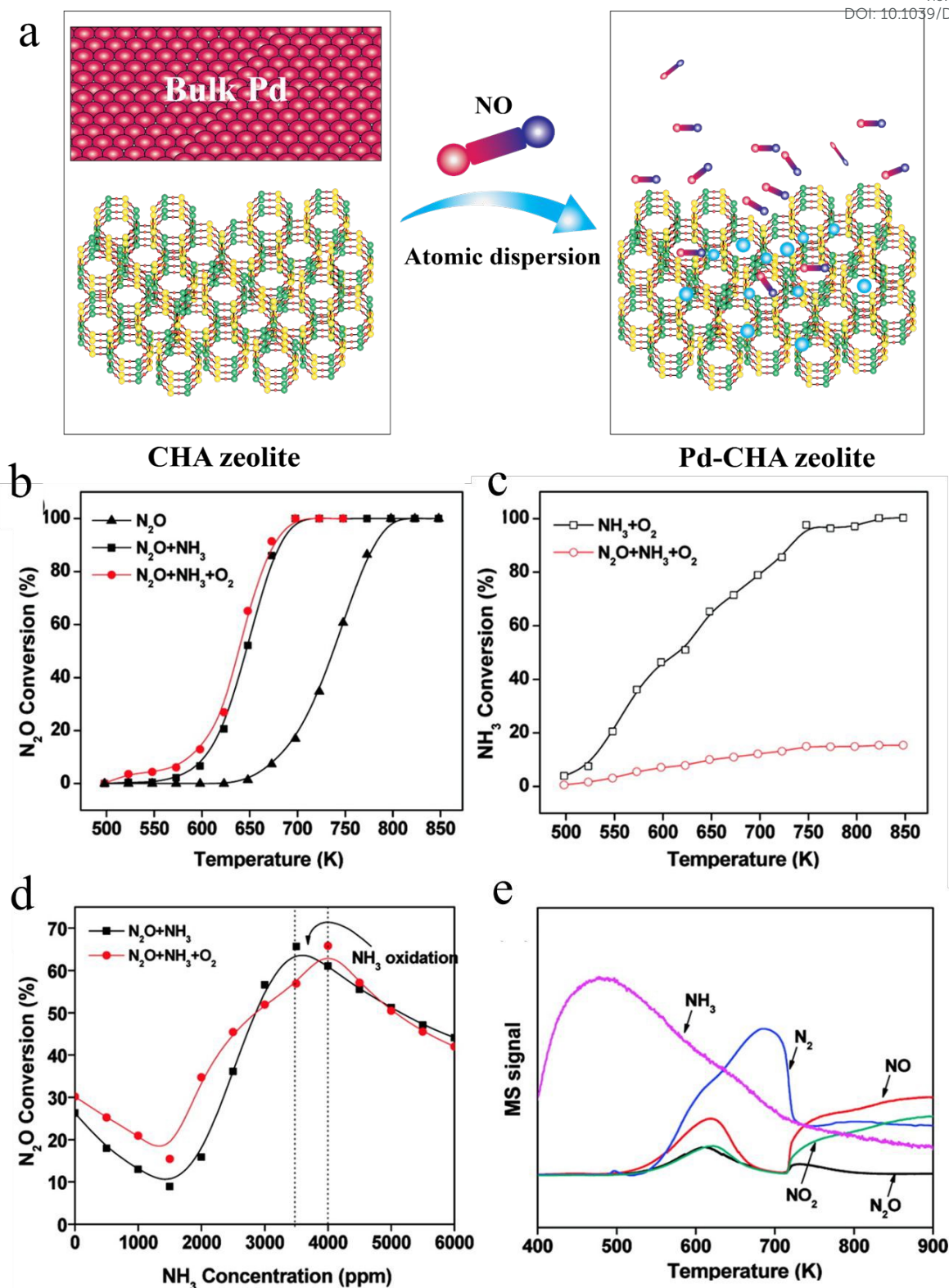
Figure 11a. Transformation of bulk Pd to Pd cations in small-pore CHA zeolites facilitated by NO [170]. Reproduced with permission from American Chemical Society (Copyright © 2021); **b.** Decomposition of N_2O (%) via selective catalytic reduction (SCR) through NH_3 on Fe–MOR catalysts; **c.** decomposition of NH_3 (%) by oxidation of NH_3 with and without N_2O; **d.** decomposition of N_2O (%) via NH_3 as a function of $P(NH_3)$ with and without O_2 and e. TPSR profiles of oxidation of NH_3. (Conditions: 100 mg catalyst, 0 or 4000 ppm NH_3, 0 or 5% O_2, 5000 ppm N_2O, and balance He. GHSV = 30000/h) [174]. Reproduced with permission from American Chemical Society (Copyright © 2012).

5.2.3. Mixed metal oxides in mesoporous silica

After the discovery of well-organized mesoporous molecular sieves, throughout scientific community has developed an igniting curiosity and interest in their catalytic applications. Discovered by Mobil researchers, these mesoporous silica supported catalysts possess a higher surface area as compared to conventional zeolites based catalysts. Owing to their fascinating properties, these materials play an important role to support the other co-catalysts in many catalytic reactions [205].

For example, SBA–15 is a mesoporous silica materials with a fibre-like morphology that is several tons micrometer long. It possesses a 3D porous structure and unique properties [206, 207]. It has various applications including its use as a support material for Rh catalysts in N_2O abatement with Rh being one of the most active metals in N_2O decomposition. Different mesoporous silica supported metal ions, are crucial with regard to their N_2O abatement activity and age resistance but among them Rh/SBA–15–S is found most active and durable. It is well-known because of its superior performance in the presence of O_2 which is typically an inhibiting agent. This is attributed to the large pore size of Rh/SBA–15–S that enhances catalyst's access, diffusion and dispersion. The smaller particle size of Rh in Rh/SBA–15–S results in the higher dispersion of metal on the catalysts surface. It favours the formation of more Rh^+ ions than Rh^0 or Rh^{3+} which, in turn, leads to higher N_2O decomposition activity. Rh/SBA–15–S is found durable, maintaining its performance at temperature of 430 °C. This suggests its suitability as a support material in long-term applications and further research [208]. Similarly, Wei *et al* reported the synthesis of highly dispersed and well-homogenized bimetallic Au–Pd alloy supported on amine-functionalized SBA–15. The catalytic activities, when tested from 150 °C to 600 °C, revealed a decreasing trend with increasing percentage of Au in bimetallic alloy catalysts (Figure 12a). It led to the conclusion that addition of Au negatively affects the activity of Pd catalysts. Though on one hand, Au–Pd alloy facilitates desorption of O_2 molecules; on the other hand, it also affect other elementary steps that change the rate-determining step. Figure 12b depicts energy profiles of N_2O degradation over Pd, Pd_3Au/Pd and $PdAu_3$/Pd catalyst's surface which has been split into three processes i.e. (a) decomposition of N_2O into N_2 and O atoms, (b) diffusion of O atom on the surface of catalyst and (c) recombination of two O atoms to form O_2. Respective mechanisms of degradation are shown through Figure 12c–k [209]. Various other examples of such catalysts have been summarized in the Table 7.

Shortcomings of mesoporous silica-supported metal oxide catalysts: Mesoporous silica-supported metal oxide catalysts often suffer from weak metal-support interactions, leading to metal sintering or leaching under harsh conditions. Their thermal and hydrothermal stability is generally lower than that of crystalline supports like zeolites. Additionally, achieving uniform metal dispersion can be challenging and their catalytic activity may decline over time due to structural degradation or active site deactivation.

Application scenario: Chemical plant emissions: Mixed metal oxides dispersed in mesoporous silica supports provide high surface area, uniform metal dispersion and enhanced redox properties, making them effective for N_2O decomposition in chemical plant emissions. They offer thermal stability and tenability, but advantages include susceptibility to pore blockage, reduced activity under humid or sulphur-rich conditions, and higher synthesis complexity.

5.3. Nanostructured metal-doped materials

Nanostructured metal-doped materials exhibit high surface area, quantum size effects, and unique electronic properties. Doping enhances catalytic activity by modifying charge distribution and creating active sites. Their tunable morphology–nanosheets, nanotubes or cages–improves reactant accessibility. These materials often show superior thermal stability, reactivity, and selectivity making them promising candidates for advanced catalytic applications like N_2O decomposition.

5.3.1. Metal-doped nanotubes, nanosheets and nanocages

Nanotubes, nanosheets and nanocages are elongated, 2D and cage-like structures, respectively, possessing large surface area, crystallinity, high porosity, hollow structure and astonishing electrical and mechanical properties; rendering them novel and excellent choice of catalyst for N_2O decomposition due to a shorter diffusion length and easier mass/heat transport [210, 211]. Recently, metal doped nanotubes (NTs), nanosheets (NSs) and nanocages (NCs)-supported decomposition of N_2O has emerged. Researchers have predicted the roles of metal-confined titania nanotubes [218, 219] carbon nanotubes (CNTs) [220, 221], boron nitride nanotubes, nanosheets [222, 223], and nanocages [224] for N_2O decomposition employing DFT studies.

Metal-doped nanocages are currently among very popular materials that can capture greenhouse gases and protect the environment from their harmful effects. Gao *et al* have successfully doped four Ca atoms in a C_{60} molecule and examined its energy profile for CO_2 capture and N_2O adsorption. In comparison, adsorption of N_2O on pristine C_{60} molecules was very weak as compared with Ca-decorated fullerene C_{60} [225]. Figure 13a represents the doping of Ca atoms in a C_{60} molecule while Figures 13b & c show the adsorption of one and two N_2O molecules on the surface of CaC_{60}, respectively. Metal-doped nancages are currently among very popular material that can capture greenhouse gases and protect the environment from their harmful effects. Gao *et al* have successfully doped four Ca atoms in a C_{60} molecule and examined its energy profile for CO_2 capture and N_2O adsorption. In comparison, adsorption of N_2O on pristine C_{60} molecules was very weak as compared with Ca-decorated fullerene C_{60} [225]. Figure 13a represents the doping of Ca atoms in a C_{60} molecule while Figures 13b & c show the adsorption of one and two N_2O molecules on the surface of CaC_{60}, respectively. Table 8 demonstrates examples of metal doped nanotubes, nanosheets and nanocages utilized for N_2O mitigation studies.
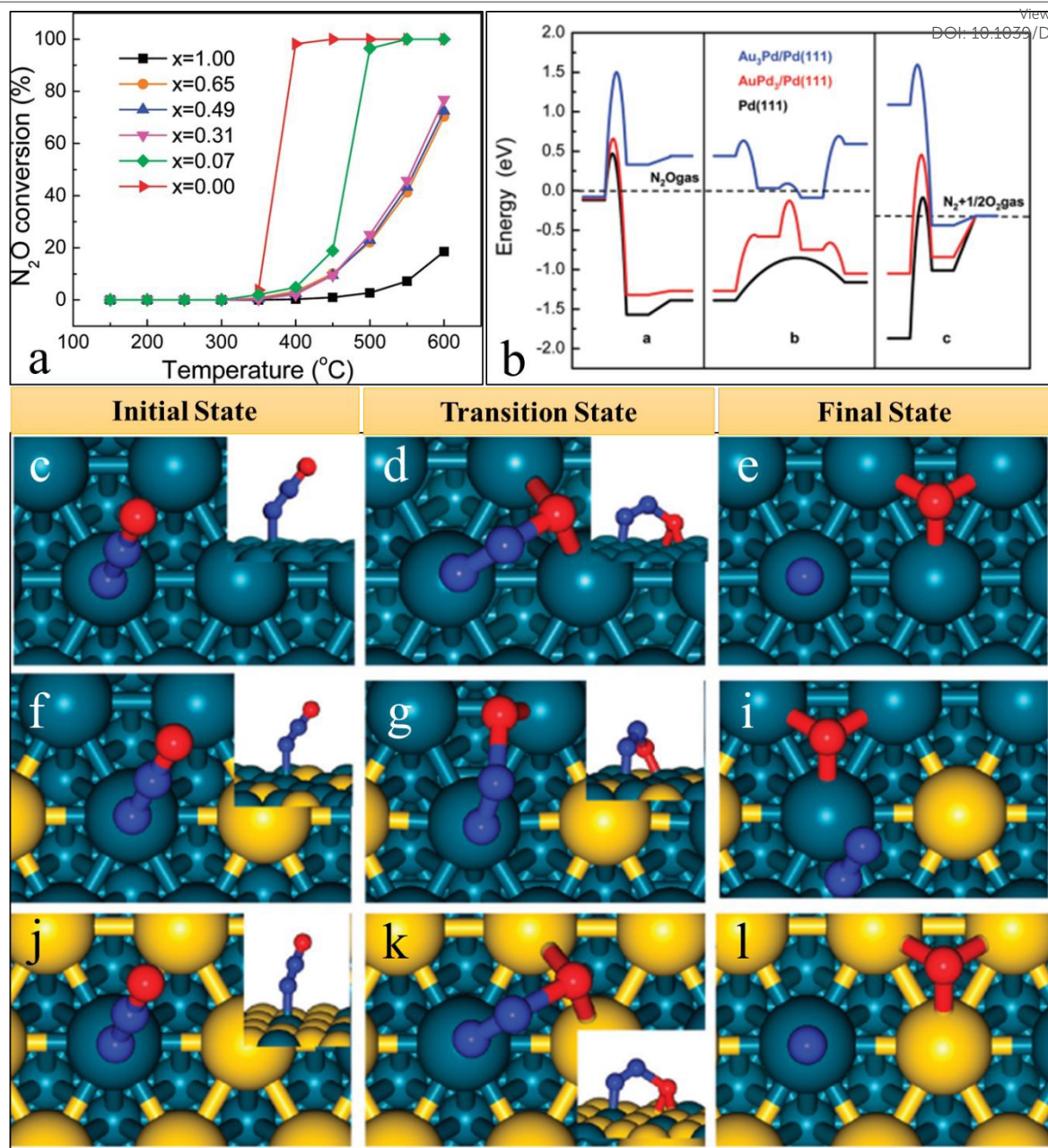
Figure 12a. N_2O conversion (%) as a function of reaction temperature onto Au_xPd_{1-x}/SBA–15 catalysts (where x = atomic ratio of Au to total metal atoms; metal loading = 2 wt%); **b.** Energy profiles for N_2O decomposition on Pd, $AuPd_3$ and Au_3Pd catalysts; **c–k** Mechanism of N_2O degradation into N_2 and O_2 over **(c–e)** Pd, **(f–h)** Pd_3Au/Pd and **(i–k)** $PdAu_3$/Pd catalysts [211]. Reproduced with permission from American Chemical Society (Copyright © 2012).

Table 7. Overview of synthesis methods, reaction conditions and various techniques employed during the course of analysis of mesoporous silica supported metal/metal oxide catalysts for N_2O decomposition.

Catalysts	Method	Reaction atmosphere	Air speed (mL/min)	N_2O Decomposition Temp-range (°C/K)	Techniques used for characterization and activity of catalysts	Ref.
Al_2O_3 + SiO_2	Wet impregnation	N_2	100	300–450 °C	AAS, XRD, TPR–H_2, FTIR, Raman, XPS, SEM, N_2 adsorption	212

Pt, Pd, Rh/Al$_2$O$_3$–SiO$_2$	Hydrothermal	He	100	600–900 °C	XRD, N$_2$ physisorption and FESEM	213
Pt/SiO$_2$	Impregnation	Ar	10	350–600 °C	BET, XRD, ICP	214
Cu–supported on hollow silica–alumina composite	impregnation	N$_2$	50	450–800 K	EDX, UV–Vis–DRS, SEM, TEM	215
Rh@S–1	Hydrothermal	-	-	200–400 °C	STEM, XPS, DRIFTS, TEM	216
NiCoAl–based monolithic catalysts	Wet impregnation	N$_2$	10	300–600 °C	SEM, EDX, BET	217
TiO$_2$@Fe$_2$O$_3$@Al$_2$O$_3$ monolith catalysts	Co-precipitation	-	-	220–420 °C	XRD, XPS	76

Table 8. Overview of synthesis methods, reaction conditions and various techniques employed during the course of analysis of metal doped nanotubes, nanosheets and nanocages for N$_2$O decomposition.

Catalysts	Method	Reaction atmosphere	Air speed (mL/min)	N$_2$O Decomposition Temp-range (°C/K)	Techniques used for characterization and activity of catalysts	Ref.
Metal oxide-confined interweaved TiO$_2$ nanotubes M/TNT (M = Mn, Cu, Ce, Fe, V, Cr and Co)	Wet impregnation	-	-	100–300 °C	BET, HRTEM, XRD, XPS, H$_2$–TPR, NH$_3$–TPD	226
C-doped BN nanotubes (C–BNNTs)	Adsorption	-	-	-	DFT calculations for N$_2$O adsorption and reduction reaction	227
C-doped BN nanosheets	Adsorption	-	-	-	DFT calculations, computational calculations	223
Si-doped C$_3$N (Si–C$_3$N) nanosheets	Adsorption	-	-	-	First-principle (DFT) calculations	228
Fullerene-like boron nitride nanocages (C-doped B$_{12}$N$_{12}$)	Adsorption	-	-	-	DFT calculation of adsorption behaviors of N$_2$O and CO	229
Boron–doped C$_3$N monolayers	Adsorption	-	-	-	DFT	230
A$_{0.5}$Co$_{2.5}$O$_4$ (A = Mg, Ca, Sr, Ba)	Hydrothermal	O$_2$/N$_2$	80	-	DFT	231
Fe–embedded C$_2$N monolayer	-	-	-	-	DFT	232
SACs supported on defective boron nitride nanotubes (BNNT)	-	-	-	-	DFT	233
Potassium promoted Gd$_{0.06}$Co catalysts	Co - Precipitation	Ar	50	150–500 °C	XPS, H$_2$–TPR, O$_2$–TPD, XRD, SEM, TEM	234
Gd to Co$_3$O$_4$	Co-precipitation	N$_2$	350	-	DFT	235
Ni–Co mixed oxides (Ni$_x$Co$_{1-x}$Co$_2$O$_4$)	-	-	-	250–600 °C	SEM, EDX, XRD,	236
CuO–Co$_3$O$_4$	Co-precipitation	NH$_3$/O$_2$/He	100	400–700 °C	XAFS, DRIFTS, DFT, XANES	237
Si (Si–doped haeck–BNNT)	Adsorption	O$_2$	550	-	DFT	238
MgO (100) in SO$_2$ and CO	Adsorption	-	-	-	DFT	239
Rh(0.2)/NC–MnFe	Adsorption	H$_2$	60	100–150 °C	XRD	240
MC$_{23}$ clusters (M = Ru, Mn, V, Rh, and Pd) clusters	-	-	-	-	DFT	241

Materials Advances Accepted Manuscript

Journal Name ARTICLE

Al– or P–doped hexagonal boron nitride nanosheets (h–BNNS)	Adsorption	-	-	-	DFT	242
Si@BN–yne	-	-	-	-	DFT, PDOS	243
Co–doped Fe–Mn@CNTs	Co-precipitation	-	-	170–250 °C	XRD, XPS	244
$Sm_{0.06}Ni$	Adsorption	Ar	50	100–600 °C	SEM, TEM, XRD, XPS, HRTEM	245
$Co_3O_4@CoMn_2O_4$	Hydrothermal	$NH_3/O_2/SO_2/H_2O/Ar$	300	90–270 °C	SEM, TEM, HRTEM, XPS, DRIFTS	246
$M_{13}@Cu_{42}$ (M = Cu, Co, Ni, Zn, Ru, Rh, Pd, Pt) core–shell clusters	Adsorption	-	-	-	DFT	247
$Si@C_{24}N_{24}$	-	-	-	-	DFT	248
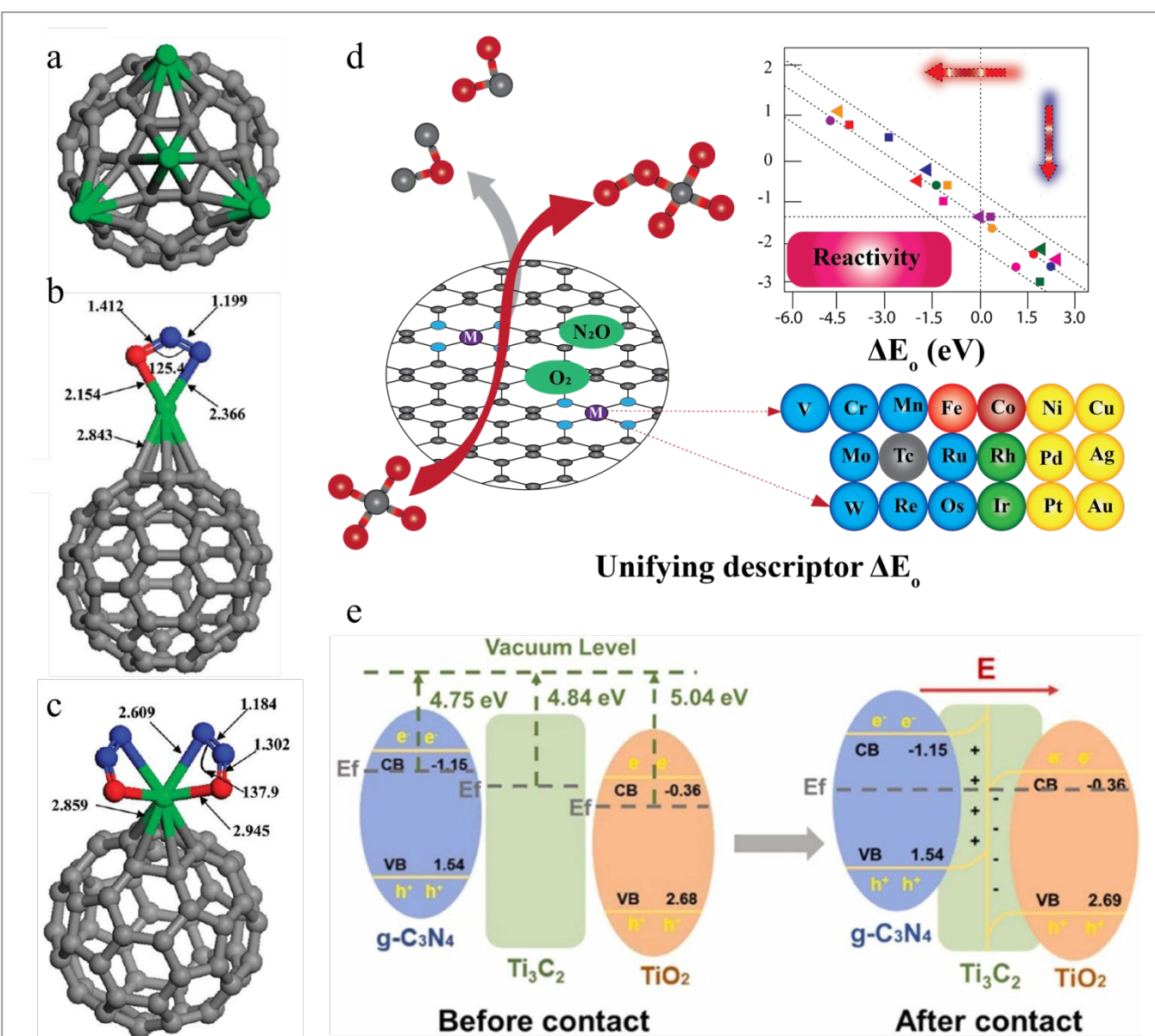
Figure 13a. Four Ca atoms doped C_{60} nanocage; adsorption profiles and corresponding energies of **b.** one and **c.** two N_2O molecules on fullerene (CaC_{60}) [250]. Reproduced with permission from American Chemical Society (Copyright © 2011); **d.** Mechanism of methane to methanol conversion by transition-metal-atom-embedded N-doped graphene($TM–N_4/C$) catalysts with N_2O and O_2 oxidants and a comparison of their reactivity [265]. Reproduced with permission from American Chemical Society (Copyright © 2023). **e.** Energy bands of TiO_2/MXene/g-C_3N_4 displaying energy bending [269]. Reproduced with permission form Elsevier (Copyright © 2023).

Shortcomings of metal doped nanotubes, nanosheets and nanocages: Controlled synthesis of metal-confined nanotubes remains a big issue. They face challenges like structural instability at high temperatures, metal agglomeration and limited long-term durability under reaction conditions. Their synthesis can be complex and costly and scalability remains a barrier. At low temperature zones, these catalysts suffer from serious disadvantages at the industrial level [249].

Application scenario: Power plant emissions: Metal-doped nanostructures offer exceptional surface area, abundant active sites, and tunable electronic properties, making them highly promising for N_2O decomposition in power plant emissions. They provide excellent dispersion of doped metals and improved redox performance. However, challenges include complex synthesis, potential agglomeration, limited large-scale stability, and higher costs compared to conventional catalyst systems.

5.3.2. Metal embedded graphene and graphitic nitrides

Graphene is considered one of the most promising candidates for next generation electronic materials of this decade [250, 251]. Extensive research is carried out on graphene because of its enormous surface-to-volume ratio (i.e. large area) for catalytic reactions. On the other hand, modified graphene sheets display high catalytic performance for N_2O decomposition and several DFT studies have been made on this catalytic behaviour, e.g. transition metal embedded-graphene [252-254], N-doped graphene [255, 256], Si-doped graphene [243, 257], metal oxide-doped graphene [254], and metal-decorated graphene oxides [252, 258]. Among them, transition-metal embedded graphene structures possess good thermal stabilities and stronger bondings between metals and neighbouring C-atoms.

Like graphene, graphitic carbon nitride (g-C_3N_4) is composed of carbon and nitrogen atoms arranged in a 2D, hexagonal lattice. However, in g-C_3N_4, carbon and nitrogen atoms are bonded together in a polymeric, layered structural form. This polymeric arrangement gives it a unique set of properties compared to graphene. However, graphene is a zero-bandgap material while g-C_3N_4 is a semiconductor with moderate bandgap that makes it suitable in electronics and photocatalytic applications especially under visible light. Furthermore, its properties can be tuned by modifying its structure, composition and doping that optimize its performance for specific applications[259-261]. For example, Troppovà *et al* modified its structure by making its nanocomposites by with TiO_2 at different weight ratios. The primary focus of the study was to access the photocatalytic activity of these TiO_2/g-C_3N_4 nanocomposites. They investigated the decomposition of N_2O under UV treatment with wavelength (λ) of 365 nm. The results showed that all the synthesized nanocomposites exhibited higher photocatalytic activity compared to the individual parent materials (g-C_3N_4 and TiO_2) [262]. The enhanced photocatalytic activity of TiO_2/g-C_3N_4 nanocomposites was attributed to the coupling of TiO_2 with g-

C_3N_4. This coupling was found to improve the separation of electron-hole pairs and expand the range of spectral light absorption. Similarly N-doped graphene embedded with single transition metal atoms produces single atom catalysts (SACs) and it can convert CH_4 to CH_3OH with help of N_2O and O_2 oxidants (Figure 13d). The relationship between adsorption energy of oxygen molecules (ΔE_o) and the catalytic reactivity in conversion of methane to methanol can be seen in the inset [263]. Many other examples of use of such catalysts in N_2O abatement are provided in Table 9.

Shortcomings of metal embedded graphene and graphitic oxides/nitrides: Major disadvantages associated with these types of catalysts are their low surface areas and a rapid recombination between photoexcited electrons and holes. However, this problem is overcome by impregnation or doping of a noble metal or co-catalysts into these semiconductor materials [264, 265].

Application scenario: Industrial flue gas treatment: Metal-embedded graphene and graphitic oxides/nitrides provide high conductivity, large surface area, and strong metal-support interactions, enhancing N_2O decomposition in industrial flue gas treatment. They enable efficient electron transfer and dispersion of active sites. However, their disadvantages include high synthesis costs, sensitivity to oxidation at elevated temperatures, and scalability issues for long-term industrial deployment.

5.3.3. MXene based materials

MXene-based catalysts have emerged as promising materials for N_2O decomposition due to their unique 2D structure, high electrical conductivity and tunable surface chemistry. Doping transition metals (e.g. Fe, Co, Cu) into MXenes enhances redox activity and introduces abundant active sites for N_2O adsorption and activation. Their layered morphology facilitates gas diffusion and charge transfer, which are critical for catalytic efficiency. However, stability under high-temperature and oxidative conditions remains a concern. Additionally, scalable synthesis and control over metal dispersion require further development. Despite these challenges, MXene-based catalysts offer a novel platform for designing efficient and selective N_2O abatement systems [266].

As of now, there are very limited experimental studies reporting the use of MXene-based catalysts for N_2O abatement. However, a few studies have been conducted of their N_2O decomposition efficiency by mixing MXenes with other semiconductor photocatalysts. For example, Zhao *et al* prepared triphase heterostructures via self-assembly of titania, MXene and graphitic carbon nitride (TiO_2/MXene/g-C_3N_4) that showed an improved photocatalytic efficiency for NO removal. Z-scheme heterojunctions enhance photocatalysts by preserving strong redox carriers and minimizing recombination of low-activity electrons and holes, as shown in Figure 13e [267]. Other studies associated with photocatalytic decomposition of NO_x via MXene

Journal Name

ARTICLE

coupled with other materials, are listed in Table 10.

Table 9. Overview of synthesis methods, reaction conditions and various techniques employed during the course of analysis of metal embedded graphene, graphitic oxides and nitrides for N_2O decomposition.

Catalysts	Method	Reaction atmosphere	Air speed (mL/min)	N_2O Decomposition Temp-range (°C/K)	Techniques used for characterization and activity of catalysts	Ref.
BC_mN_n-doped graphene sheets	Adsorption	-	-	-	DFT calculations, Computational studies on adsorption configurations, electronic structures, and catalytic activity by quantum chemical calculations	256
Single Si or P atom incorporated N-doped graphene(SiN_4-Gr/PN_4-Gr)	-	-	-	-	Comparative DFT study, computational calculations for adsorption energies and reduction mechanism by first-principle	274
Single Ge or Ga atom-doped graphene	Adsorption	-	-	-	DFT study, computational estimation of adsorption energies and reaction mechanisms	275
ZnO-doped graphene [ZnO(001)@G]	-	-	-	-	DFT calculation for adsorption and activation energies, *ab-initio* model, OAT, ER and LH pathway	276
Al– and Ti–doped graphene (Al–/Ti–graphene)	-	-	-	-	DFT calculations for reaction barriers and thermodynamic parameters	277
M-decorated graphene oxide (M = Mg, Cu or Ag)	Adsorption	-	-	-	DFT computational method	258
Graphitic carbon nitride (g-C_3N_4)	Melamine condensation	N_2	15	400–700 °C	UV–Vis–DRS, PL, FTIR, Raman, SSA, XRD, SEM, TEM	278
TiO_2/g–C_3N_4 photocatalysts	Adsorption	N_2	30	-	XRPD, UV–Vis–DRS, Raman, FTIR, SEM, TEM, BET, PL, XPS, GC–BID	279
TiO_2/g–C_3N_4 photocatalysts	Hydrothermal	O_2	3.5–4.5	-	N_2-physisorption, XRD, UV–Vis–DRS, FTIR, Raman, PL, TEM, XPS	262
g–C_3N_4/WO_3 photocatalysts	Calcination	-	-	-	XRD, XPS, HR–TEM, STEM, N_2–adsorption, UV–Vis–DRS, PL, EDS	280
g–C_3N_4/ZnO nanocomposite photocatalysts	Co-precipitation	-	-	-	XRD, UV–Vis, FTIR, Raman Spectroscopy, TEM and AAS	281
g–C_3N_4/$BiVO_4$ composite photocatalysts	Sol-gel	N_2	500	-	XRD, N_2–physisorption, UV–Vis–DRS, PL, FTIR, XPS, TEM	282
$BiVO_4$/g–C_3N_4 (1:1) composite photocatalysts	Adsorption	-	-	-	XPS, UV–Vis–DRS, PL, FTIR, Raman, BET, TEM	283
g-C_3N_4 and $BiOIO_3$	Hydrothermal	-	-	300–800 °C	FTIR, XRPD, XPS, HRTEM, DRS, TEM	284
SiN_4G	-	-	-	-	DFT	285
Cu-Embedded Graphene	Adsorption	-	-	-	DFT	252
Si@Graphene	Adsorption		-	100–350 °C	DFT	257
Au/C_2N and Cu/C_2N	Adsorption	-	-	-	DFT	286
Si–doped C_3N (Si–C_3N) nanosheets	Co-adsorption	-	-	-	DFT	287
Co_3O_4/g–CN	Wet impregnation	N_2	5	100–700 °C	XRD, HR–TEM, N_2–physisorption, Raman,	288

Materials Advances Accepted Manuscript

					FT–IR, XPS, H$_2$–TPR, CO$_2$–TPD, EC

5.4. Porous MOFs and MOF-derived catalysts

MOFs act as porous solid material catalysts possessing coordinatively unsaturated sites (CUS) for gas adsorption, separation and catalysis [268]. Their well-defined composition, hollow structures, small particle size, and exposed surface, impart considerable efficiency and stability to these catalysts. MOFs are also utilized as precursors for the synthesis of metal oxides that can prevent the nanoparticle's clustering during the calcination [269].

Metal-organic frameworks are composed of metal atoms or metal oxides clusters coordinated to organic linkers. This arrangement creates a highly ordered, porous network with a large surface area. The choice of metal and linkers can be tailored to achieve specific applications. MOFs are well-known for their structural flexibility, meaning that their frameworks can be tuned or modified to suit particular needs. This flexibility allows for the design of customized surface and porous structures. Coordinative unsaturated metal sites are of particular interest as these sites have metal atoms with unoccupied coordination, making them highly reactive. CUS can be crucial in gas adsorption and separation processes as well as catalytic reactions that's why MOFs are excellent candidates for gas adsorption and separation due to their high surface area and tunable porosity. The tunable nature of MOFs generate catalytic sites with precise geometries, enhancing catalytic efficiency and selectivity [270, 271]. For example, nanoscale MOFs may exhibit different properties compared to their bulk counterparts, making them suitable for their specific dynamic applications [272, 273].

Despite of the huge number of reports on gas sorption, the N$_2$O abatement studies by MOFs are still scarce. The common route of N$_2$O abatement is through catalytic decomposition, but adsorptive removal of N$_2$O by MOFs had also been reported in cases when catalytic decomposition is not economically feasible due to very low N$_2$O concentration [147]. In the some studies, MOFs also offer an important mean for dissociative adsorption of N$_2$O [289-293], as displayed in Figure 14.

Vogiatzis *et al* conducted a computational study on high-spin Fe(IV)–OXO complexes that have well-known activating effects on the strong C−H bonds [294]. Although it is difficult to stabilize a high-spin electronic configuration for homogenous catalysis in molecular species, results suggested that it is attainable in MOFs-based catalysts, e.g. Fe$_2$(dobdc) and its Mg-substituted analogues. By the use of a screening approach, different frameworks were identified that could form Fe(IV)–OXO complexes on N$_2$O adsorption. It was concluded from the study that among different materials, Fe–BTT selectively oxidizes C$_2$H$_8$ to C$_2$H$_5$OH by N$_2$O adsorption. The follow-up spectroscopic techniques suggested that the observed reactivity was attributed to the existing defect sites [294]. Further examples from the recent studies have been given in Table 11.

Shortcomings of MOFs and MOF-derived catalysts: MOFs and MOF-derived catalysts face challenges such as limited thermal stability, structural degradation under reaction conditions, and low conductivity, which can hinder electron transfer during N$_2$O decomposition. Additionally, their synthesis cab ne complex and costly and active site accessibility may be restricted, affecting overall catalytic efficiency.

Application scenario: Waste gas purification: MOFs and MOF-derived catalysts offer ultra-high surface area, tunable porosity, and flexible metal-ligand coordination, making them highly effective for N$_2$O decomposition in waste gas purification. Their derived metal oxides or carbons show strong redox activity and stability. However, drawbacks include complex synthesis, limited hydrothermal and thermal stability and challenges in scaling up for industrial applications.

5.5. Emerging or novel materials

Antenna-reactor catalysts and quantum dots-based catalysts exhibit unique light-harvesting and charge separation abilities, crucial for N$_2$O decomposition. Further details are provided in the coming sections.

5.5.1. Antenna-reactor catalysts

Very recently, the concept of "Antenna–Reactor" plasmonic photocatalysts is introduced and it is rapidly gaining interest in the field of catalysis. In a few studies done till now, N$_2$O decomposition was selected as a model reaction [138, 303]. The use of antenna-reactor photocatalysts holds special significance in controlling the rate and products of various chemical reactions. Being poor absorbers of light, many traditional catalysts lack the ability to catalyze efficiently because of the restricted surface chemistry. By combining a catalytic nanoparticle with a plasmonic nanoantenna in a single complex, the light-harvesting properties of plasmonic nanoparticles can be fine-tuned to increase light absorption [304]. Table 12 summarizes few examples of these such catalysts.

5.5.2. Quantum dots

Quantum dots (QDs) can play a significant role in N$_2$O decomposition due to their tunable bandgaps, high surface-to-volume ratios, and excellent light absorption properties. These features enable efficient electron-hole pair generation and separation under visible light, promoting redox reactions. QDs can be engineered to provide active sites for N$_2$O adsorption and activation, potentially lowering the activation energy and enhancing catalytic efficiency under mild, sustainable reaction conditions [305]. Currently, there are no experimental studies specifically reporting the use of QDs for N$_2$O decomposition. However, theoretical investigations have predicted their potential.

Table 10. Overview of synthesis methods, reaction conditions and various techniques employed during the course of analysis of MXene based catalysts for N_2O decomposition.

Catalysts	Method	Reaction atmosphere	Air speed (mL/min)	N_2O Decomposition Temp-range (°C/K)	Techniques used for characterization and activity of catalysts	Ref.
UO_2@MXnene (e.g. Ti_2CO_2, V_2CO_2, Cr_2CO_2, Zr_2CO_2, Nb_2CO_2, Mo_2CO_2)	-	-	-	-	*ab initio* calculations	295
Y-doped Ti_2CO_2 (MXene) monolayer	-	-	-	-	DFT and *ab initio* calculations	296
P@Cr_2CO_2 and P@$MoCO_2$	-	-	-	-	DFT	297
g-C_3N_4/TiO_2/Ti_3C_2 MXene	Air oxidation and ultrasonic processing	O_2	3000	-	XRD, SEM, TEM, HRTEM, EDS, XPS, PL, BET, EPR	298
TiO_2–N–$Ti_3C_2T_x$	Co-precipitation	-	-	-	TEM, SEM, FTIR, Raman, XPS, PL, EPR	299
(Ti,C)-BiOBr/$Ti_3C_2T_x$	Solvothermal	N_2	200	-	XRD, FESEM, STEM, DRS, XPS, BET, Raman	300
Ti_3C_2-OH with TiO_2	Co-precipitation	N_2	-	-	SEM, TEM, XRD, XPS	301
Cu/$Ti_3C_2O_2$-V_0 and Ni/$Ti_3C_2O_2$-Ti_1	-	-	-	-	DFT	302

Table 11. Overview of synthesis methods, reaction conditions and various techniques employed during the course of analysis of MOFs and MOF-derived catalysts for N_2O decomposition.

Catalysts	Method	Reaction atmosphere	Air speed (mL/min)	N_2O Decomposition Temp-range (°C/K)	Techniques used for characterization and activity of catalysts	Ref.
$M_3(BTC)_2$ MOF [M = Cr, Fe, Co, Ni, Cu and Zn]	Wet impregnation	-	-	-	DFT calculations with M06–L functional, EXAFS, computational screening	306
MOF-derived Ni/CeO_2 HPOC	Wet impregnation	Ar	10	250–500 °C	SEM, TEM, N_2–adsorption, EDS, XRD, H_2–TPR, Raman, XPS, ICP–MS, GC–TCD	290
Fe-supported MOF Zr–NU–1000	Wet impregnation	-	-	-	DFT and CASPT2 calculations with M06–L functional	307
MnO_2 decorated Ru–MOF (Ru–NH_2–UiO–66/MnO_2)	Hydrothermal	-	-	Not clear	XRD, XPS, BET, SEM, TEM, N_2O–TPD, MS, EXAFS, IC, DFT	308
MFU–4*l* MOFs (MFU–4*l*, Cu^I–MFU–4*l* and Li–MFU–4*l*) ($BTDD^{2-}$ ligands and $[Zn_5Cl_4]^{6+}$ building units)	Wet impregnation	N_2	3	Not clear	DFT calculations, PXRD, FTIR, TGA, ICP–OES, BET	309
Fe(II)(Me_3TACN)(S_2S iMe_2)	Hydrothermal	-	-	100–135 °C	UV–vis, resonance Raman, EPR, Mössbauer, XAS, DFT	310
ZIF–67 derived Co/CoO_x@C	Hydrothermal	N_2	30	305–650 °C	TPD, DRIFTS	311
Mn@$Cu_3(BTC)_2$	Ion exchange	-	-	230–260 °C	SEM, TEM, XRD, XPS, FESEM, ZEISS-ΣIGMA HD, BET	312

Materials Advances Accepted Manuscript

Table 12. Overview of synthesis methods, reaction conditions and various techniques employed during the course of analysis of antenna-reactor catalysts for N_2O decomposition

Catalysts	Method	Reaction atmosphere	Air speed (mL/min)	N_2O Decomposition Temp-range (°C/К)	Techniques used for characterization and activity of catalysts	Ref.
Al–Ir antenna–reactor photocatalysts	Ion exchange	-	-	250–350 °C	HAADF–STEM, MS, XPS and UV–Vis–NIR	138
Antenna–reactor plasmonic photocatalysts (Pd decorated Al NCs, Al@Cu_2O and Cu–Ru surface alloy@Cu)	Co-precipitation	-	-	-	XPS, ICP–MS, UV–Vis–DRS, TEM, HAADF,GC–MS, HR–TEM	303

6. Performance-based summary of N_2O decomposition catalysts

Performance-based comparisons are critical for identifying optimal catalysts and guiding their future research directions. Table 13 provides a comparative summary of the benchmark performance metrics for different classes of catalysts used in N_2O decomposition, based on catalytic activity, temperature range, hydrothermal stability, and resistance to inhibitors. This provides a clear performance-based comparison of N_2O decomposition catalysts.

7. Mechanisms of N_2O decomposition

There are five primary mechanisms of N_2O decomposition in context of fundamental steps and catalysts surface interactions. These mechanisms are key to understanding how various catalysts function in breaking down N_2O into harmless components (Figure 15).

7.1. Direct thermal decomposition

$$N_2O \rightarrow N_2 + \tfrac{1}{2} O_2$$
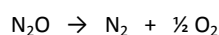
Direct thermal decomposition of nitrous oxide occurs at temperatures above 800 °C in the absence of catalysts. Although the reaction is thermodynamically favourable, the extreme energy demand makes this route impractical for most industrial applications. However, in certain specialized high-concentration processes such as semiconductor manufacturing, direct pyrolysis of N_2O has been investigated under nitrogen-rich atmospheres at temperatures approaching 1000 °C. These studies demonstrate that while N_2O can indeed be decomposed at such conditions, the process requires significant thermal input and careful gas-phase control, which limits its scalability for broader emission abatement. Nonetheless, this pathway remains relevant in niche applications where high-purity nitrogen or oxygen streams are simultaneously desired [313].

7.2. Surface-catalysed decomposition

Most practical catalysts (e.g. Fe, CO and Cu-based) accelerate this reaction by activating N_2O on their surfaces. It requires active
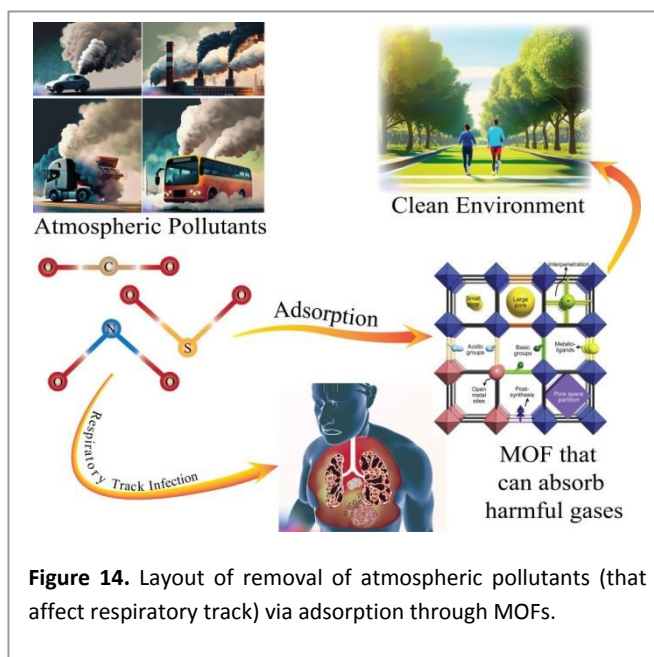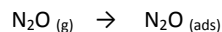

Figure 14. Layout of removal of atmospheric pollutants (that affect respiratory track) via adsorption through MOFs.

oxygen-vacancy sites. Catalysts can be used to lower the activation energy for N–O bond scission. Overall, it is summarized in three steps [314, 315];
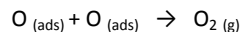
1. Adsorption

$N_2O_{(g)} \rightarrow N_2O_{(ads)}$

2. N–O bond cleavage

$N_2O \rightarrow N_{2(g)} + O_{(ads)}$

3. Recombination of surface oxygen

$O_{(ads)} + O_{(ads)} \rightarrow O_{2(g)}$

7.3. Redox mechanism (Mars-van Krevelen type)

It is commonly observed in transition metal oxide catalysts. Here, catalysts surface is first reduced and then deoxidized, enabling a catalytic cycle [316, 317].

1. In first step, N_2O reacts with a lattice oxygen.

$N_2O + [M]–O \rightarrow N_2 + [M]–O–O$
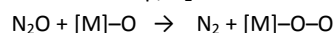
2. Oxygen vacancy is replenished by O_2 from gas phase.

$[M] + \frac{1}{2} O_2 \rightarrow [M]–O$
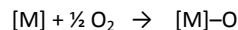
7.4. Single atom or atomically dispersed catalysis

This type of catalysis is common in Fe-ZSM-5, Fe-SSZ-13 and Cu-CHA materials. During it, first N_2O coordinates to a single metal centre. Then N–O bond is cleaved through electron transfer from the metal. Oxygen binds to the metal site or adjacent framework oxygen. It shows high site selectivity and stability, especially in the presence of steam or O_2.

7.5. Photocatalytic decomposition

It involves photon-excitation of catalysts like TiO_2, g-C_3N_4 or MXene hybrids. In this case, light generates electron-hole pairs in the photocatalysts. Electrons are responsible for the reduction of N_2O to N_2. Holes may oxidized adsorbed species or water to maintain charge neutrality. This mechanism is still under development particularly for low-temperature N_2O removal.

8. N₂O activation mechanisms

N_2O activation mechanisms follow different pathways, three of which are most common, including dual-pathway mechanism, radical-initiated oxidative decomposition and electron-assisted surface decomposition. Representative reactions belonging to each category are indicated in this section.

8.1. Dual-pathway mechanism

It corresponds to the classical surface-mediated activation of H_2O on catalysts active sites (*), described as follows;

$N_2O + * \rightarrow N_2 + *O^-$

$2*O^- \rightarrow O_2 + 2* \qquad N_2O + *O^- \rightarrow N_2 + O_2 + *$
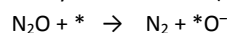
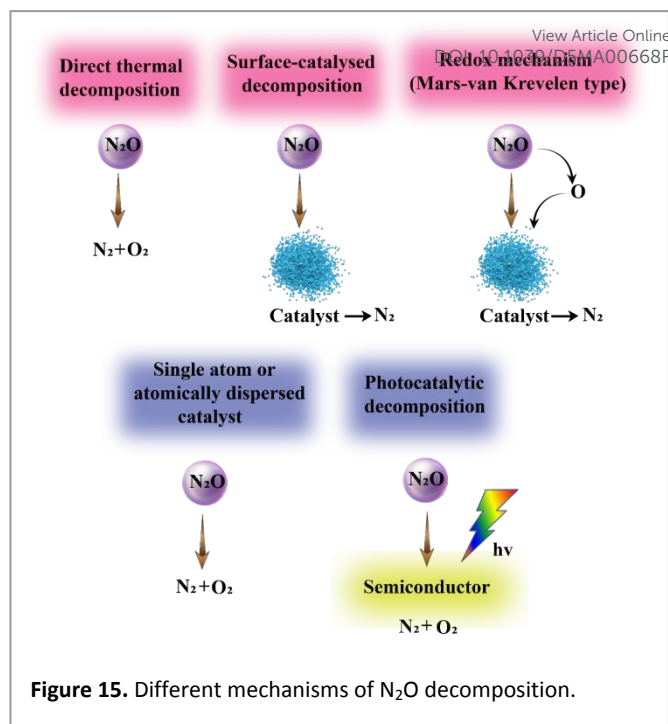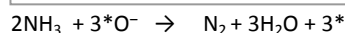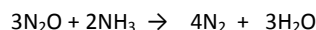When NH_3 is present (NH_3-assisted SCR), surface O_2 can be removed as


Figure 15. Different mechanisms of N_2O decomposition.

$2NH_3 + 3*O^- \rightarrow N_2 + 3H_2O + 3*$

Interaction of NH_3 with N_2O is given as

$3N_2O + 2NH_3 \rightarrow 4N_2 + 3H_2O$

Fe–MOR catalyst was employed for the systematic investigation of N_2O reduction reaction mechanism by NH_3, through which the roles of different oxygen species were examined [318] (Figure 16a).
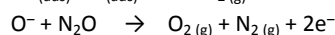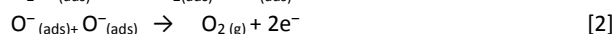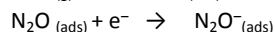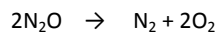
8.2. Radical-mediated oxidation of N₂O

In this case, N_2O activation occurs by the following main reaction routes (Figure 16b);

$N_2O \rightarrow NO + N$

$NO + O \rightarrow NO_2$

$NO + OH \rightarrow HNO_2$

$NO_2 + OH \rightarrow HNO_3$
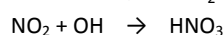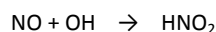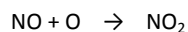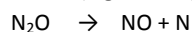
8.3. Electron-mediated reduction of N₂O

The solid solution system is fairly active toward the decomposition reaction of N_2O in the temperature range 300–450 °C. Winter proposed the mechanism N_2O decomposition reaction involving the following steps [319], (Figure 16c).

$2N_2O \rightarrow N_2 + 2O_2$

$N_2O_{(g)} \rightarrow N_2O_{(ads)}$ [1]

$N_2O_{(ads)} + e^- \rightarrow N_2O^-_{(ads)}$

$N_2O^-_{(ads)} \rightarrow N_{2(ads)} + O^-_{(ads)}$

$O^-_{(ads)} + O^-_{(ads)} \rightarrow O_{2(g)} + 2e^-$ [2]

$O^- + N_2O \rightarrow O_{2(g)} + N_{2(g)} + 2e^-$

In governing the reaction rate, N_2O adsorption [step 1] and oxygen (O^-_{ads}) desorption as O_2 [step 2] are the key steps. Using the rate equations given below, the kinetic parameters of N_2O decomposition have been derived [320].

$$\ln\left(\frac{a}{a-x}\right) = k_1 t$$

$$\left(\tfrac{1}{2}a\right)ln\left(\frac{a^{1/2}+x^{1/2}}{a^{1/2}+x^{1/2}}\right)-(2x)^{1/2}=k_2t$$

$$ln\left(\frac{a}{a-x}\right)-b\left[\left(\tfrac{1}{2}a\right)ln\left(\frac{a^{1/2}+x^{1/2}}{a^{1/2}+x^{1/2}}\right)-(2x)^{1/2}\right]=k_t3 \qquad [3]$$

Table 13. Comparative benchmark performance of N$_2$O decomposition catalysts

Catalyst class	Typical active sites	*T$_{50}$ (°C)	Hydrothermal stability	**Resistance to H$_2$O/O$_2$	Remarks
Metal oxides	CuO, Co$_3$O$_4$, MnO$_2$	300–500	Moderate	Low moderate	Inexpensive; deactivated by moisture
Spinel oxides	CoFe$_2$O$_4$, MnFe$_2$O$_4$	300–450	High	Moderate	Good stability; better than simple oxides
Hydroxyapatites	Ca$_{10}$(PO$_4$)$_6$(OH)$_2$ doped with Fe, Cu	>450	Moderate	Poor	High thermal stability; lower activity
Mixed metal oxides	Cu–Mn, Fe–Al oxides	250–400	Moderate	Low – Moderate	Synergistic effects; still limited by deactivation
Hydrotalcites	Mg–Al–Fe–Cu layered structures	300–500	Moderate	Moderate	Tunable; activity depends on calcination
Zeolites	Fe, Co, Cu in ZSM-5, SSZ-13	200–400	High	High	Fe-SSZ-13 shows best performance under wet/oxidizing conditions
Mixed metal oxides in mesoporous silica	Fe/Cu in SBA-15, MCM-41	250–450	Moderate – High	Moderate	Good dispersion and surface area
Metal-doped nanotubes/ nanosheets	Fe, Co, Cu on CNTs, g-C$_3$N$_4$, BN	300–500	Moderate	Low – Moderate	High surface are; expensive synthesis
Graphene and graphitic nitrides	Single atoms or clusters (Fe, Co)	250–450	Low – Moderate	Low – Moderate	Tunable electronic structure; prone to sintering
MXene-based materials	Ti$_3$C$_2$, Mo$_2$TiC$_2$ doped with metals	250–400	Moderate	Moderate	Emerging materials with potential for hybrid photocatalysis
MOFs and MOF-derived catalysts	Fe-MIL-100, ZIF-8-derived oxides	300–500	Low – Moderate	Poor	High porosity; often thermally unstable
Antenna-reactor catalysts	Dual-site systems (e.g. Ce, Fe)	200–350	Moderate	Moderate – High	Emerging concept; synergistic enhancement
Quantum dots-based catalysts	CdS, Fe$_3$O$_4$ QDs supported on hosts	<300 (predicted)	Unknown	Unknown	Theoretical potential; lacks direct experimental validation

* T$_{50}$ (°C): Temperature at which 50% N$_2$O conversion is achieved.

**Resistance to H$_2$O/O$_2$: Resistance to inhibition by water vapour or oxygen.

Where, α = P° N$_2$O (i.e. initial pressure of N$_2$O), x = P^t N$_2$O (which represents the pressure of N$_2$O at time 't'), and x/2 = P^{t}O$_2$ (i.e. pressure of oxygen released at any time 't').

Journal Name

ARTICLE

This rate equation corresponds to non-inhibitory effect caused by O_2. The rate equation [3] corresponds to strong inhibition by O_2 and represents weak inhibition on the decomposition kinetics by O_2 [321].

9. Conclusions and future perspectives

In this review we have summarized various categories of N_2O decomposing catalysts. Starting with the well-known category of TMI exchanged-zeolites, we then have gone through other different classes, including hydrotalcites, spinel oxides, mixed metal oxides, mesoporous silica supported metal oxides and pure metal oxides, and finally the more recent categories of catalysts such as the metal-doped nanotubes, nanosheets and nanocages, graphene and graphitic oxides/nitrides, MOFs and MOF-derived catalysts for adsorptive reduction of N_2O. Nitrous oxide (N_2O) is a potent greenhouse gas and a major contributor to stratospheric ozone depletion. Its anthropogenic and natural emissions through biological processes such as nitrification, denitrification and nitrifier denitrificaion along with abiotic pathways and industrial activities, demand urgent and effective mitigation strategies. Catalytic decomposition of N_2O into benign products (N_2 and O_2) stands out as a promising solution owing to its direct applicability in emission abatement technologies and potential integration into existing industrial setups.

This review comprehensively categorizes N_2O decomposition catalysts based on their mechanisms, composition and material structure, providing a unified understanding of their functionality and efficiency. Mechanistically, the catalysts are classified into those following direct catalytic decomposition (DCD), selective catalytic reduction (SCR) and other redox or surface-catalysed processes. Composition-wise, both precious metal-based catalysts (e.g. Rh, Pt, Pd) and non-precious alternatives (e.g. Fe, Co, Cu-based materials) have been investigated with emphasis on cost, stability and activity trade-offs. The type of support materials – ranging from metal oxides, and spinels to mesoporous and layered structures – plays a vital role in modulating dispersion, redox behaviour and oxygen vacancy dynamics.

Importantly, this review offers a progress-based classification, moving from classical oxide-based catalysts to novel nanostructured materials and framework materials such as MOFs and MOF-derived catalysts, which have shown significant promise due to their high surface areas, tunbale porosity and ability to accommodate multiple active sites. Emerging materials like antenna-reactor systems and quantum dots illustrate the frontier of N_2O decomposition research, hinting at the exciting potential of photonic and nanoscale control over activation energies.

Mechanistic pathways such as surface-catalysed decomposition, Mars-van Krevelen mechanisms, and single-atom catalysis reveal the
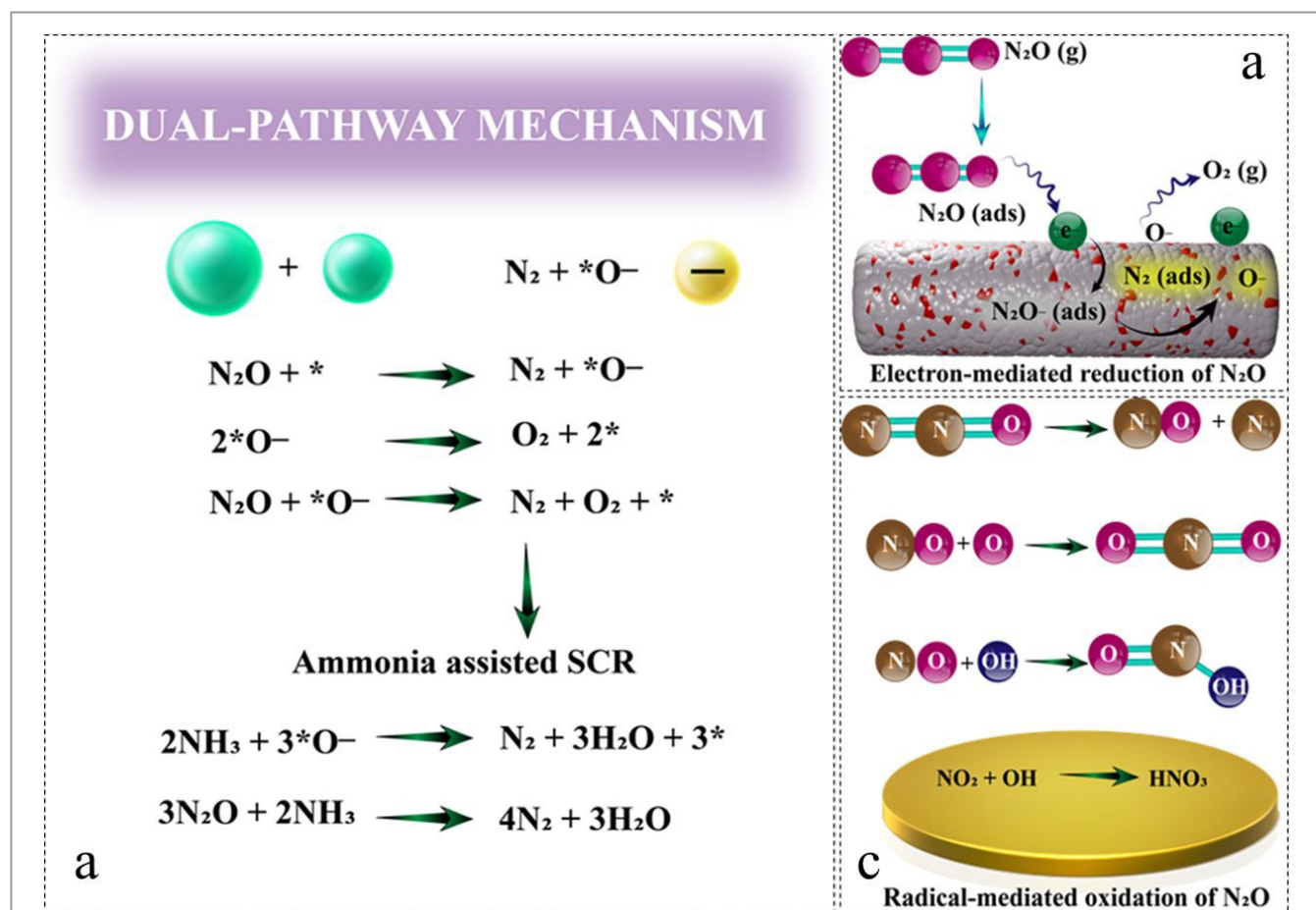

Figure 16. Different mechanisms of N_2O decomposition.

intricate nature of N_2O activation, where lattice oxygen, metal oxidation states and coordination environments dictate the reaction rate and selectivity. Novel mechanisms including photocatalytic and electron/radical-mediated pathways further expand the toolkit available for N_2O conversion, particularly under mild conditions or light-driven environments.

Looking ahead, several key future perspectives emerge. Firstly, the rational design of catalysts with high activity at low temperatures coupled with selectivity and durability under industrial gas compositions, remains an urgent priority. The integration of computational modelling and machine learning can accelerate the discovery of optimal catalysts compositions and structures. Secondly, a shift towards earth-abundant, non-toxic elements is essential to scale these technologies sustainably. Single-atom catalysts and dual-function catalysts that combine decomposition with selective oxidation or reduction reactions open new frontiers in multifunctional reactor design.

Moreover, in-situ and operando characterization techniques should be leveraged to elucidate real-time reaction mechanisms, bridging the gap between theoretical models and actual catalysts performance. Finally, interdisciplinary collaboration between catalysis, material science, environmental engineering and process design is essential to translate laboratory successes into commercially viable solutions.

In summary, catalytic N_2O decomposition is a vibrant and evolving field. Continued research on catalyst development, mechanistic understanding and scalable application will be pivotal in mitigating N_2O emissions and achieving global climate and sustainability goals.

Acknowledgments

References

1.   F. Charlson, S. Ali, T. Benmarhnia, M. Pearl, A. Massazza, J. Augustinavicius and J. G. Scott, *International journal of environmental research and public health*, 2021, **18**, 4486.
2.   S. Sinhababu, Y. Lakliang and N. P. Mankad, *Dalton Transactions*, 2022, **51**, 6129-6147.
3.   K. Hayashi and N. Itsubo, *The International Journal of Life Cycle Assessment*, 2023, 1-13.
4.   N. J. Bassous, A. C. Rodriguez, C. I. L. Leal, H. Y. Jung, C. K. Lee, S. Joo, S. Kim, C. Yun, M. G. Hahm and M. H. Ahn, *Advanced Sensor Research*, 2023, 2300094.
5.   R. Feng and X. Fang, *Environmental Science & Technology*, 2022, **56**, 5299-5301.
6.   S. He, Y. Han and X. Qin, *Journal of Environmental Sciences*, 2024.
7.   B. K. Sovacool, S. Griffiths, J. Kim and M. Bazilian, *Renewable and Sustainable Energy Reviews*, 2021, **141**, 110759.
8.   X. Zhu, M. Burger, T. A. Doane and W. R. Horwath, *Proceedings of the National Academy of Sciences*, 2013, **110**, 6328-6333.
9.   N. Wrage, G. L. Velthof, M. L. Van Beusichem and O. Oenema, *Soil biology and Biochemistry*, 2001, **33**, 1723-1732.
10. T. C. Robinson, D. E. Latta, L. Notini, K. E. Schilling and M. M. Scherer, *Environmental Science: Processes & Impacts*, 2021, **23**, 1531-1541.
11. Y. Zhang, G. Cao and X. Yang, *Energy & Fuels*, 2021, **35**, 6443-6464.
12. Y. Liu, F. Gao, H. Yi, C. Yang, R. Zhang, Y. Zhou and X. Tang, *Environmental Science and Pollution Research*, 2021, **28**, 2549-2571.
13. H. Chen, L. Zeng, D. Wang, Y. Zhou and X. Yang, *Water Research*, 2020, **184**, 116168.
14. M. Galle, D. Agar and O. Watzenberger, *Chemical Engineering Science*, 2001, **56**, 1587-1595.
15. A. E. Hughes, N. Haque, S. A. Northey and S. Giddey, *Resources*, 2021, **10**, 93.
16. Q. Zhang, S. Gao and J. Yu, *Chemical reviews*, 2022, **123**, 6039-6106.
17. N. Richards, J. H. Carter, E. Nowicka, L. A. Parker, S. Pattisson, Q. He, N. F. Dummer, S. Golunski and G. J. Hutchings, *Applied Catalysis B: Environmental*, 2020, **264**, 118501.
18. S. Hinokuma, T. Iwasa, Y. Kon, T. Taketsugu and K. Sato, *Catalysis Communications*, 2021, **149**, 106208.
19. S. Hinokuma, T. Iwasa, Y. Kon, T. Taketsugu and K. Sato, *Scientific Reports*, 2020, **10**, 21605.
20. M. Miao, M. Zhang, H. Kong, T. Zhou, X. Yang and H. Yang, *Energies*, 2021, **14**, 6148.
21. Y. Yin, R. Xiao, L. Qiu, C. Wang and H. Chang, *Fuel*, 2024, **366**, 131303.
22. Y. Li, S. Yang, H. Peng, W. Liu, Y. Mi, Z. Wang, C. Tang, D. Wu and T. An, *Journal of catalysis*, 2021, **395**, 195-209.
23. R. Li, Y. Li and Z. Liu, *Fuel*, 2024, **355**, 129405.
24. N. Richards, J. H. Carter, L. A. Parker, S. Pattisson, D. G. Hewes, D. J. Morgan, T. E. Davies, N. F. Dummer, S. Golunski and G. J. Hutchings, *ACS Catalysis*, 2020, **10**, 5430-5442.
25. A. Szymaszek-Wawryca, P. Summa, D. Duraczyńska, U. Díaz and M. Motak, *Materials*, 2022, **15**, 7884.
26. F. Lin, T. Andana, Y. Wu, J. Szanyi, Y. Wang and F. Gao, *Journal of Catalysis*, 2021, **401**, 70-80.
27. F. Saleem, M. Z. Abid, K. Rafiq, A. Rauf, K. Ahmad, S. Iqbal, R. Jin and E. Hussain, *International Journal of Hydrogen Energy*, 2023, DOI: https://doi.org/10.1016/j.ijhydene.2023.05.048.
28. N. Wajid, K. Rafiq, M. Z. Abid, A. Ilyas, T. Najam, A. Rauf and E. Hussain, *Materials Chemistry and Physics*, 2023, **306**, 128062.
29. M. Sabir, K. Rafiq, M. Z. Abid, U. Quyyum, S. S. A. Shah, M. Faizan, A. Rauf, S. Iqbal and E. Hussain, *Fuel*, 2023, **353**, 129196.
30. T. Gaidei, A. Kokorin, N. Pillet, M. Srukova, E. Khaustova, G. Shmurak and N. Yaroshenko, *Russian Journal of Physical Chemistry A*, 2007, **81**, 895-900.
31. L. Han, S. Cai, M. Gao, J.-y. Hasegawa, P. Wang, J. Zhang, L. Shi and D. Zhang, *Chemical Reviews*, 2019, **119**, 10916-10976.

Please do not adjust margins

Materials Advances

Materials Advances Accepted Manuscript

Journal Name

ARTICLE

32. D. Shun, D. H. Bae, J. Y. Paek and Y. S. Park, *Korean Journal of Chemical Engineering*, 2004, **21**, 890-894.

33. A. Ilyas, K. Rafiq, M. Z. Abid, A. Rauf and E. Hussain, *RSC Advances*, 2023, **13**, 2379-2391.

34. M. Z. Abid, A. Ilyas, K. Rafiq, A. Rauf, M. A. Nadeem, A. Waseem and E. Hussain, *Environmental Science: Water Research & Technology*, 2023, **9**, 2238-2252.

35. M. Z. Abid, K. Rafiq, A. Rauf, S. S. A. Shah, R. Jin and E. Hussain, *Nanoscale Advances*, 2023.

36. J. Liu, L. Wang, W. Song, M. Zhao, J. Liu, H. Wang, Z. Zhao, C. Xu and Z. Duan, *ACS Sustainable Chemistry & Engineering*, 2018, **7**, 2811-2820.

37. V. G. Komvokis, M. Marti, A. Delimitis, I. A. Vasalos and K. S. Triantafyllidis, *Applied Catalysis B: Environmental*, 2011, **103**, 62-71.

38. P. S. S. Reddya, N. S. Babua, N. Lingaiaha, P. S. Prasada and I. Raob, *Proc. Eur. Cong. Chem. Eng.*, 2007.

39. L.-L. Zhang, X.-M. Chen and C.-G. Liu, *Inorganic Chemistry*, 2019, **58**, 5221-5229.

40. S. N. Basahel, M. Mokhtar, T. T. Ali and K. Narasimharao, *Catalysis Today*, 2020, **348**, 166-176.

41. N. Zhang, C. He, Y. Jing, Y. Qian, T. Toyao and K.-i. Shimizu, *Surfaces and Interfaces*, 2024, **46**, 104120.

42. M. K. Singh and G. Rajaraman, *Inorganic chemistry*, 2019, **58**, 3175-3188.

43. M. G. Galloni, S. Campisi, A. Gervasini, S. Morandi and M. Manzoli, *Applied Catalysis A: General*, 2023, **655**, 119101.

44. W. Gao, D. Wen, J. Ho and Y. Qu, *Materials Today Chemistry*, 2019, **12**, 266-281.

45. X. Hu, L. Wu, S. Ju, C. Dong, Y. Yang and W. Qin, *Environmental Engineering Science*, 2014, **31**, 308-316.

46. X. Li, J. Chen, C. Lu, G. Luo and H. Yao, *Fuel*, 2021, **299**, 120910.

47. M. D. Esrafili, H. Janebi and P. Mousavian, *Applied Surface Science*, 2021, **569**, 151001.

48. H. Yu, X. Qi, X. Du, Y. Pan, X. Feng, W. Shan and Y. Xiong, *Molecular Catalysis*, 2023, **537**, 112960.

49. E. M. Goliaei and N. Seriani, *Applied Surface Science*, 2022, **579**, 152215.

50. K. Feng, R. Lin, T. Chen, Y. Hu, Y. Feng, D. Chen, M. H. Tahir and T. Cao, *Journal of Environmental Chemical Engineering*, 2024, 111891.

51. H. Liu, S. Yang, G. Wang, H. Liu, Y. Peng, C. Sun, J. Li and J. Chen, *Environmental Science & Technology*, 2022, **56**, 16325-16335.

52. H. Liu, J. Chen, Y. Wang, S. Xiong, Z. Su, Y. Wang, W. Yang, X. Chu, W. Yang and Y. Peng, *Chemical Engineering Journal*, 2021, **414**, 128643.

53. X. Hu, Y. Wang, R. Wu and Y. Zhao, *Molecular Catalysis*, 2021, **509**, 111656.

54. F. Zasada, J. Gryboś, E. Budiyanto, J. Janas and Z. Sojka, *Journal of Catalysis*, 2019, **371**, 224-235.

55. Q. Zhao, Z. Yan, C. Chen and J. Chen, *Chemical Reviews*, 2017, **117**, 10121-10211.

56. G. Chen, C. Guyon, Z. Zhang, B. Da Silva, P. Da Costa, S. Ognier, D. Bonn and M. Tatoulian, *Microfluidics and nanofluidics*, 2014, **16**, 141-148.

57. Q. Shen, L. Li, J. Li, H. Tian and Z. Hao, *Journal of hazardous materials*, 2009, **163**, 1332-1337.

58. M.-J. Kim, S.-J. Lee, I.-S. Ryu, M.-W. Jeon, S.-H. Moon, H.-S. Roh and S. G. Jeon, *Molecular Catalysis*, 2017, **442**, 202-207.

59. Y. Li, A. Sundermann, O. Gerlach, K.-B. Low, C. C. Zhang, X. Zheng, H. Zhu and S. Axnanda, *Catalysis Today*, 2019, DOI: https://doi.org/10.1016/j.cattod.2019.04.063.

60. J. Pérez-Ramírez, F. Kapteijn, G. Mul and J. A. Moulijn, *Journal of Catalysis*, 2002, **208**, 211-223.

61. S. Li, Y. Li, W. Shen, Y. Bai and L. Kong, *Journal of Cleaner Production*, 2022, **380**, 134961.

62. Y. Matsumura and J. B. Moffat, *Journal of Catalysis*, 1994, **148**, 323-333.

63. S. Sugiyama, K. Abe, H. Hayashi and J. B. Moffat, *Applied Catalysis A: General*, 1999, **183**, 135-142.

64. Y. Cui, H. Liu, Y. Lin and Z. Ma, *Journal of the Taiwan Institute of Chemical Engineers*, 2016, **67**, 254-262.

65. C. Huang, Z. Ma, P. Xie, Y. Yue, W. Hua and Z. Gao, *Journal of Molecular Catalysis A: Chemical*, 2015, **400**, 90-94.

66. M. G. Galloni, S. Campisi, A. Gervasini, S. Morandi and M. Manzoli, *Applied Catalysis A: General*, 2023, **655**, 119101.

67. X. Wei, Y. Wang, X. Li, R. Wu and Y. Zhao, *Molecular Catalysis*, 2020, **491**, 111005.

68. X. Tan, H. Chen, L. Shi, Q. Lu, S. Qi, C. Yi and B. Yang, *Catalysis Letters*, 2023, **153**, 3724-3733.

69. K.-M. Lee, G. Kwon, S. Hwang, J. A. Boscoboinik and T. Kim, *Catalysis Science & Technology*, 2021, **11**, 7850-7865.

70. D. Jia, K. Hanna, G. Mailhot and M. Brigante, *Molecules*, 2021, **26**, 5748.

71. U. Quyyum, K. Rafiq, M. Z. Abid, F. Ahmad, A. Rauf and E. Hussain, *Environmental Science: Water Research & Technology*, 2023, **9**, 1147-1160.

72. M. Jalil, K. Rafiq, M. Z. Abid, A. Rauf, S. Wang, S. Iqbal and E. Hussain, *Nanoscale Advances*, 2023, **5**, 3233-3246.

73. K. U. Sahar, K. Rafiq, M. Z. Abid, A. Rauf, U. u. Rehman, M. A. Nadeem, R. Jin and E. Hussain, *Colloids and Surfaces A: Physicochemical and Engineering Aspects*, 2023, **674**, 131942.

74. A. Aslam, M. Z. Abid, K. Rafiq, A. Rauf and E. Hussain, *Scientific Reports*, 2023, **13**, 6306.

75. H. Beyer, J. Emmerich, K. Chatziapostolou and K. Koehler, *Applied Catalysis A: General*, 2011, **391**, 411-416.

76. L. Han, M. Gao, J.-y. Hasegawa, S. Li, Y. Shen, H. Li, L. Shi and D. Zhang, *Environmental Science & Technology*, 2019, **53**, 6462-6473.

77. L. Rocha-Meneses, A. Inayat, M. Ayoub, S. Ullah, S. R. Naqvi, S. Farrukh, A. Mustafa, A. Z. Abdullah and A. H. Bhat, *Environmental Progress & Sustainable Energy*, 2023, **42**, e13982.

78. S. Wojcik, P. Indyka, Z. Sojka and A. Kotarba, *Catalysis Today*, 2020, **348**, 111-117.

79. G. Grzybek, P. Stelmachowski, S. Gudyka, J. Duch, K. Ćmil, A. Kotarba and Z. Sojka, *Applied Catalysis B: Environmental*, 2015, **168-169**, 509-514.

80. M. Inger, J. Rajewski, M. Ruszak and M. Wilk, *Chemical Papers*, 2019, **73**, 1979-1986.

81. B. M. Abu-Zied, S. A. Soliman and S. E. Abdellah, *Journal of Industrial and Engineering Chemistry*, 2015, **21**, 814-821.

82. S. Li, J. Zhao, Z. Song, H. Wang, T. Zhang, J. Liu and Q. Jiang, *Fuel*, 2024, **362**, 130745.

83. A. Inayat, L. Rocha-Meneses, M. Ayoub, S. Ullah, A. Z. Abdullah, S. R. Naqvi and A. H. Bhat, *Environmental Science and Pollution Research*, 2023, 1-12.

84. T. Franken and R. Palkovits, *Applied Catalysis B: Environmental*, 2015, **176-177**, 298-305.

85. A. Klyushina, K. Pacultová, K. Karásková, K. Jirátová, M. Ritz, D. Fridrichová, A. Volodarskaja and L. Obalová, *Journal of Molecular Catalysis A: Chemical*, 2016, **425**, 237-247.

86. H. Yu, X. Wang, X. Wu and Y. Chen, *Chemical Engineering Journal*, 2018, **334**, 800-806.

87. M. Tursun, X. Wang, F. Zhang and H. Yu, *Catalysis Communications*, 2015, **65**, 1-5.

88. S. Wójcik, G. Grzybek, P. Stelmachowski, Z. Sojka and A. Kotarba, *Catalysts*, 2020, **10**, 41.

89. M. Inger, B. Moszowski, M. Ruszak, J. Rajewski and M. Wilk, *Catalysts*, 2020, **10**, 987.

90. P. Hermawan, J. Kim, M. H. Jeong, S. A. Choi, S.-M. Hwang and S. K. Jeong, *Available at SSRN 4693392*.

91. A. Klegova, K. Pacultová, T. Kiška, P. Peikertová, A. Rokicińska, P. Kuśtrowski and L. Obalová, *Molecular Catalysis*, 2022, **533**, 112754.

92. B. Abu-Zied, S. Soliman and S. Abdellah, *Current Catalysis*, 2020, **9**, 152-162.

93. B. Li, X. Duan, T. Zhao, B. Niu, G. Li, Z. Zhao, Z. Yang, D. Liu, F. Zhang and J. Cheng, *Environmental Science & Technology*, 2024.

94. P. Lu, L. Ye, X. Yan, X. Chen, P. Fang, D. Chen, D. Chen and C. Cen, *Journal of Hazardous Materials*, 2021, **414**, 125468.

95. T. Gaidei, A. Kokorin, N. Pillet, V. Sadov, M. Strukova, S. Filatov, E. Khaustova and N. Yaroshenko, *Russian Journal of Applied Chemistry*, 2010, **83**, 1130-1138.

96. C. Ratanatawanate, A. Chyao and K. J. Balkus Jr, *Journal of the American Chemical Society*, 2011, **133**, 3492-3497.

97. S. Imamura, J.-i. Tadani, Y. Saito, Y. Okamoto, H. Jindai and C. Kaito, *Applied Catalysis A: General*, 2000, **201**, 121-127.

98. Y. Li, A. Sundermann, O. Gerlach, K.-B. Low, C. C. Zhang, X. Zheng, H. Zhu and S. Axnanda, *Catalysis Today*, 2020, **355**, 608-619.

99. J. Michael, 2017.

100. T. C. Peck, G. K. Reddy, M. Jones and C. A. Roberts, *The Journal of Physical Chemistry C*, 2017, **121**, 8435-8443.

101. Y. Lin, T. Meng and Z. Ma, *Journal of Industrial and Engineering Chemistry*, 2015, **28**, 138-146.

102. Y. Wang, X. Zhou, X. Wei, X. Li, R. Wu, X. Hu and Y. Zhao, *Molecular Catalysis*, 2021, **501**, 111370.

103. M. G. Galloni, 2022.

104. M. Galloni, S. Campisi and A. Gervasini, 2020.

105. X. Liu, Y. Wang, R. Wu and Y. Zhao, *Catalysis Surveys from Asia*, 2021, **25**, 168-179.

106. M. Konsolakis, *ACS Catalysis*, 2015, **5**, 6397-6421.

107. Y. Ni, Z. Han, Y. Chai, G. Wu and L. Li, 2023.

108. H. Xu, Y. Ma, J. Chen, W.-x. Zhang and J. Yang, *Chemical society reviews*, 2022, **51**, 2710-2758.

109. M. Zabilskiy, P. Djinović, E. Tchernychova and A. Pintar, *Applied Catalysis B: Environmental*, 2016, **197**, 146-158.

110. H. Zhu, Y. Li and X. Zheng, *Applied Catalysis A: General*, 2019, **571**, 89-95.

111. X. Fan, S. Kang, J. Li and T. Zhu, *RSC Advances*, 2018, **8**, 26998-27007.

112. H. Zeng and X. Pang, *Applied Catalysis B: Environmental*, 1997, **13**, 113-122.

113. M. Jabłońska, M. A. Arán, A. M. Beale, K. Góra-Marek, G. Delahay, C. Petitto, K. Pacultová and R. Palkovits, *RSC advances*, 2019, **9**, 3979-3986.

114. S. Carabineiro, E. Papista, G. Marnellos, P. Tavares, F. Maldonado-Hódar and M. Konsolakis, *Molecular Catalysis*, 2017, **436**, 78-89.

115. M. Lykaki, E. Papista, N. Kaklidis, S. A. Carabineiro and M. Konsolakis, *Catalysts*, 2019, **9**, 233.

116. K. Karásková, K. Pacultová, K. Jirátová, D. Fridrichová, M. Koštejn and L. Obalová, *Catalysts*, 2020, **10**, 1134.

117. X. Hu, Y. Wang, R. Wu, L. Zhao, X. Wei and Y. Zhao, *Applied Surface Science*, 2020, **514**, 145892.

118. T. Zhao, Y. Li, Q. Gao, Z. Liu and X. Xu, *Catalysis Communications*, 2020, **137**, 105948.

119. P. H. Ho, M. Jabłońska, M. Nocuń, G. Fornasari, F. Ospitali, A. Vaccari, P. Benito and R. Palkovits, *ChemCatChem*, 2019, **11**, 5580-5592.

120. E. M. Iwanek, L. F. Liotta, G. Pantaleo, K. Krawczyk, E. Gdyra, J. Petryk, J. W. Sobczak and Z. Kaszkur, *Catalysts*, 2021, **11**, 325.

121. B. M. Abu-Zied, L. Obalová, K. Pacultová, A. Klegova and A. M. Asiri, *Journal of Industrial and Engineering Chemistry*, 2021, **93**, 279-289.

122. E. M. Kostyukhin, A. L. Kustov, N. V. Evdokimenko, A. I. Bazlov and L. M. Kustov, *Journal of the American Ceramic Society*, 2021, **104**, 492-503.

123. D. Wang, Q. Yao, S. Hui and Y. Niu, *Fuel*, 2019, **251**, 23-29.

124. W. Muhammad, L. Wu, A. El Kasmi, A. Muhammad and Z. Tian, *Journal of Thermal Science*, 2023, **32**, 531-541.

125. Y. Zeng, Z. Wu, L. Guo, Y. Wang, S. Zhang and Q. Zhong, *Molecular Catalysis*, 2020, **488**, 110916.

126. Y. Zeng, F. Lyu, Y. Wang, S. Zhang, Q. Zhong and Z. Zhong, *Molecular Catalysis*, 2022, **525**, 112356.

127. L. Sheng, Z. Ma, S. Chen, J. Lou, C. Li, S. Li, Z. Zhang, Y. Wang and H. Yang, *Chinese Journal of Catalysis*, 2019, **40**, 1070-1077.

128. Z. Z. Khan, I. A. Khan, I. Khan, M. H. S. Wattoo and A. Badshah, *Solid State Sciences*, 2019, **98**, 106035.

129. D. Wang, Q. Yao, C. Mou, S. Hui and Y. Niu, *Fuel*, 2019, **254**, 115719.

130. F. Zhao, D. Wang, X. Li, Y. Yin, C. Wang, L. Qiu, J. Yu and H. Chang, *Industrial & Engineering Chemistry Research*, 2022, **61**, 13854-13862.

131. M.-x. Xu, H.-X. Wang, H.-d. Ouyang, L. Zhao and Q. Lu, *Journal of Hazardous Materials*, 2021, **401**, 123334.

132. M. Zabilskiy, I. Arčon, P. Djinović, E. Tchernychova and A. Pintar, *ChemCatChem*, 2021, **13**, 1814-1823.

133. A. A. Khan, A. Ahmad, H. M. Al-Swaidan, S. Haider, M. S. Akhtar and S. U. Khan, *Molecular Catalysis*, 2022, **527**, 112392.

134. C.-G. Liu, Y.-J. Chu, L.-L. Zhang, C. Sun and J.-Y. Shi, *Environmental Science & Technology*, 2019, **53**, 12893-12903.

135. M. Wang, W. Li and S. Wang, *The Journal of Physical Chemistry C*, 2023, **127**, 20344-20353.

136. S. Xie, D. Kim, K. Ye, L. Tetard and F. Liu, *Journal of Rare Earths*, 2023, **41**, 941-951.

137. M. Jabłońska and R. Palkovits, *Catalysis Science & Technology*, 2016, **6**, 49-72.

138. D. F. Swearer, H. Robatjazi, J. M. P. Martirez, M. Zhang, L. Zhou, E. A. Carter, P. Nordlander and N. J. Halas, *ACS nano*, 2019, **13**, 8076-8086.

139. D. Tichit and B. Coq, *CATTECH*, 2003, **7**, 206-217.

140. F. Gholami, M. Tomas, Z. Gholami and M. Vakili, *Science of the Total Environment*, 2020, **714**, 136712.

Please Materials Advances argins

ARTICLE

141. A. De Stefanis, M. Dondi, G. Perez and A. Tomlinson, *Chemosphere*, 2000, **41**, 1161-1165.

142. Y. Zhang, X. Wang, Y. Zhu, B. Hou, X. Yang, X. Liu, J. Wang, J. Li and T. Zhang, *The Journal of Physical Chemistry C*, 2014, **118**, 1999-2010.

143. E. E. Kiss, T. J. Vulić and A. F. . Reitzmann, *Reaction Kinetics and Catalysis Letters*, 2005, **86**, 233-240.

144. M. C. Karaeyvaz and S. Balci, *Microporous and Mesoporous Materials*, 2021, **323**, 111193.

145. X. Xing, N. Li, J. Cheng, Y. Sun, G. Wang, Z. Zhang, H. Xu, C. He and Z. Hao, *Industrial & Engineering Chemistry Research*, 2019, **58**, 9362-9371.

146. S. Kannan and C. Swamy, *Catalysis Today*, 1999, **53**, 725-737.

147. Z. Zhuang, B. Guan, J. Chen, C. Zheng, J. Zhou, T. Su, Y. Chen, C. Zhu, X. Hu and S. Zhao, *Chemical Engineering Journal*, 2024, 150374.

148. Z. Tišler, A. Klegová, E. Svobodová, J. Šafář, K. Strejcová, J. Kohout, S. Šlang, K. Pacultová, D. Rodríguez-Padrón and R. Bulánek, *Catalysts*, 2020, **10**, 1398.

149. G. He, B. Zhang, H. He, X. Chen and Y. Shan, *Science of the total environment*, 2019, **673**, 266-271.

150. L. J. Lobree, I.-C. Hwang, J. A. Reimer and A. T. Bell, *Journal of Catalysis*, 1999, **186**, 242-253.

151. A. Ates, A. Reitzmann, C. Hardacre and H. Yalcin, *Applied Catalysis A: General*, 2011, **407**, 67-75.

152. M. Jabłońska, M. A. Arán, A. M. Beale, G. Delahay, C. Petitto, M. Nocuń and R. Palkovits, *Applied Catalysis B: Environmental*, 2019, **243**, 66-75.

153. Y. Zhang, Y. Guo, N. Li and Y. Feng, *Polish Journal of Environmental Studies*, 2019, **28**.

154. P. H. Ho, M. Jabłońska, R. Palkovits, E. Rodríguez-Castellón, F. Ospitali, G. Fornasari, A. Vaccari and P. Benito, *Chemical Engineering Journal*, 2020, **379**, 122259.

155. S. Xiong, J. Chen, N. Huang, S. Yang, Y. Peng and J. Li, *Environmental Science & Technology*, 2019, **53**, 10379-10386.

156. M. Armandi, T. Andana, S. Bensaid, M. Piumetti, B. Bonelli and R. Pirone, *Catalysis Today*, 2020, **345**, 59-70.

157. A. Inayat, M. Ayoub, A. Z. Abdullah, S. Ullah and S. R. Naqvi, *Environmental Progress & Sustainable Energy*, 2019, **38**, 13129.

158. D. Lopes, F. Zotin and L. A. Palacio, *Applied Catalysis B: Environmental*, 2018, **237**, 327-338.

159. J. Akil, C. Ciotonea, S. Siffert, S. Royer, L. Pirault-Roy, R. Cousin and C. Poupin, *Catalysis Today*, 2022, **384**, 97-105.

160. C. d. O. P. Teixeira, S. da Silva Montani, J. C. S. Soares, L. A. Palacio and F. M. Z. Zotin, *Molecular Catalysis*, 2024, **561**, 114157.

161. M. Rutkowska, A. Jankowska, E. Różycka-Dudek, W. Dubiel, A. Kowalczyk, Z. Piwowarska, S. Llopis, U. Díaz and L. Chmielarz, *Catalysts*, 2020, **10**, 1139.

162. J. Zhang, X. Tang, H. Yi, Q. Yu, Y. Zhang, J. Wei and Y. Yuan, *Applied Catalysis A: General*, 2022, **630**, 118467.

163. Y. Li and J. N. Armor, *Applied Catalysis B: Environmental*, 1992, **1**, L21-L29.

164. S. A. Yashnik, O. P. Taran, T. A. Surovtsova, A. B. Ayusheev and V. N. Parmon, *Journal of Environmental Chemical Engineering*, 2022, **10**, 107950.

165. N. F. Biturini, A. P. N. Santos and M. S. Batista, *Reaction Kinetics, Mechanisms and Catalysis*, 2019, **126**, 341-352.

166. P. J. Smeets, J. S. Woertink, B. F. Sels, E. I. Solomon and R. A. Schoonheydt, *Inorganic chemistry*, 2010, **49**, 3573-3583.

167. U. Deka, I. Lezcano-Gonzalez, B. M. Weckhuysen and A. M. Beale, *ACS Catalysis*, 2013, **3**, 413-427.

168. T. Žumbar, I. Arčon, P. Djinović, G. Aquilanti, G. Žerjav, A. Pintar, A. Ristić, G. Dražić, J. Volavšek and G. Mali, *ACS applied materials & interfaces*, 2023, **15**, 28747-28762.

169. B. Liu, D. Yao, F. Wu, L. Wei, X. Li and X. Wang, *Industrial & Engineering Chemistry Research*, 2019, **58**, 20516-20527.

170. S. Yasumura, H. Ide, T. Ueda, Y. Jing, C. Liu, K. Kon, T. Toyao, Z. Maeno and K.-i. Shimizu, *JACS Au*, 2021, **1**, 201-211.

171. M. Jin, P. Wang, L. Zhang, C. Ao and L. Lei, *Thermal Science and Engineering Progress*, 2023, **45**, 102088.

172. M. Jabłońska, M. E. Potter and A. M. Beale, *ChemCatChem*, 2024, **16**, e202301214.

173. C. Ruan, X. Wang, C. Wang, L. Zheng, L. Li, J. Lin, X. Liu, F. Li and X. Wang, *Nature Communications*, 2022, **13**, 718.

174. X. Zhang, Q. Shen, C. He, C. Ma, J. Cheng, L. Li and Z. Hao, *Acs Catalysis*, 2012, **2**, 512-520.

175. W.-S. Ju, M. Matsuoka and M. Anpo, *Catalysis letters*, 2001, **71**, 91-93.

176. S. Dzwigaj, D. Reja, S. Koné-Guira, A. Miche, G. Costentin and C. Thomas, *Applied Catalysis A: General*, 2023, **657**, 119119.

177. M. Shukla, B. V. Chauhan, S. Verma and A. Dhar, *Solids*, 2022, **3**, 665-683.

178. B. Bromley, C. Pischetola, L. Nikoshvili, F. Cárdenas-Lizana and L. Kiwi-Minsker, *Molecules*, 2020, **25**, 3867.

179. B. Kang, M. Li, Z. Di, X. Guo, Y. Wei, J. Jia and R. Zhang, *Catalysis Today*, 2022, **402**, 17-26.

180. B. Kang, R. Zhang, M. Guo, X. Guo, Z. Di, Y. Wei and J. Jia, *Energy & Fuels*, 2023.

181. D. Pietrogiacomi, M. C. Campa, L. Ardemani and M. Occhiuzzi, *Catalysis Today*, 2019, **336**, 131-138.

182. G. A. Zenkovets, R. A. Shutilov, V. I. Sobolev and V. Y. Gavrilov, *Catalysis Communications*, 2020, **144**, 106072.

183. C. Gao, J. Li, J. Zhang and X. Sun, *Catalysts*, 2020, **10**, 646.

184. J. B. Lim, S. H. Cha and S. B. Hong, *Applied Catalysis B: Environmental*, 2019, **243**, 750-759.

185. K. M. Farhan, A. N. Thabassum, T. M. Ismail and P. Sajith, *Catalysis Science & Technology*, 2022, **12**, 1466-1475.

186. B. Zhang, G. He, Y. Shan and H. He, *Catalysis Today*, 2019, **327**, 177-181.

187. Y. You, S. Chen, J. Li, J. Zeng, H. Chang, L. Ma and J. Li, *Journal of hazardous materials*, 2020, **383**, 121117.

188. L. M. Kustov, S. F. Dunaev and A. L. Kustov, *Molecules*, 2022, **27**, 398.

189. S. Li, J. Wang, R. Shang, J. Zhao, Q. Xu, H. Wang and J. Liu, *Molecular Catalysis*, 2024, **552**, 113706.

190. X. Liang, H. Tang, F. Yang, G. Tu, F. Zhang, Q. Xiao, Y. Zhong and W. Zhu, *Microporous and Mesoporous Materials*, 2019, **290**, 109655.

191. G. Zhao, E. Benhelal, A. Adesina, E. Kennedy and M. Stockenhuber, *The Journal of Physical Chemistry C*, 2019, **123**, 27436-27447.

192. J. Zeng, S. Chen, Z. Fan, C. Wang, H. Chang and J. Li, *Industrial & Engineering Chemistry Research*, 2020, **59**, 19500-19509.

193. J. Cheng, D. Zheng, G. Yu, R. Xu, C. Dai, N. Liu, N. Wang and B. Chen, *ACS Catalysis*, 2022, **13**, 934-947.

194. T. Zhang, Y. Qiu, G. Liu, J. Chen, Y. Peng, B. Liu and J. Li, *Journal of Catalysis*, 2020, **392**, 322-335.

195. J. Han, A. Wang, G. Isapour, H. Harelind, M. Skoglundh, D. Creaser and L. Olsson, *Industrial & Engineering Chemistry Research*, 2021, **60**, 17826-17839.

196. S. Li, C. Zhang, J. Li, Y. Li, H. Wang, C. Li and Y. Song, *Research on Chemical Intermediates*, 2019, **45**, 3601-3616.

197. G. Sádovská, M. Bernauer, B. Bernauer, E. Tabor, A. Vondrová and Z. Sobalík, *Catalysis Communications*, 2018, **112**, 58-62.

198. M. L. Bols, B. E. Snyder, H. M. Rhoda, P. Cnudde, G. Fayad, R. A. Schoonheydt, V. Van Speybroeck, E. I. Solomon and B. F. Sels, *Nature Catalysis*, 2021, **4**, 332-340.

199. T. Wu, Y. Shen, L. Feng, Z. Tang and D. Zhang, *Journal of Chemical & Engineering Data*, 2019, **64**, 3473-3482.

200. A. J. Shih, J. M. González, I. Khurana, L. P. Ramírez, A. Peña L, A. Kumar and A. L. Villa, *ACS Catalysis*, 2021, **11**, 10362-10376.

201. S. J. Lee, I. S. Ryu, S. G. Jeon and S. H. Moon, *Environmental Progress & Sustainable Energy*, 2019, **38**, 451-456.

202. M. C. Campa, D. Pietrogiacomi, C. Catracchia, S. Morpurgo, J. Olszowka, K. Mlekodaj, M. Lemishka, J. Dedecek, A. Kornas and E. Tabor, *Applied Catalysis B: Environmental*, 2024, **342**, 123360.

203. E. Tabor, K. Mlekodaj, G. Sádovská, M. Bernauer, P. Klein, P. Sazama, J. Dědeček and Z. Sobalík, *Microporous and Mesoporous Materials*, 2019, **281**, 15-22.

204. E. Tabor, G. Sádovská, M. Bernauer, P. Sazama, J. Nováková, V. Fila, T. Kmječ, J. Kohout, K. Závěta and Z. Sobalík, *Applied Catalysis B: Environmental*, 2019, **240**, 358-366.

205. N. Pal and A. Bhaumik, *RSC advances*, 2015, **5**, 24363-24391.

206. P. Verma, Y. Kuwahara, K. Mori, R. Raja and H. Yamashita, *Nanoscale*, 2020, **12**, 11333-11363.

207. Y. Qin, Z. Qu, C. Dong, Y. Wang and N. Huang, *Journal of Environmental Sciences*, 2019, **76**, 208-216.

208. M. Marafi and E. Furimsky, *Energy & Fuels*, 2017, **31**, 5711-5750.

209. X. Wei, X.-F. Yang, A.-Q. Wang, L. Li, X.-Y. Liu, T. Zhang, C.-Y. Mou and J. Li, *The Journal of Physical Chemistry C*, 2012, **116**, 6222-6232.

210. Z. Li, B. Li, C. Yu, H. Wang and Q. Li, *Advanced Science*, 2023, **10**, 2206605.

211. L. Yu, H. Hu, H. B. Wu and X. W. Lou, *Advanced Materials*, 2017, **29**, 1604563.

212. K. Pacultová, A. Klegova, T. Kiška, D. Fridrichová, A. Martaus, A. Rokicińska, P. Kuśtrowski and L. Obalová, *Materials Research Bulletin*, 2020, **129**, 110892.

213. M. C. Campa, A. M. Doyle, G. Fierro and D. Pietrogiacomi, *Catalysis Today*, 2022, **384**, 76-87.

214. B. Bozorgi, J. Karimi-Sabet and P. Khadiv-Parsi, *Environmental Technology & Innovation*, 2022, **26**, 102344.

215. T. Umegaki, H. Katori, K. Otake, R. Yamamoto and Y. Kojima, *Journal of Sol-Gel Science and Technology*, 2019, **92**, 715-722.

216. S. Wang, B. Yan, J. Chai, T. Li, H. Yu, T. Li, P. Cao, F. Yang, X. Yuan and H. Yin, *European Journal of Inorganic Chemistry*, 2021, **2021**, 2201-2210.

217. O. Muccioli, E. Meloni, S. Renda, M. Martino, F. Brandani, P. Pullumbi and V. Palma, *Processes*, 2023, **11**, 1511.

218. T. Boningari, D. K. Pappas and P. G. Smirniotis, *Journal of Catalysis*, 2018, **365**, 320-333.

219. D. K. Pappas, T. Boningari, P. Boolchand and P. G. Smirniotis, *Journal of Catalysis*, 2016, **334**, 1-13.

220. P. Nematollahi and M. D. Esrafili, *RSC advances*, 2016, **6**, 59091-59099.

221. J.-H. Lee, Y.-J. An, H. Choi, J. Lee, S.-Y. Lee and S.-J. Park, *Applied Catalysis O: Open*, 2024, 206937.

222. M. D. Esrafili and N. Saeidi, *Applied Surface Science*, 2017, **403**, 43-50.

223. M. D. Esrafili and N. Saeidi, *Applied Surface Science*, 2018, **444**, 584-589.

224. M. D. Esrafili, *Physics Letters A*, 2017, **381**, 2085-2091.

225. B. Gao, J.-x. Zhao, Q.-h. Cai, X.-g. Wang and X.-z. Wang, *The Journal of Physical Chemistry A*, 2011, **115**, 9969-9976.

226. T. Boningari, D. K. Pappas and P. G. Smirniotis, *Journal of Catalysis*, 2018, **365**, 320-333.

227. M. D. Esrafili and N. Saeidi, *Applied Surface Science*, 2017, **403**, 43-50.

228. M. D. Esrafili and S. Heydari, *Molecular Physics*, 2020, DOI: 10.1080/00268976.2020.1759830, 1-8.

229. M. D. Esrafili, *Physics Letters A*, 2017, **381**, 2085-2091.

230. M. D. Esrafili and S. Heidari, *Chemical Physics Letters*, 2019, **725**, 52-58.

231. J. Sun, L. Wang, L. Zhang, Y. Zhao, Y. Chi, H. Wang, C. Li, J. Liu and J. Liu, *ACS Applied Energy Materials*, 2021, **4**, 8496-8505.

232. X. Liu and L. Sheng, *Materials Today Communications*, 2021, **28**, 102585.

233. G. Fan, Q. Wang, H. Xu, X. Wang, X. Tu and X. Chu, *Applied Surface Science*, 2021, **544**, 148776.

234. Y. Xiong, Y. Zhao, W. Shan, X. Feng, J. Cui, Z. Lou, G. Shao, M. Dong and H. Yu, *Chemosphere*, 2022, **303**, 135257.

235. Y. Xiong, Y. Zhao, X. Qi, J. Qi, Y. Cui, H. Yu and Y. Cao, *Environmental Science & Technology*, 2021, **55**, 13335-13344.

236. E. Meloni, M. Martino, S. Renda, O. Muccioli, P. Pullumbi, F. Brandani and V. Palma, *Catalysts*, 2022, **12**, 1405.

237. X. Guan, H. Asakura, R. Han, S. Xu, H.-X. Liu, L. Chen, Z. Yao, J. H. C. Yan, T. Tanaka and Y. Guo, *ACS catalysis*, 2023, **13**, 13816-13827.

238. A. Hassanpour, M. Kamel, S. Ebrahimiasl, A. G. Ebadi, S. Arshadi and Z. Ghulinezhad Ahangari, *Journal of Molecular Modeling*, 2022, **28**, 1-14.

239. X. Hu, E. Zhang, W. Li, L. Wu, Y. Zhou, H. Zhang and C. Dong, *Applied Sciences*, 2022, **12**, 5034.

240. X. Tan, S. Qi, G. Cheng, C. Yi and B. Yang, *Available at SSRN 4470798*.

241. M. Derdare, A.-G. Boudjahem and M. Boulbazine, *Structural Chemistry*, 2022, **33**, 2043-2062.

242. M. D. Esrafili, S. Asadollahi and S. Heydari, *Journal of Molecular Graphics and Modelling*, 2019, **89**, 41-49.

243. A. A. Khan, M. D. Esrafili, F. Ali, R. Ahmad and I. Ahmad, *Journal of Molecular Graphics and Modelling*, 2022, **114**, 108186.

244. P. Li, T. Zhang, H. Sun, Y. Gao, Y. Zhang, Y. Liu, C. Ge, H. Chen, X. Dai and X. Zhang, *Nano Research*, 2022, **15**, 3001-3009.

245. J. Qi, X. Qi, Y. Pan, J. Cui, Y. Xiong, W. Shan and H. Yu, *Applied Surface Science*, 2023, **611**, 155657.

Journal Name

ARTICLE

246. Y. Bai, Y. Hou, Y. Guo, N. Xiang, X. Han, H. Wang, Z. Wu and Z. Huang, *Journal of Colloid and Interface Science*, 2022, **616**, 55-66.

247. Z. Liu, H. Wang, Y. Gao and J. Zhao, *Molecules*, 2023, **28**, 4485.

248. M. D. Esrafili and B. Nejadebrahimi, *Chemical Physics Letters*, 2019, **716**, 11-16.

249. X. Dai, Y. Cheng, T. Liu and L. Mao, *Energy & Fuels*, 2024.

250. S. K. Tiwari, S. Sahoo, N. Wang and A. Huczko, *Journal of Science: Advanced Materials and Devices*, 2020, **5**, 10-29.

251. T. Das, B. K. Sharma, A. K. Katiyar and J.-H. Ahn, *Journal of Semiconductors*, 2018, **39**, 011007.

252. A. Akça, O. Karaman and C. Karaman, *ECS Journal of Solid State Science and Technology*, 2021, **10**, 041003.

253. X. Liu and L. Sheng, *Advanced Theory and Simulations*, 2023, **6**, 2200680.

254. R. Gholizadeh, Y.-X. Yu and Y. Wang, *Applied Surface Science*, 2017, **420**, 944-953.

255. M. D. Esrafili, *Chemical Physics Letters*, 2018, **708**, 94-99.

256. M. D. Esrafili, *Chemical Physics Letters*, 2018, **705**, 44-49.

257. M. Vakili, R. Gholizadeh, A. Ghadi, E. Salmasi and M. Sinnokrot, *Journal of Molecular Graphics and Modelling*, 2020, **101**, 107752.

258. Z. Liu, X.-r. Cheng, Y.-m. Yang, H.-z. Jia, B.-q. Bai and L. Zhao, *Materials*, 2019, **12**, 2611.

259. I. Majeed, U. Manzoor, F. K. Kanodarwala, M. A. Nadeem, E. Hussain, H. Ali, A. Badshah, J. A. Stride and M. A. Nadeem, *Catalysis Science & Technology*, 2018, **8**, 1183-1193.

260. L. Hu, J. Yan, C. Wang, B. Chai and J. Li, *Chinese Journal of Catalysis*, 2019, **40**, 458-469.

261. K. U. Sahar, K. Rafiq, M. Z. Abid, U. ur Rehman, A. Rauf and E. Hussain, *Reaction Chemistry & Engineering*, 2023, **8**, 2522-2536.

262. I. Troppová, M. Šihor, M. Reli, M. Ritz, P. Praus and K. Kočí, *Applied Surface Science*, 2018, **430**, 335-347.

263. D. Ma, X. Cao and Z. Cao, *The Journal of Physical Chemistry C*, 2023, **127**, 5800-5809.

264. D. Masih, Y. Ma and S. Rohani, *Applied Catalysis B: Environmental*, 2017, **206**, 556-588.

265. J. Li, M. Zhang, Q. Li and J. Yang, *Applied Surface Science*, 2017, **391**, 184-193.

266. J. O. Ighalo, M. L. Smith, A. Al Mayyahi and P. B. Amama, *Applied Catalysis B: Environment and Energy*, 2024, 124352.

267. S. Zhao, D. Chen, N. Li, Q. Xu, H. Li and J. Lu, *Journal of Alloys and Compounds*, 2023, **960**, 170830.

268. H. D. Mai, K. Rafiq and H. Yoo, *Chemistry–A European Journal*, 2017, **23**, 5631-5651.

269. P. Liu, X. Gu, K. Kang, H. Zhang, J. Cheng and H. Su, *ACS Applied Materials & Interfaces*, 2017, **9**, 10759-10767.

270. S. M. Rogge, A. Bavykina, J. Hajek, H. Garcia, A. I. Olivos-Suarez, A. Sepúlveda-Escribano, A. Vimont, G. Clet, P. Bazin and F. Kapteijn, *Chemical Society Reviews*, 2017, **46**, 3134-3184.

271. A. Bavykina, N. Kolobov, I. S. Khan, J. A. Bau, A. Ramirez and J. Gascon, *Chemical reviews*, 2020, **120**, 8468-8535.

272. K. Rafiq, H. D. Mai, J. K. Kim, J. M. Woo, B. M. Moon, C. H. Park and H. Yoo, *Sensors and Actuators B: Chemical*, 2017, **251**, 472-480.

273. F. Ahmad, K. Rafiq, T. Najam, E. Hussain, M. Sohail, M. Z. Abid, A. Mahmood, M. S. Javed and S. S. A. Shah, *International Journal of Hydrogen Energy*, 2023.

274. M. D. Esrafili, *Chemical Physics Letters*, 2018, **708**, 94-99.

275. M. D. Esrafili and E. Vessally, *Surface Science*, 2018, **667**, 105-111.

276. R. Gholizadeh, Y.-X. Yu and Y. Wang, *Applied Surface Science*, 2017, **420**, 944-953.

277. M. D. Esrafili, F. Mohammadian-Sabet and P. Nematollahi, *RSC advances*, 2016, **6**, 64832-64840.

278. P. Praus, L. Svoboda, M. Ritz, I. Troppová, M. Šihor and K. Kočí, *Materials Chemistry and Physics*, 2017, **193**, 438-446.

279. K. Kočí, M. Reli, I. Troppová, M. Šihor, J. Kupková, P. Kustrowski and P. Praus, *Applied Surface Science*, 2017, **396**, 1685-1695.

280. M. Reli, L. Svoboda, M. Šihor, I. Troppová, J. Pavlovský, P. Praus and K. Kočí, *Environmental Science and Pollution Research*, 2018, **25**, 34839-34850.

281. K. Kočí, M. Reli, I. Troppová, M. Šihor, T. Bajcarová, M. Ritz, J. Pavlovský and P. Praus, *Catalysts*, 2019, **9**, 735.

282. M. Reli, I. Troppová, M. Šihor, J. Pavlovský, P. Praus and K. Kočí, *Applied Surface Science*, 2019, **469**, 181-191.

283. P. Praus, J. Lang, A. Martaus, L. Svoboda, V. Matějka, M. Kormunda, M. Šihor, M. Reli and K. Kočí, *Journal of Inorganic and Organometallic Polymers and Materials*, 2019, **29**, 1219-1234.

284. V. Matějka, M. Šihor, M. Reli, A. Martaus, K. Kočí, M. Kormunda and P. Praus, *Materials Science in Semiconductor Processing*, 2019, **100**, 113-122.

285. P. Maitarad, A. Junkaew, V. Promarak, L. Shi and S. Namuangruk, *Applied Surface Science*, 2020, **508**, 145255.

286. S. Su, J. Ma, Z. Liu, D. Holiharimanana and H. Sun, *Catalysts*, 2023, **13**, 578.

287. M. D. Esrafili and S. Heydari, *Molecular Physics*, 2020, **118**, e1759830.

288. X. Hu, Y. Wang, R. Wu and Y. Zhao, *Applied Surface Science*, 2021, **538**, 148157.

289. S. Ketrat, T. Maihom, S. Wannakao, S. Probst, S. Nokbin and J. Limtrakul, *Inorganic chemistry*, 2017, **56**, 14005-14012.

290. P. Zhao, F. Qin, Z. Huang, C. Sun, W. Shen and H. Xu, *Chemical Engineering Journal*, 2018, **349**, 72-81.

291. V. Paluka, T. Maihom, M. Probst and J. Limtrakul, *Physical Chemistry Chemical Physics*, 2020, **22**, 13622-13628.

292. S. Chen, Y. Zhou, J. Li, Z. Hu, F. Dong, Y. Hu, H. Wang, L. Wang, K. K. Ostrikov and Z. Wu, *ACS Catalysis*, 2020, **10**, 10185-10196.

293. H. Louis, T. C. Egemonye, T. O. Unimuke, B. E. Inah, H. O. Edet, E. A. Eno, S. A. Adalikwu and A. S. Adeyinka, *ACS omega*, 2022, **7**, 34929-34943.

294. K. D. Vogiatzis, E. Haldoupis, D. J. Xiao, J. R. Long, J. I. Siepmann and L. Gagliardi, *The Journal of Physical Chemistry C*, 2016, **120**, 18707-18712.

295. B. Huang, Y. F. Wu, Z. Zhang, R. Chen, G. Y. Ren, N. Zhou, N. Li and Y. Qian, *Journal of Materials Chemistry A*, 2025.

296. Y.-X. Yu, *Journal of Colloid and Interface Science*, 2025, 137799.

297. B. Huang, G. y. Ren, R. Chen and N. Li, *Chemical Physics Letters*, 2025, **874-875**, 142178.

298. X. Hu, Y. Wang, Z. Ling, H. Song, Y. Cai, Z. Li, D. Zu and C. Li, *Applied Surface Science*, 2021, **556**, 149817.

299.   A. Al Mayyahi, S. Sarker, B. M.Everhart, B. Tonyali, U. Yucel and P. B Amama, *Journal of Physics and Chemistry of Solids*, 2022, **170**, 110875.

300.   A. Hermawan, T. Hasegawa, Y. Asakura and S. Yin, *Separation and Purification Technology*, 2021, **270**, 118815.

301.   A. A. Mayyahi, S. Sarker, B. M. Everhart, X. He and P. B. Amama, *Materials Today Communications*, 2022, **32**, 103835.

302.   L. Kong, M. Wang and C.-M. L. Wu, *ACS Materials Letters*, 2024, **6**, 1711-1721.

303.   N. J. Halas, P. Nordlander, H. Robatjazi, D. F. Swearer, C. Zhang, H. Zhao and L. Zhou, *Journal*, 2020.

304.   D. F. Swearer, H. Zhao, L. Zhou, C. Zhang, H. Robatjazi, J. M. P. Martirez, C. M. Krauter, S. Yazdi, M. J. McClain and E. Ringe, *Proceedings of the National Academy of Sciences*, 2016, **113**, 8916-8920.

305.   K. Rafiq, I. Sadia, M. Z. Abid, M. Z. Waleed, A. Rauf and E. Hussain, *ACS Biomaterials Science & Engineering*, 2024, **10**, 7268-7313.

306.   S. Ketrat, T. Maihom, S. Wannakao, M. Probst, S. Nokbin and J. Limtrakul, *Inorganic Chemistry*, 2017, **56**, 14005-14012.

307.   V. Paluka, T. Maihom, M. Probst and J. Limtrakul, *Physical Chemistry Chemical Physics*, 2020.

308.   S. Chen, Y. Zhou, J. Li, Z. Hu, F. Dong, Y. Hu, H. Wang, L. Wang, K. Ostrikov and Z. Wu, *ACS Catalysis*, 2020.

309.   D. Denysenko, J. Jelic, O. V. Magdysyuk, K. Reuter and D. Volkmer, *Microporous and Mesoporous Materials*, 2015, **216**, 146-150.

310.   A. Dey, T. Albert, R. Y. Kong, S. N. MacMillan, P. Moënne-Loccoz, K. M. Lancaster and D. P. Goldberg, *Inorganic Chemistry*, 2022, **61**, 14909-14917.

311.   H. Tang, Y. He, P. Liu, J. Shao, F. Lin and Z. Wang, *Energy & Fuels*, 2021, **35**, 18664-18679.

312.   Z. Yao, D. Qu, Y. Guo, Y. Yang and H. Huang, *Advances in Materials Science and Engineering*, 2019, **2019**, 1-9.

313.   R. Nava, B. Pawelec, P. Castaño, M. C. Álvarez-Galván, C. V. Loricera and J. L. G. Fierro, *Applied Catalysis B: Environmental*, 2009, **92**, 154-167.

314.   G. J. Kubas, *Chemical reviews*, 2007, **107**, 4152-4205.

315.   B. Kim, Z. Li, B. D. Kay, Z. Dohnálek and Y. K. Kim, *The Journal of Physical Chemistry C*, 2014, **118**, 9544-9550.

316.   S. Royer, D. Duprez, F. Can, X. Courtois, C. Batiot-Dupeyrat, S. Laassiri and H. Alamdari, *Chemical Reviews*, 2014, **114**, 10292-10368.

317.   I. Fechete, Y. Wang and J. C. Védrine, *Catalysis Today*, 2012, **189**, 2-27.

318.   T. Selvaraj, P. Aghalayam and J. J. Varghese, *Industrial & Engineering Chemistry Research*, 2024, **63**, 6591-6599.

319.   E. Winter, *Journal of Catalysis*, 1969, **15**, 144-152.

320.   E. V. Kondratenko and J. Pérez-Ramírez, *The Journal of Physical Chemistry B*, 2006, **110**, 22586-22595.

321.   S. Subramanian and C. Swamy, *Catalysis letters*, 1995, **35**, 361-372.

Materials Advances Accepted Manuscript

Data Availability Statement

The data and necessary protocols of this study have been included as part of the Supplementary

Information.

Materials Advances Accepted Manuscript